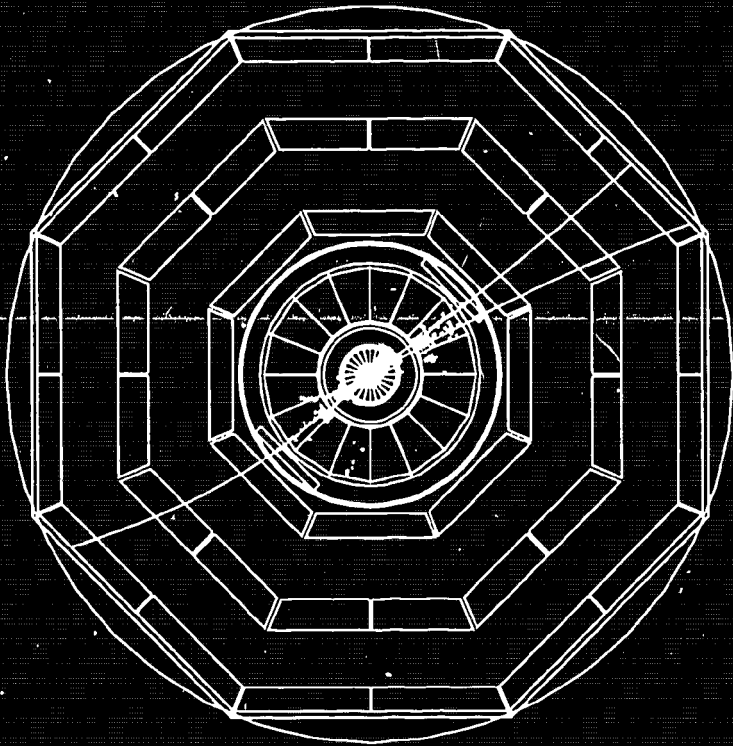


NL96F6-184
INIS-mf--15149

J/ψ Production and Decay at the Z Resonance



Pratibha Vikas

NL 96F6184



KS001969705
I: FI
DE008355001

J/ψ Production and Decay at the Z Resonance

J/ψ productie en verval op de Z resonantie (met een samenvatting in het Nederlands)

Proefschrift

Proefschrift ter verkrijging van de graad van doctor
aan de Universiteit Utrecht op gezag van de
Rector Magnificus, Prof. Dr. J. A. van Ginkel
ingevolge het besluit van het College van Decanen
in het openbaar te verdedigen
op 13 October 1994,
des middags te 12:45 uur

door

Pratibha Vikas

geboren op 30 april 1965, te Allahabad, India.

Promotor:

Prof. Dr. Ir. F. C. Ern 

Co-promotor:

Dr. R. Clare

To my parents

Contents

Motivation	1
1 Theory	3
1.1 Introduction	3
1.2 An Overview of the Standard Model	3
1.3 Heavy Flavor Decay	6
1.4 B Lifetime and the Determination of $ V_{cb} $	8
1.5 Heavy Flavor Fragmentation	8
1.6 $c\bar{c}$ Spectroscopy	10
1.6.1 The ψ' and J/ψ Mesons	11
1.7 ψ' Production at the Z Pole	12
1.8 J/ψ Production Mechanisms at the Z Pole	13
1.8.1 Decays of higher charmonium states	14
1.8.2 $Z \rightarrow b\bar{b}; b(\bar{b}) \rightarrow J/\psi + X$	14
1.8.3 $Z \rightarrow q\bar{q}g^*; g^* \rightarrow J/\psi + X$	15
1.8.4 $Z \rightarrow c\bar{c}J/\psi$	16
1.8.5 $Z \rightarrow J/\psi g(g)$	17
1.8.6 $Z \rightarrow J/\psi \gamma$	17
2 The L3 Experiment	21
2.1 Introduction	21
2.2 LEP	21
2.3 The L3 Detector	22
2.4 The Central Track Detector	24
2.5 The Luminosity Monitor	24
2.6 The Electromagnetic Calorimeter	26
2.7 The Scintillation Counters	27
2.8 The Hadron Calorimeter and Muon Filter	27
2.9 The Muon Detector	29
2.9.1 The precision chambers	30
2.9.2 The Z-chambers	30
2.10 The L3 Trigger	30
2.10.1 Level-1 trigger	31

2.10.2	Level-2 trigger	32
2.10.3	Level-3 trigger	32
2.11	Event Reconstruction	32
2.12	Event Simulation	33
3	Event Selection and Acceptance Calculations	35
3.1	Introduction	35
3.2	Hadron selection	35
3.2.1	Triggers	35
3.2.2	Event Selection and Acceptance	36
3.3	Event Preselection	39
3.4	Muon selection	39
3.5	J/ψ Selection	41
3.6	Background Simulation and Acceptance Calculation	41
3.6.1	Detector Inefficiency	47
4	J/ψ and ψ' Production	53
4.1	Introduction	53
4.2	Determination of J/ψ and ψ' Production	53
4.3	Determination of $Br(Z^0 \rightarrow J/\psi + X)$	55
4.3.1	Systematic Error	55
4.3.2	Final Result	56
4.4	Determination of $Br(Z^0 \rightarrow \psi' + X)$	56
4.5	Non-b J/ψ Production	57
4.6	Determination of $Br(b \rightarrow J/\psi + X)$	60
4.7	Discussion and comparison with other experiments	61
5	B Physics with J/ψ tagged b hadrons	63
5.1	Introduction	63
5.2	Estimation of the b Hadron Four-Vector	63
5.2.1	b hadron momentum estimation	63
5.2.2	b hadron direction estimation	64
5.3	Measurement of the b quark fragmentation parameter, ϵ_b	64
5.3.1	Systematic errors	65
5.3.2	Final result	66
5.4	J/ψ Decay Angular Distribution	67
6	Measurement of the Average b Hadron Lifetime	73
6.1	Introduction	73
6.2	Vertex Finding and Decay Distance Determination	75
6.3	Event Selection	78
6.4	Determination of the proper time	78
6.5	The fitting procedure	79
6.5.1	Determination of the scale factor for τ_{bc}	80

6.5.2	Determination of τ_{bkd}	80
6.5.3	The Result	81
6.5.4	Systematic Errors	81
6.5.5	Final Result	84
6.5.6	Comparison with other Experiments	84
6.6	Determination of $ V_{cb} $	84
A	Full Vertex Reconstruction in L3	89
A.1	Introduction	89
A.2	Computation of the Vertex	89
B	Full Vertex Correction for 1992b	93
C	Determination of LEP Beam Spot Size	95
	Summary	103
	Sammenvatting	105
	Acknowledgements	107
	Curriculum Vitae	109

Motivation

The basic aim of high energy physics is to ascertain what the building blocks of matter are and to understand the interactions between them. The knowledge in this field has come a long way since the ancient times when nature was believed to be composed of air, water, earth and fire. Today's understanding of the fundamental constituents of matter is based on the existence of two kinds of point-like particles - the fermions and bosons. All matter is composed of fermions of which there are two distinct classes, the quarks and leptons, and the interactions between them are mediated by bosons. This knowledge is embodied in a conceptual framework, the Standard Model (SM) which is a culmination of several decades work by theoretical and experimental physicists.

The discovery of the predicted intermediate vector bosons, W^\pm and the Z at CERN in 1983, was a breakthrough for the SM. The Large Electron Positron (LEP) collider and SLC were commissioned at CERN and SLAC, respectively, to further study the properties of the weak neutral and charged currents mediated by these bosons. LEP, which has been operational since 1989, collides electrons and positrons at the center-of-mass energies in the vicinity of the Z resonance. Given its high luminosity and the experimentally 'clean' environment, a characteristic of e^+e^- colliders, it is an ideal environment to determine the SM parameters more accurately and also to look for physics beyond the SM.

A substantial fraction of all Z decay modes consist of decays into the heavy charm and bottom quarks ($\sim 12\%$ for c and $\sim 15\%$ for b). Thus, the LEP collider allows precision measurements in the heavy quark sector. Ever since the existence of the heavy quarks was established, there has been a considerable interest in the study of heavy quarkonia ($c\bar{c}$ and $b\bar{b}$ mesons) because the leptonic decay channels of these resonances provide the cleanest signals of heavy quarks. At LEP, the primary source of J/ψ mesons is the decay of b hadrons. Hence, the J/ψ meson provides a clean tag for b hadrons. In addition, a small fraction of J/ψ mesons is also expected to be produced via charm fragmentation and gluon bremsstrahlung. Distinguishing quark jets from gluon jets, and then studying gluon properties is a challenging problem for experimentalists. The gluon produced J/ψ is potentially a good candidate to tag gluon jets. In this thesis, J/ψ is identified by its decay into a muon pair. J/ψ production from the sources accessible at the current LEP luminosity has been investigated. Further, some properties of J/ψ tagged b hadrons have been studied.

Chapter 1 summarizes the theoretical inputs that motivated the measurements described in this thesis. It contains a brief description of the SM, the relevant heavy flavor phenomenology and a summary of the J/ψ and ψ' production mechanisms and their

expected rates at the Z resonance.

Chapter 2 contains a description of LEP and the L3 experiment, with which the data for this thesis was collected.

Chapter 3 is devoted to the event selection procedure and the purity and efficiency for tagging J/ψ mesons obtained thereof.

Chapter 4 is devoted to the measurement of J/ψ and ψ' production at LEP. The determination of the total J/ψ production rate is followed by limits on ψ' production and non-b production of the J/ψ mesons. Finally, the determination of $Br(b \rightarrow J/\psi + X)$ is described.

Chapter 5 contains the measurements of some properties of b hadrons tagged using the J/ψ . The method to estimate the b hadron four vector is described. Next the determination of the b quark fragmentation parameter ϵ_b is explained. This is followed by the measurement of J/ψ alignment.

Chapter 6 describes the determination of the average b hadron lifetime, τ_b . The value of τ_b is further used to determine the CKM matrix element V_{cb} .

Finally, the results obtained in this thesis, their implications and prospects are discussed.

Chapter 1

Theory

1.1 Introduction

This chapter is devoted to the theoretical and phenomenological inputs which motivated the measurements in this thesis. A brief overview of the Standard Model follows. Next heavy flavor decay, lifetimes and fragmentation are described. Subsequently, some properties of the J/ψ and ψ' mesons are described. The chapter ends with a description of the production mechanisms of ψ' and J/ψ at LEP energies.

1.2 An Overview of the Standard Model

Understanding the composition of the universe involves the identification of the basic particles, knowledge of the forces the particles feel and then ascertaining the behaviour of the particles given the forces. The Standard Model [1] (SM), based on the gauge group $SU_C(3) \times SU_L(2) \times U_Y(1)$, has been successful in providing answers to all three facets of the problem. Quarks and leptons, together referred to as the 'fundamental fermions', are the basic constituents of matter. They are considered to be pointlike particles. Quarks carry the 'color' charge whereas the leptons do not. Table 1.1 lists the forces matter is subject to and their transmitters. These transmitters called the "gauge bosons" are the second class of particles. In addition, a third kind of particle, the scalar Higgs boson, is attributed to be responsible for the masses of the fermions and the gauge bosons. It has not been observed yet and the understanding of this mechanism remains one of the most fundamental problems facing particle physicists.

In the Standard Model the left handed quarks and leptons are arranged in three weak isospin doublets; the right handed ones are arranged in singlets. There is no evidence for the existence of right-handed neutrinos. The number of families is not fixed; experimental measurements point to the existence of three families [4]. Table 1.2 lists the properties of the three families, where N_c is the number of colors. The τ neutrino has evaded experimental observation yet.

The properties of the mediators of the electromagnetic, weak and strong interactions,

Force	Acts on	Transmitter
gravity	all particles	graviton
electromagnetism	electrically charged particles	photon (γ)
weak interaction	fermions and gauge bosons	W^\pm, Z
strong interaction	quarks and gluons	gluons (g)

Table 1.1: Forces and their transmitters.

Family	Flavor	Spin	Charge ($ e $)	N_c	Mass(MeV)
1	u	$1/2$	$2/3$	3	200 – 880
	d	$1/2$	$-1/3$	3	150 – 500
	e	$1/2$	-1	1	0.511
	ν_e	$1/2$	0	1	$\simeq 0$
2	c	$1/2$	$2/3$	3	1300 – 1700
	s	$1/2$	$-1/3$	3	100 – 300
	μ	$1/2$	-1	1	105.6
	ν_μ	$1/2$	0	1	$\simeq 0$
3	t	$1/2$	$2/3$	3	$\geq 130 \times 10^3$
	b	$1/2$	$-1/3$	3	4700 – 5300
	τ	$1/2$	-1	1	1784.1
	ν_τ	$1/2$	0	1	$\simeq 0$

Table 1.2: The fermions and their properties[3].

namely the photon, the three massive vector bosons, the W^\pm and Z and the eight massless gluons, respectively are listed in Table 1.3.

	Spin	Charge	Color	Mass (GeV)
γ	1	0	no	0
Z	1	0	no	91.181
W^\pm	1	± 1	no	≈ 80.6
g_i ($i = 1, \dots, 8$)	1	0	yes	0

Table 1.3: The properties of interaction carriers, where the Z mass is taken from the L3 measurement.

The interactions of the $SU_L(2) \times U_Y(1)$ gauge field are specified by the electroweak theory [5]. In terms of the electric charge and the weak mixing angle θ_W , the couplings of the fermions to the massive W^\pm and Z bosons and the photon are given by:

$$\begin{aligned}
 \bullet \quad & \text{Diagram: A wavy line labeled } \gamma \text{ splits into two fermion lines labeled } f \text{ and } \bar{f}. & = & -ieQ_f\gamma_\mu \\
 \bullet \quad & \text{Diagram: A dashed line labeled } Z \text{ splits into two fermion lines labeled } f \text{ and } \bar{f}. & = & ie\gamma_\mu(v_f - a_f\gamma_5)\frac{1}{2\sin\theta_W\cos\theta_W} \\
 \bullet \quad & \text{Diagram: A wavy line labeled } W^\pm \text{ splits into two fermion lines labeled } f \text{ and } \bar{f}'. & = & ie\gamma_\mu(1 - \gamma_5)\frac{1}{2\sqrt{2}\sin\theta_W}
 \end{aligned}$$

where γ_i are the Dirac γ -matrices. The vector and axial vector coupling constants are defined by:

$$v_f = I_{3f} - 2Q_f\sin^2\theta_W \quad a_f = I_{3f} \quad (1.1)$$

Here, f refers to the particular fermion, Q_f is the fermion charge, and I_{3f} is the third component of fermion weak isospin. The mixing angle θ_W is given by the Z and W^\pm masses:

$$\sin^2\theta_W = 1 - \frac{M_W^2}{M_Z^2} \quad (1.2)$$

Unlike the electromagnetic and strong interactions, flavor is not conserved in weak interactions. The charge $-1/3$ weak eigenstates, d', s', b' are mixtures of the strong mass eigenstates, d, s, b and one thus has decays consisting of transitions between the generations. The mixed eigenstates are related to the flavour eigenstates by the Cabbibo-Kobayashi-Maskawa matrix [6]:

$$\begin{pmatrix} d' \\ s' \\ b' \end{pmatrix} = \begin{pmatrix} V_{ud} & V_{us} & V_{ub} \\ V_{cd} & V_{cs} & V_{cb} \\ V_{td} & V_{ts} & V_{tb} \end{pmatrix} \begin{pmatrix} d \\ s \\ b \end{pmatrix} \quad (1.3)$$

Each of the nine complex elements in this matrix represents the coupling of a charge $2/3$ quark to a charge $-1/3$ quark. The elements of this matrix are fundamental parameters of matter and it is a prime task of experimentalists to measure them. The present experimental status of the elements of this matrix is shown in Table 1.4. Assuming that the CKM matrix is unitary, it can be expressed in terms of four parameters - three mixing angles and one CP violating phase. If the neutrinos are indeed massless, there is no analogous mixing in the leptonic sector.

Element	Experimental value	Method
$ V_{ud} $	0.9744 ± 0.0010	nuclear β decay
$ V_{us} $	0.2205 ± 0.0018	K_{e3}^+ and K_{e3}^0 decay
$ V_{cd} $	0.204 ± 0.017	Neutrino dilepton production
$ V_{cs} $	1.0 ± 0.20	$D \rightarrow K e \nu$
$ V_{cb} $	0.043 ± 0.007	B meson decay
$ V_{ub} $	$(0.10 \pm 0.03) V_{cb} $	B meson decay

Table 1.4: Experimental values of the elements of the CKM matrix[3].

The SU(3) part of the standard model is a gauge theory of the strong interaction and is referred to as quantum chromodynamics (QCD) [7]. Each quark flavor comes in three colors while the leptons are colorless. The 8 generators of the SU(3) correspond to an octet of gauge bosons, the gluons, which are flavor neutral. Since the SU(3) symmetry is unbroken, the gluons are massless. One of the features of QCD is gluon self coupling which leads to the property of asymptotic freedom - the strength of the coupling in QCD depends on the distance scale of the interaction, i.e., the effective coupling decreases with the square of the four-momentum transfer. The same is true for SU(2) but the converse holds for U(1) where the coupling becomes stronger with energy.

1.3 Heavy Flavor Decay

The simplest description of the weak decays of heavy flavor mesons is given by the spectator model, illustrated in Figure 1.1. The initial state meson is represented by its valence quark configuration. The heavy quark Q (c or b), moves freely and decays into a lighter quark via the emission of a W boson. The other quark acts as a 'spectator' and has no

influence on the meson decay. The dominant weak charge-changing transition of the b quark is to the c quark and a virtual W boson and less frequently to the u quark. In the case of charmed mesons, the dominant transition is to the s quark and a small fraction to the d quark, both again via W emission.

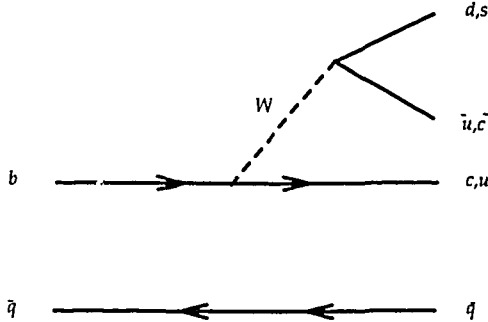


Figure 1.1: Heavy meson decay in the spectator model

The test for the suitability of the spectator model would be the measurement of the lifetimes and the semileptonic branching ratios of the various charged and neutral heavy mesons. They would be the same for all mesons if indeed the model provides an appropriate framework for the decay of heavy flavor mesons. However, the observed lifetime differences of charm hadrons [8],

$$\tau(D^+) : \tau(D^0) : \tau(\Lambda_c^+) : \tau(\Xi_c^+) : \tau(\Omega_c^0) \sim 2.5 : 1 : 1 : 0.5 : 1.3 : 1.9, \quad (1.4)$$

obliges one to consider non-spectator mechanisms arising from W exchange or weak annihilation, quark interference and the absence of “color suppression” due to soft gluon effects. These non-spectator effects have been predicted to decrease with some power in $1/m_Q$, where m_Q is the mass of the heavy quark. Thus, they should be less important for the heavier bottom quark decays. Therefore, it might be justified to use the spectator model in bottom decays, further refined by taking into account phase space corrections due to finite quark and lepton masses and QCD corrections arising from virtual gluon exchanges and real gluon emissions.

The semileptonic decay rate is then given by:

$$\Gamma_{sl}(Q \rightarrow ql\bar{\nu}_l) = |V_{qQ}|^2 f_q(\epsilon) \frac{G_F^2 m_Q^5}{192\pi^3} \quad (1.5)$$

Here, $|V_{qQ}|$ are the elements of the CKM matrix, G_F is the Fermi coupling constant, $f_q(\epsilon)$ is the product of the phase space and QCD corrections with $\epsilon = m_q/m_Q$. The phase space

and QCD corrections can be approximated by [67]:

$$f_q^{\text{PS}}(\epsilon) = 1 - 8\epsilon^2 + 8\epsilon^6 - \epsilon^8 - 24\epsilon^4 \ln \epsilon, \quad (1.6)$$

and

$$f_q^{\text{QCD}} = 1 - \left[\frac{2\alpha_s(m_b^2)}{3\pi} \right] \left[\left(\pi^2 - \frac{31}{4} \right) (1 - \epsilon)^2 + \frac{3}{2} \right] \quad (1.7)$$

For massless final states $f_q^{\text{PS}} = 1$ while $f_q^{\text{QCD}} \rightarrow 1$, if the strong interaction could be switched off.

1.4 B Lifetime and the Determination of $|V_{cb}|$

The total width for the decay of b quarks can be broken up into two terms, one for semileptonic decays and one for hadronic decays:

$$\Gamma_{\text{tot}} = \Gamma_{sl} + \Gamma_{had} \quad (1.8)$$

The lifetime is simply the reciprocal of the total width and can be related to the width of a specific channel in terms of the branching ratio for that channel:

$$\tau_b = \frac{1}{\Gamma_{\text{tot}}(b)} = \frac{Br_{sl}}{\Gamma_{sl}} \quad (1.9)$$

Since the semileptonic channels suffer the least from theoretical and experimental uncertainties, they are chosen here.

The decay rate within the framework of the spectator model is given by Equation 1.5. In the SM, b quarks decay into u and c quarks and hence, τ_b measures a combination of $|V_{ub}|^2$ and $|V_{cb}|^2$. It is also known from fits to prompt lepton spectra at the Υ_{4S} , the $b\bar{b}$ resonance, that $|V_{ub}|^2 \ll |V_{cb}|^2$ ($|V_{ub}|^2/|V_{cb}|^2 \sim 10^{-2}$). Thus, a measurement of τ_b can be used to determine $|V_{cb}|$ by the following relation:

$$|V_{cb}|^2 = \frac{BR(b \rightarrow \mu\nu X)}{\tau_b} \times \left[\left(\frac{G_F^2 m_b^5}{192\pi^3} \right) \left(f_c + f_u \frac{|V_{ub}|^2}{|V_{cb}|^2} \right) \right]^{-1} \quad (1.10)$$

1.5 Heavy Flavor Fragmentation

Figure 1.2 shows the configuration of a typical multihadronic e^+e^- annihilation event. In the first phase, an e^+e^- pair annihilates into a virtual γ/Z resonance, which produces a primary $q\bar{q}$ pair. Before the annihilation, initial state QED bremsstrahlung may occur reducing the mass of the hadronic final state from the naïve value. This phase is mainly given by electroweak perturbation theory. In the second phase, the initial $q\bar{q}$ pair may radiate gluons, which may radiate themselves. Strong perturbation theory has to be invoked to describe this phase. Since the strong coupling constant is larger than the weak one, the degree of accuracy in the description is less, especially for soft parton emission.

The third phase when the colored partons reorganize themselves into colorless hadrons is referred to as *fragmentation*. This process can be deduced qualitatively from QCD but a rigorous quantitative understanding is lacking due to its complex nature. In the fourth phase, unstable hadrons decay into the experimentally observable particles. The underlying theories here are QCD and QED but this again is a realm where QCD predictions are simplistic and the main input comes from experimentally determined branching ratios. Detectors are set up to identify and measure the energy/momenta of the particles produced at this stage and reconstruct the primary hard process.

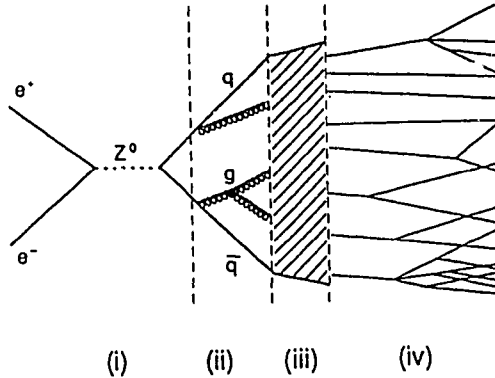


Figure 1.2: Schematic illustration of the time evolution of an e^+e^- event.

The prediction of the energy spectra of heavy flavor hadrons is of primary importance for tagging them and measuring their lifetime, mixing, oscillations, etc. In contrast to light-quark hadronization, the fragmentation of heavy quarks is hard because the inertia of the heavy quark is retained in the hadrons [9]. Also, gluon radiation from heavy quarks is suppressed, leaving more energy to the leading particle than in light quark jets. Hard fragmentation for b and c quarks has been observed in many experiments [10].

Since the fragmentation process is not exactly calculable, various phenomenological models have evolved to describe it. There are three main schools - independent fragmentation (IF), string fragmentation (SF) and cluster fragmentation (CF).

The IF [11] approach assumes that the fragmentation of any system of partons can be described as an incoherent sum of independent fragmentation procedures for each parton separately. The SF [12] scheme is the combination of fragmentation with the concept of the color string, which is stretched from the quark via the gluon to the anti-quark. This color string is envisaged to break first to produce a hadron carrying a sizeable fraction

of the gluon energy. The remainder of the gluon energy is then shared between the two pieces of the broken string, which are fragmented independently in their respective center-of-mass systems. Both these models employ an iterative ansatz and the process stops when only on shell hadrons remain. For the sharing of energy and momentum at each step, both the models employ probability distributions $f(z)$, called fragmentation functions, where

$$z = \frac{(E + P_{\parallel})_{\text{hadron}}}{(E + P_{\parallel})_{\text{quark}}}. \quad (1.11)$$

For the light quarks (u, d, s), the Field-Feynman parametrization [11]

$$f(z) = 1 - a + 3a(1 - z)^2 \quad (1.12)$$

is commonly used with $a = 0.77$.

Since, charm and bottom data clearly indicate the need for a harder fragmentation function, the Peterson et. al. formula [14]

$$f(z) = \frac{1}{z} \left(1 - \frac{1}{z} - \frac{c_q^2}{1 - z} \right)^{-2} \quad (1.13)$$

is widely employed. Here, c_q^2 is a free parameter and its value is expected to decrease with the increase in the quark masses, i.e., $c_q^2 \propto 1/m_q^2$.

In the CF [13] approach, gluons from the perturbative phase are first split into quark and anti-quark pairs which then form colorless clusters. These clusters, depending upon their masses, either decay into lower class clusters or directly into particles. In this scheme, the distributions of particle momenta are determined by those of the parent cluster and its decay properties. No extra parameters are needed for hadronization.

1.6 $c\bar{c}$ Spectroscopy

The discovery of the J/ψ in 1974 is referred to as the *November Revolution*. By providing the first evidence of the existence of the theoretically postulated fourth quark [16], it heralded a new era in the field of particle physics. Both at Brookhaven [17] and SLAC [18], a resonance of mass 3.1 GeV was discovered with an extremely narrow width, $\Gamma \sim 70$ keV. Some theorists were quick to predict that given the interpretation that the J/ψ was a $q\bar{q}$ meson in an orbital s -wave and a spin triplet state, the first radial excitation should be 600 MeV higher in energy. Sure enough, the predicted state, the ψ' , was immediately found and the interpretation in terms of the fourth quark became the dominant one. The J/ψ is interpreted as the $1^3 S_1$ state and the ψ' is the $2^3 S_1$ state of the bound system of the charmed quark c and its antiparticle \bar{c} . Subsequently, other energy levels of the charmonium were also discovered. Figure 1.3 shows the energy states of charmonium system relevant to this thesis and the allowed transitions between them as interpreted by the charmonium model.

The charmonium system and, quarkonia in general, are akin to positronium except that the binding potential to be used in this case is not obvious. At short range a Coulombic

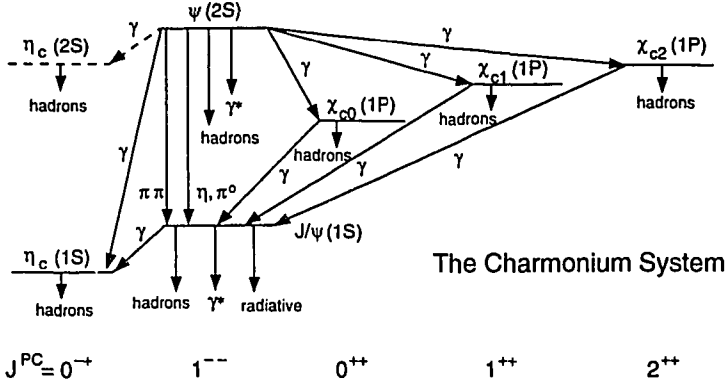


Figure 1.3: The energy levels of the charmonium system.

potential, $V \sim 1/r$, is expected. At large distances, the potential must increase without limit to account for quark confinement. The functional form of $V(r)$ is speculative at large r and different functional forms have been used. Some authors prefer a harmonic oscillator potential, $V \sim r^2$, others a logarithmic dependence, $V \sim \ln(r)$ and still others a linear potential $V \sim r$ [19]. Quarkonia can only be studied theoretically in the non relativistic limit since an exact solution of the relativistic bound state problem is not available. This approximation works well for the heavy quarks because the binding energy in this case is actually negligible compared to the constituent masses.

1.6.1 The ψ' and J/ψ Mesons

Some properties of the J/ψ and ψ' mesons are listed in Tables 1.5. The decay modes of the ψ' and J/ψ mesons are listed in Table 1.6.

	ψ'	J/ψ
Mass	$3686.00 \pm 0.10 \text{ MeV}$	$3096.93 \pm 0.09 \text{ MeV}$
Width	$278 \pm 32 \text{ keV}$	$85.5^{+6.1}_{-5.8} \text{ keV}$

Table 1.5: The Properties of the ψ' and J/ψ mesons[3].

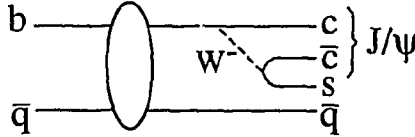
In the analysis presented in this thesis, the ψ' and J/ψ mesons are both tagged via their decays into a muon pair, i.e., $\psi' \rightarrow \mu^+\mu^-$ and $J/\psi \rightarrow \mu^+\mu^-$.

Mode	ψ'	J/ψ
$\Gamma_1 : \text{hadrons}$	$(98.10 \pm 0.30)\%$	$(86.0 \pm 2.0)\%$
$\Gamma_2 : e^+e^-$	$(8.8 \pm 1.3) \times 10^{-3}$	$(6.27 \pm 0.20)\%$
$\Gamma_3 : \mu^+\mu^-$	$(7.7 \pm 1.7) \times 10^{-3}$	$(5.97 \pm 0.25)\%$

Table 1.6: ψ' and J/ψ decay modes[3].

1.7 ψ' Production at the Z Pole

The only accessible production mechanism for ψ' mesons at the integrated luminosity available for this thesis is its production via the decay of b hadrons. The $b(\bar{b})$ decay to produce the ψ' mesons proceeds through a “color-suppressed” spectator diagram in which the c and \bar{c} have to match in color as shown in Figure 1.4. This leads to an expected suppression of $1/9$ in this decay due to color mismatch. QCD effects may reduce or enhance this suppression. Fritzsche[20] argued that the color suppression may or may not be effective due to color mismatch by soft gluons. On the other hand, virtual gluon exchanges[21,23,24] modify the effective Hamiltonian, which leads to a larger suppression. Experimental measurements of the branching ratio for the process are essential for further guidance.

Figure 1.4: “Color suppressed” spectator diagram for the production of J/ψ and ψ' mesons via b decay.

The width for $c\bar{c}$ vector meson production in b decays can be calculated in analogy with that for the decay $\tau^- \rightarrow \rho^- \nu_\tau$. The width for ψ' production is then given by Wise [21] as:

$$\Gamma_{b \rightarrow \psi' + s} = \frac{G_F^2}{12\pi^2} |V_{bc}|^2 |V_{cs}|^2 |R(0)|^2 \left(\frac{m_{\psi'}}{m_b} \right) \left(\frac{m_b^2 - m_{\psi'}^2}{2m_b} \right)^2 \times \left[2 + \frac{m_b^2}{m_{\psi'}^2} \right], \quad (1.14)$$

where $|R(0)|$ is the radial wave function of the ψ' meson in its rest frame evaluated at the origin, $|V_{bc}|$ and $|V_{cs}|$ are the CKM matrix elements and G_F is the Fermi decay constant. The “color suppression” factor $1/9$ is implicit in the above expression.

The value of $|R(0)|$ is related to the leptonic decay width by the Royen-Weisskopf

formula modified to include first-order QCD corrections [22]:

$$\Gamma(n^3S_1 \rightarrow l\bar{l}) = 4e_Q^2\alpha^2 \frac{|R_{nS}(0)|^2}{M_n^2} \left\{ 1 - \frac{16}{3} \frac{\alpha_s}{\pi} \right\} \left(1 + \frac{2m_l^2}{M_n^2} \right) \sqrt{1 - \frac{4m_l^2}{M_n^2}}, \quad (1.15)$$

where m_l is the lepton mass, M_n is the quarkonium mass and e_Q is the quark charge (2/3 in this case). Using the measured values of $\Gamma(\psi' \rightarrow e^+e^-) = 2.14 \pm 0.21$ keV, we get $|R(0)|^2 = 0.5 \text{ GeV}^3$ for the ψ' .

Further, using $G_F = 1.166 \times 10^{-5} \text{ GeV}^{-2}$ and $m_b = 4.95 \text{ GeV}$, we get

$$\Gamma_{b \rightarrow \psi' + s} = 2.0 \times 10^{-12} |V_{bc}|^2 |V_{cs}|^2 \text{ GeV} \quad (1.16)$$

For an estimate of $Br(b \rightarrow \psi' + X)$, one needs to estimate the total width of the b quark. From Equations 1.10 and 1.11 we find

$$\Gamma_b = \frac{G_F^2 m_b^5}{192\pi^3} |V_{bc}|^2 (f_c + f_u \frac{|V_{ub}|^2}{|V_{cb}|^2}) \frac{1}{Br(b \rightarrow \mu\nu X)} \quad (1.17)$$

with f_c and f_u as defined in Equation 1.5. Evaluation (see Section 6.6 of this thesis) leads to:

$$\Gamma_b = 2.7 \times 10^{-10} |V_{cb}|^2 \quad (1.18)$$

Combining Equations 1.16 and 1.18, we get

$$Br(b \rightarrow \psi' + X) = \frac{\Gamma(b \rightarrow \psi' + X)}{\Gamma_b} \approx 0.7\% \quad (1.19)$$

The branching ratio $Br(Z \rightarrow b\bar{b}; b(\bar{b}) \rightarrow \psi' + X)$ is given by:

$$Br(Z \rightarrow b\bar{b}; b(\bar{b}) \rightarrow \psi' + X) = \frac{2\Gamma_{b\bar{b}}}{\Gamma_Z} \times Br(b \rightarrow \psi' + X) \quad (1.20)$$

Using the Standard Model value of $\Gamma_{b\bar{b}}/\Gamma_Z$ of 15% we get:

$$Br(Z \rightarrow b\bar{b}; b(\bar{b}) \rightarrow \psi' + X) = 2.1 \times 10^{-3}. \quad (1.21)$$

1.8 J/ψ Production Mechanisms at the Z Pole

At LEP energies, J/ψ mesons can be produced by the following processes:

1. Decays of higher charmonium states
2. $Z \rightarrow b\bar{b}; b(\bar{b}) \rightarrow J/\psi + X$
3. $Z \rightarrow q\bar{q}g^*; g^* \rightarrow J/\psi + X$
4. $Z \rightarrow c\bar{c}J/\psi$

5. $Z \rightarrow J/\psi gg$

6. $Z \rightarrow J/\psi \gamma$

The measurement of the branching ratio for each of these processes is of great importance since they provide information on the interplay between weak and strong interactions. Process (2), which is the dominant mode for J/ψ production, is also a good mode to tag b hadrons [20]. Measurements of $Br(b \rightarrow J/\psi + X)$ have been performed at CESR and DORIS [8] and it will be useful to compare the production rate of J/ψ at LEP energies to those at $\Upsilon(4S)$.

The mechanisms and expected branching ratios for all the production processes are described in the following sections.

1.8.1 Decays of higher charmonium states

Table 1.7 lists the branching ratios for higher charmonium states into J/ψ mesons relevant to this thesis. The production rate of charmonium states from processes other than b hadron decays is negligible. In a model by Kuhn et al [23] the b-decay width into charmonium states is estimated from expressions for the charmonium continuum and meson form factors. A vector meson form factor is needed in case of vector decay, and an axial vector meson or pseudoscalar form factor in case of axial vector decay. The relative abundance of charmonium states in b hadron decays is estimated to be:

$$\eta_c : J/\psi : P_c | \chi_{1c} : \psi' \cong 0.57 : 1 : 0.27 : 0.31 \quad (1.22)$$

b hadron decays into the states χ_{0c} , χ_{2c} and the 1P_1 states are forbidden. Given the production rate of the various charmonium states in b hadron decays and the branching ratios of the higher charmonium states into J/ψ mesons, one can expect 18% of the J/ψ to be products of ψ' decays and 7% to be products of the χ_{c1} decays. Thus, $\sim 75\%$ J/ψ mesons are expected to be direct products of b hadron decays.

Mode	Fraction (Γ_j/Γ)
$\psi' \rightarrow J/\psi + X$	$(57 \pm 4)\%$
$\chi_{c1} \rightarrow J/\psi + \gamma$	$(27.3 \pm 1.6)\%$

Table 1.7: J/ψ production via the decay of higher charmonium states[3].

1.8.2 $Z \rightarrow b\bar{b}; b(\bar{b}) \rightarrow J/\psi + X$

This is the dominant mechanism for the production of J/ψ mesons in Z decays. The mechanism by which the production proceeds is exactly the same as for ψ' production via the decay of b hadrons as described in Section 1.7. The results from CLEO and ARGUS on the $Br(b \rightarrow J/\psi + X)$ provided the first evidence of color selection rules in bottom

decays [24]. The measured production rate was of the order of 1% whereas the predicted rate was of the order of 3 – 5% [20].

The width for J/ψ production in b decays can be calculated using Equation 1.14 where $|R(0)|$ is the radial wave function of the J/ψ meson in its rest frame evaluated at the origin. Using $|R(0)|^2 = 0.8 \text{ GeV}^3$ computed using Equation 1.15 with $\Gamma(J/\psi \rightarrow e^+e^-) = 5.36^{+0.29}_{-0.28} \text{ keV}$ [3, 56], we get

$$\Gamma_{b \rightarrow J/\psi + s} = 5.9 \times 10^{-12} |V_{bc}|^2 |V_{cs}|^2 \text{ GeV} \quad (1.23)$$

Combining Equations 1.23 and 1.18 we get

$$Br(b \rightarrow J/\psi + X) = \frac{\Gamma(b \rightarrow J/\psi + X)}{\Gamma_b} \approx 2.2\% \quad (1.24)$$

As remarked above, this estimate of the branching ratio is uncertain because of QCD effects.

The branching ratio $Br(Z \rightarrow b\bar{b}; b(\bar{b}) \rightarrow J/\psi + X)$ is given by:

$$Br(Z \rightarrow b\bar{b}; b(\bar{b}) \rightarrow J/\psi + X) = \frac{2\Gamma_{b\bar{b}}}{\Gamma_Z} \times Br(b \rightarrow J/\psi + X) \quad (1.25)$$

Using the Standard Model value of $\Gamma_{b\bar{b}}/\Gamma_Z$ of 15% we get:

$$Br(Z \rightarrow b\bar{b}; b(\bar{b}) \rightarrow \psi' + X) = 6.4 \times 10^{-3}. \quad (1.26)$$

1.8.3 $Z \rightarrow q\bar{q}g^*; g^* \rightarrow J/\psi + X$

The early estimates [25] for this cross section illustrated in Figure 1.5 were based on local duality; i.e., a certain fraction of the $g^* \rightarrow c\bar{c}$ decays with $2m_c < \mu < 2m_D$, where $\mu \equiv m(g^*)$, was identified with J/ψ production, after allowance was made for the color mismatch. The uncertainties in the duality estimates were large and an explicit calculation has been performed in [26]. The total cross section for producing the charmonium state J/ψ , from gluon jets is calculated [26] through the following relation:

$$\sigma(e^+e^- \rightarrow q\bar{q}g^*; g^* \rightarrow J/\psi X) = \int_{M_{J/\psi}}^s d\mu^2 \sigma(e^+e^- \rightarrow q\bar{q}g^*(\lambda)) P(g^* \rightarrow J/\psi X) \quad (1.27)$$

where $\lambda = \mu^2/s$, where $\mu = m(g^*)$ is the mass of the virtual gluon, $\sigma(e^+e^- \rightarrow q\bar{q}g^*(\lambda))$ is the integrated cross section and $P(g^* \rightarrow J/\psi X)d\mu^2$ is the probability distribution of producing the decay $g^* \rightarrow J/\psi X$.

Using the leading order running coupling $\alpha_s(\mu^2)$ with four flavours, at LEP energies, the authors [26] predict ~ 170 J/ψ events from $q\bar{q}g^*$ followed by $g^* \rightarrow J/\psi + X$ in 10^6 hadronic decays of the Z , which corresponds to a branching ratio of

$$Br(Z \rightarrow q\bar{q}g^*, g^* \rightarrow J/\psi + X) = 1.7 \times 10^{-4} \quad (1.28)$$

A recent publication [27] which calculates the fragmentation functions for high energy partons into a quarkonium state and other partons, points out some fallacies in the computation in [26]. These authors claim that J/ψ production via charm fragmentation described in the following section (Section 1.8.4) would be larger than via gluon fragmentation.

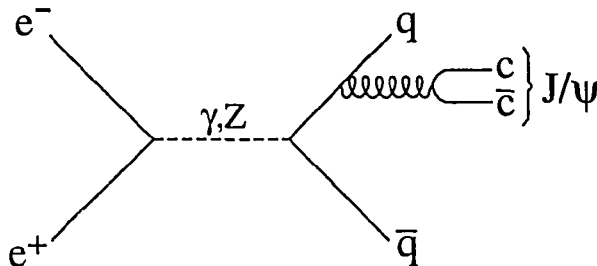


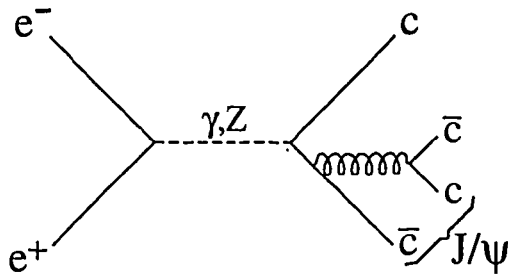
Figure 1.5: Diagram for J/ψ production from gluon jets.

1.8.4 $Z \rightarrow c\bar{c}J/\psi$

This process is of considerable interest since it involves both short-distance and long-distance aspects of QCD. The production of a $c\bar{c}$ pair with small relative momentum in Z decays is a short-distance process whereas the subsequent formation of a bound state from the $c\bar{c}$ pair is a long-distance process involving all the complications of non-perturbative QCD. The calculation for the expected branching ratio for this mechanism can be found in [28] and [29]. In this process, illustrated in Figure 1.6, a high energy charm or anticharm quark is produced followed by its splitting into a charmonium state. The amplitude for this process involves four Feynman diagrams with different attachments of the exchanged gluon. With the non-relativistic approximation and with the wave function for the J/ψ at the origin $|\Psi(0)|^2 = 0.063 \text{ GeV}^3$, the expected branching ratios as calculated in References [28] and [29] are consistent. The estimated branching ratio for this process is given by:

$$Br(Z \rightarrow c\bar{c}J/\psi) = 2.7 \times 10^{-5} \quad (1.29)$$

Thus, approximately 30 events of this kind are expected to be produced in 10^6 Z decays.

Figure 1.6: Diagram for J/ψ production via charm fragmentation.

1.8.5 $Z \rightarrow J/\psi g(g)$

In this mechanism since J/ψ is produced in conjunction with one or more gluons and the J/ψ can be cleanly tagged via its decay into lepton pairs, it opens up the possibility of unambiguous study of gluon properties.

Two different classes of models have been proposed to study this decay. In the Color Evaporation Model (CEM) [30], the production of a pair of charmed quarks with an invariant mass between $2m_c$ and $2m_D$ is calculated with the crude assumption that roughly $1/8 - 1/3$ of these pairs would convert into a J/ψ . The color content of the quark is ignored since by radiating off an arbitrary number of soft gluons, the $c\bar{c}$ pair can be a color singlet state. The Feynman diagram for the process is illustrated in Figure 1.7. The predicted branching ratio from this model is

$$Br(Z \rightarrow J/\psi g) \approx 10^{-5} \quad (1.30)$$

On the other hand, the Color Singlet Model (CSM) [31] assumes that perturbative QCD describes the formation of the $J/\psi gg$ final state. In this model, the $c\bar{c}$ state is produced as a $3S_1$ color singlet state together with two gluons (Figure 1.8). The predicted branching ratio, in this case is

$$Br(Z \rightarrow J/\psi g) \approx 3 \times 10^{-7} - 3 \times 10^{-6} \quad (1.31)$$

1.8.6 $Z \rightarrow J/\psi \gamma$

The Feynman diagram for this process is illustrated in Figure 1.9. The branching ratio for this mechanism has been calculated [32] to be:

$$Br(Z \rightarrow J/\psi \gamma) \approx 3 \times 10^{-7} - 3 \times 10^{-6} \quad (1.32)$$

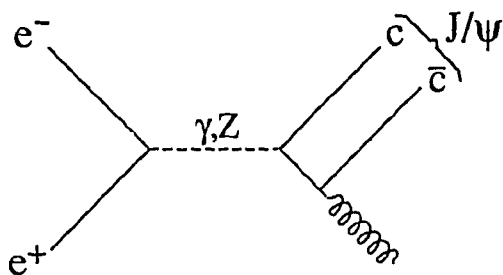


Figure 1.7: Diagram for J/ψ production via charm fragmentation in CEM.

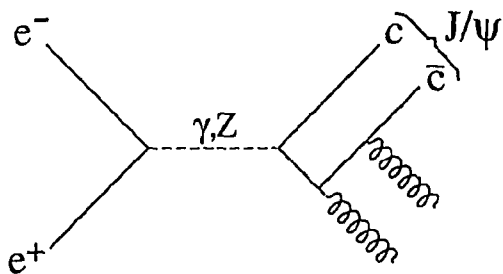


Figure 1.8: Diagram for J/ψ production via charm fragmentation in CSM.

The use of different potential models in the final computation gives rise to the uncertainty in the final result.

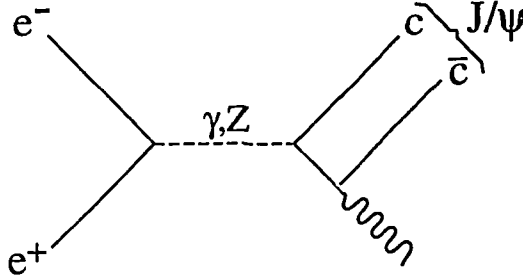


Figure 1.9: Radiative decay of Z into J/ψ .

Table 1.8 contains a list of all the production mechanisms and their expected branching ratios.

Number	Process	Branching Ratio
1	$Z \rightarrow b\bar{b}; (b\bar{b} \rightarrow J/\psi + X)$	3.2×10^{-3}
2	From ψ' and χ_{c1} decays	0.8×10^{-3}
3	$Z \rightarrow q\bar{q}g^*, g^* \rightarrow J/\psi + X$	1.7×10^{-4}
4	$Z \rightarrow J/\psi g$	1.0×10^{-5}
5	$Z \rightarrow J/\psi c\bar{c}$	2.7×10^{-5}
6	$Z \rightarrow J/\psi \gamma$	$10^{-7} - 10^{-6}$
6	$Z \rightarrow J/\psi gg$	3.0×10^{-8}

Table 1.8: Expected branching ratios of different processes producing J/ψ in Z decays.

Chapter 2

The L3 Experiment

2.1 Introduction

The data for the analysis presented in this thesis was collected with the L3 detector at the LEP (Large Electron Positron) collider. This chapter briefly describes the LEP collider and the components of the L3 detector. This is followed by an outline of the triggers used for the data acquisition. Lastly, there is a brief description of the L3 data reconstruction and simulation.

2.2 LEP

The Large Electron Positron collider LEP at CERN is situated in a circular tunnel of 27 km circumference on both sides of the border between France and Switzerland (Figure 2.1); it has been operational since 1989. The tunnel is between 50 and 170 m below the surface and its diameter is 3.8 m .

The collider consists of eight bending sections, each 2840 m long, with 3304 dipole magnets to guide the beam. At 45 GeV beam energy, the required field is 0.048 T. There are eight 500 m straight sections, four of which house the four experiments - ALEPH [33], DELPHI [34], L3 [35] and OPAL [36]. Four ~ 1 cm long bunches of electrons and four similar bunches of positrons circulate in opposite directions in the beam pipe and collide at these four interaction points. LEP is designed to provide center-of-mass energies upto 200 GeV with a luminosity of $\mathcal{L} = 10^{31} \text{cm}^{-2}\text{s}^{-1}$.

Before injection into the LEP ring, four accelerators are employed to accumulate and preaccelerate the positron and electron bunches. The LEP Injector Linacs (LIL) create the electrons and positrons in pulses of 12 ns and accelerate them up to 600 MeV. These are then accumulated in the Electron Positron Accumulator (EPA) into bunches. The Proton Synchrotron (PS) then accelerates these bunches up to 3.5 GeV followed by the Super Proton Synchrotron (SPS) which further accelerates them to 20 GeV and injects them into the LEP ring. In LEP, the beams are further accelerated to the desired energy and then brought into collision. A period with colliding beams, a fill, may last several

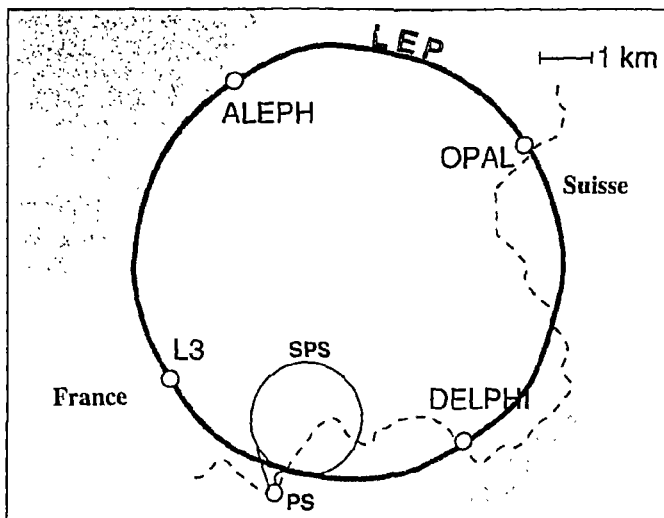


Figure 2.1: The LEP Collider Complex.

hours.

A detailed description of the LEP accelerator and injection chains can be found in the LEP design reports [37].

2.3 The L3 Detector

The L3 experiment is designed to study e^+e^- collisions up to 200 GeV with emphasis on high resolution energy measurement of electrons, photons and muons as well as good spatial and energy resolution of hadron jets. The detector is installed within a 7800 ton magnet providing a 0.5 T field. A relatively low field is chosen in a large volume to optimize the muon momentum resolution, which improves linearly with the field but quadratically with the track length. The poles of the magnet are double doors, thus enabling access to the detectors.

From the interaction point radially outwards the following detectors are installed (see figure 2.2) :

- A central track detector (Time Expansion Chamber, TEC) for the detection of charged particles and a precise measurement of the location and direction of their tracks.

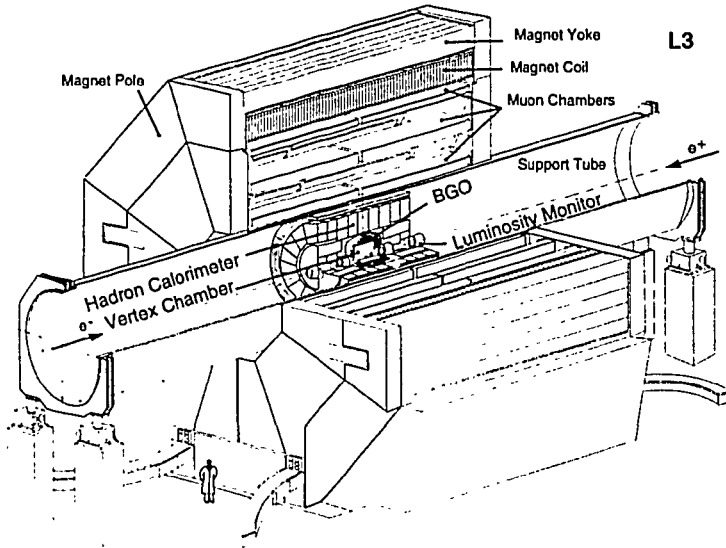


Figure 2.2: The L3 Detector.

- An electromagnetic calorimeter (BGO, named after the crystal material it is made of, $Bi_4Ge_3O_{12}$) to measure electron and photon energies.
- A scintillation counter array, used to measure the arrival time of traversing particles.
- A hadron calorimeter (HCAL), to measure the hadron energies and act as a filter to absorb the hadrons and provide a clean muon signature in the detector surrounding it. In addition, the HCAL tracks muons.
- A muon detector (MUon CHambers, MUCII) consisting of 176 large drift chambers to measure the sagitta of the muon tracks.

The detector is supported by a steel tube, 32 m long on adjustable jacks placed on concrete pillars. The tube is concentric with the LEP beam line and symmetric with respect to the interaction point which allows the alignment of all the subdetectors relative to the LEP beam. In addition, there are the luminosity monitor, the trigger system, electronics for data acquisition and a cluster of online and offline computers for the data handling.

2.4 The Central Track Detector

The TEC is a precise wire chamber which determines the location of ionization clusters caused by charged particles traversing its volume. The total lever arm for coordinate measurement in the central tracking detector is 31.7 cm radially. The charge identification of 50 GeV particles with 95% confidence level requires 50 coordinate measurements with 50 μm resolution. This is accomplished by a Time Expansion Chamber (TEC), surrounded by two cylindrical proportional chambers with cathode strip readout, the z-detector. The z direction is defined along the beam direction. (Figure 2.3). Following the TEC principle [38], the high field amplification region at the sense wire plane is separated from the low field drift region by an additional grid wire plane. The TEC operates with a low diffusion 80% CO_2 and 20% $i\text{C}_4\text{H}_{10}$ gas mixture at a pressure of 1.2 bar and a low drift velocity of 6 $\mu\text{m}/\text{ns}$. The angle between the direction of the electric field and the drift direction, the Lorentz angle, is only 2.3° for this gas mixture.

The TEC is made up of two concentric cylinders with twelve inner and twenty four outer sectors with each inner sector spanning two outer sectors. The anodes are divided into three groups according to their function - the standard optimized for $r\phi$ measurement, the charge division to provide a z coordinate measurement and the left-right for ambiguity resolution. The inner sectors each have 8 standard and 2 charge division anodes whereas the outer sectors each have 54 standard, 9 charge division and 14 left right anodes as shown in Figure 2.4. The single wire resolution in the outer sectors is 49 μm and in the inner sectors it is 57 μm . The double track resolution 600 to 800 μm . The resolution of the distance of closest approach to the interaction vertex was determined to be $120 \pm 2 \mu\text{m}$.

The z-detector consists of two thin cylindrical multiwire proportional chambers with cathode strip readout, covering the outer cylinder of the TEC. The cathode strips are inclined with respect to the beam (z-) direction by 69° and 90° for the inner chamber, and by -69° and 90° for the outer chamber. The resolution in the z measurement improves from 60 mm obtained by using the charge division wires alone to 450 μm when the z chambers are used.

Each TEC segment is equipped on its outer surface with a plastic scintillation fiber (PSF) ribbon designed to monitor the drift velocity to an accuracy of 0.1%.

In the forward region, there are Forward Tracking Chambers (FTC) measuring the position and the direction of charged particles behind the central track detector's end flange with a spatial resolution of better than 200 μm and an angular precision better than 10 mrad.

The details of the design, construction and performance of the TEC can be found in [39].

2.5 The Luminosity Monitor

In L3, the luminosity is determined from the measured rate of small-angle Bhabha scattering, $e^+e^- \rightarrow e^+e^-(\gamma)$. The polar angle θ of these events lies in the angular range defined by $31 \text{ mrad} < \theta$ or $(\pi - \theta) < 64 \text{ mrad}$. The main contribution to the small angle cross

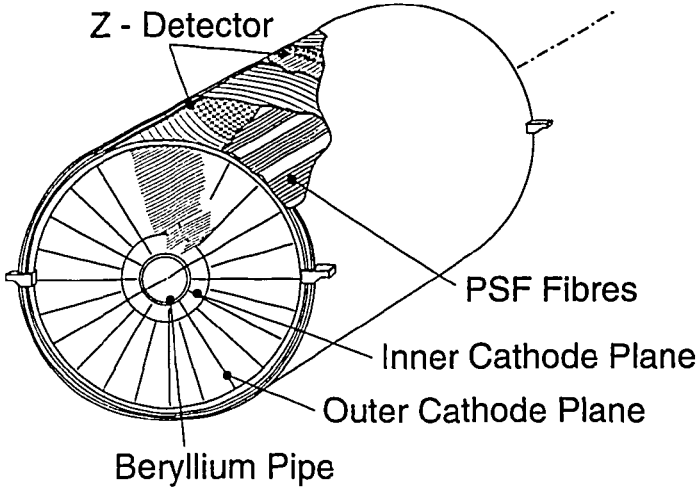


Figure 2.3: The Time Expansion Chamber.

section comes from the t-channel γ -exchange. Since the cross section and angular distribution for this process, σ_{Bhabha} , are well known from QED, the integrated luminosity, \mathcal{L}_{int} , of a running period is given by:

$$\mathcal{L}_{int} = N_{Bhabha} / \sigma_{Bhabha}, \quad (2.1)$$

where, N_{Bhabha} is the measured number of Bhabha events in the running period, corrected for possible inefficiencies.

The luminosity monitor consists of two electromagnetic calorimeters and two sets of proportional wire chambers, situated symmetrically on either side of the interaction point, at a distance of about 2.7 m. The calorimeter is a finely segmented and azimuthally symmetric array of 304 BGO crystals covering the polar angular range $25 < \theta < 70$ mrad. Each crystal is read out by a photodiode and has an LED to monitor its stability. The analog photodiode signals are used for the luminosity triggers and the digitised photodiode signals are used to determine the energy deposited in the crystals. The energy resolution of the calorimeters is about 2% at 45 GeV, and the angular resolution is 0.4 mrad in θ and 0.5° in ϕ .

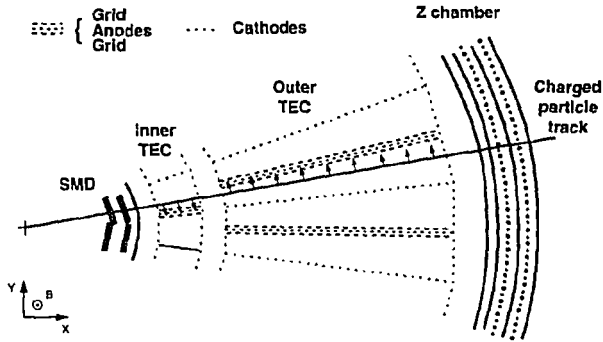


Figure 2.4: An inner and two outer TEC sectors.

2.6 The Electromagnetic Calorimeter

The electromagnetic calorimeter (ECAL) uses BGO as both the showering and detecting medium; it has excellent energy and spatial resolution for photons and electrons over a wide energy range (from 100 MeV to 100 GeV). BGO is a particularly attractive material for an electromagnetic calorimeter because it has a high stopping power (short radiation length, $X_0 = 1.12$ cm), it has a low afterglow and it is not hygroscopic.

The electromagnetic calorimeter (figure 2.5) consists of 10734 BGO crystals pointing to the interaction region. Each crystal is 24 cm long resulting in a total radiation length of $21X_0$. The calorimeter surrounds the central track detector and consists of:

- Two half barrels of BGO crystals. The 7680 crystals of the barrel are arranged in two symmetrical half barrels, giving a polar angle coverage $42^\circ < \theta < 138^\circ$.
- Two endcaps, each made of 1527 crystals with polar angle coverage $11.6^\circ < \theta < 38^\circ$. Both endcaps have a gap equivalent to the volume of three by three crystals through which a deuteron beam can be transported from the Radio Frequency Quadrupole, a device to calibrate the crystals.

The energy resolution obtained for electrons and photons is about 6% at 100 MeV and about 1% for energies above 2 GeV. The measured spatial resolution above 2 GeV is better than 1 mm.

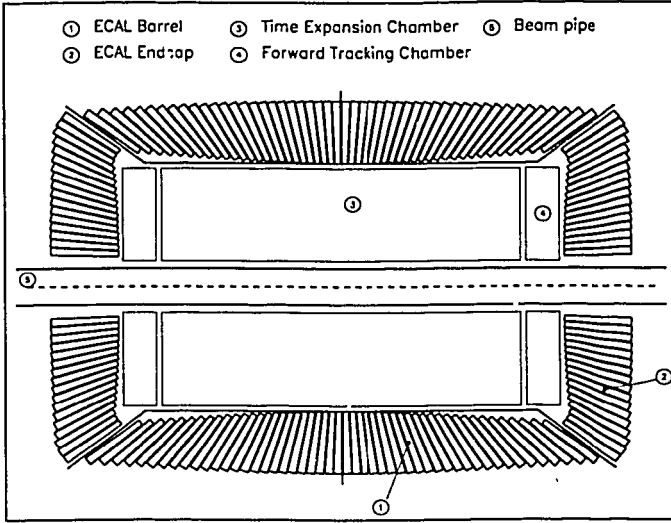


Figure 2.5: The BGO electromagnetic calorimeter.

2.7 The Scintillation Counters

The scintillation counter system consists of 30 single plastic counters. It is located between the electromagnetic and hadronic calorimeters. The polar angle coverage it provides is $|\cos \theta| < 0.83$ which is the acceptance of the middle muon chambers (MM). The azimuthal coverage is 93%. The scintillator hit multiplicity is used to trigger hadronic events.

2.8 The Hadron Calorimeter and Muon Filter

The energy of hadrons emerging from e^+e^- collisions is measured by the total absorption technique with an electromagnetic and a hadron calorimeter (HCAL). The hadron calorimeter is divided into a barrel part (HIBAR) covering the central region ($35^\circ \leq \theta \leq 145^\circ$) and a forward-backward part (HICAP) covering $5.5^\circ \leq \theta \leq 35^\circ$ (see figure 2.6). The azimuthal coverage of the barrel and the endcaps is $\sim 2\pi$. It is a fine sampling calorimeter made of depleted uranium absorber plates interspersed with proportional wire chambers. It acts as a calorimeter as well as a filter, allowing only non-showering particles to reach the precision muon chambers. Uranium has a short absorption length maximizing the amount of absorber material in the available space and since it is radioactive, it acts as a

built in gamma source for the calibration of the wire chambers.

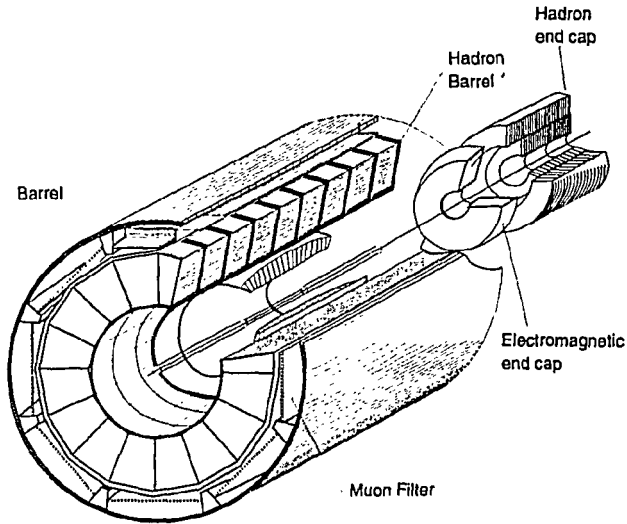


Figure 2.6: The hadron calorimeter.

The HBAR has a modular structure consisting of 9 rings of 16 modules each. The modules in the three inner rings are longer than the other ones. The wires in each module are grouped to form readout towers. In the ϕ projection the towers point to the beam axis with a constant angular interval. The segmentation is 16 in ϕ , 9 in z and 10 (8) in the radial direction for the long (short) modules. The thickness, including the electromagnetic calorimeter and support structure, varies between 5.9 and 7.2 nuclear absorption lengths in the barrel part. Each endcap consists of three separate rings - an outer ring and two inner rings. Each ring is split vertically into two half rings, resulting in a total of 12 separate modules. The amount of material traversed by a particle originating at the interaction point varies between 6 and 7 absorption lengths in the endcap region.

A muon filter is mounted on the inside wall of the support tube; it adds 1.03 absorption lengths to the hadron calorimeter. It consists of eight octants, each made of six 1 cm thick brass (65% Cu and 35% Zn) absorber plates, interleaved with five layers of proportional tubes and followed by 1.5 mm thick absorber plates matching the circular shape of the support tube.

The fine segmentation of the calorimeters allows the measurement of the axis of jets with an angular resolution of approximately 2.5° and of the total energy of hadronic

events from Z decays of better than 10%. The details of the design and performance of the HCAL can be found in [48].

2.9 The Muon Detector

The L3 muon detector(MUCH) has been designed [41] to measure high energy muons with an accuracy of $\Delta p/p = 2\%$ at 50 GeV, thus providing a 1.4% dimuon mass resolution at 100 GeV. This is achieved with a configuration of three layers of drift chambers which measure the curvature of the muon trajectory very precisely in the region between the support tube and the magnet coil. In this region, the 0.5 T magnetic field makes a 50 GeV muon track deviate from a straight line by a sagitta, $s = 3.4\text{mm}$. To get $\Delta m/m = 1/\sqrt{2} \times \Delta p/p = 1.4\%$, $\Delta s/s$ must be measured to 2%, i.e., $\Delta s \sim 70\mu\text{m}$.

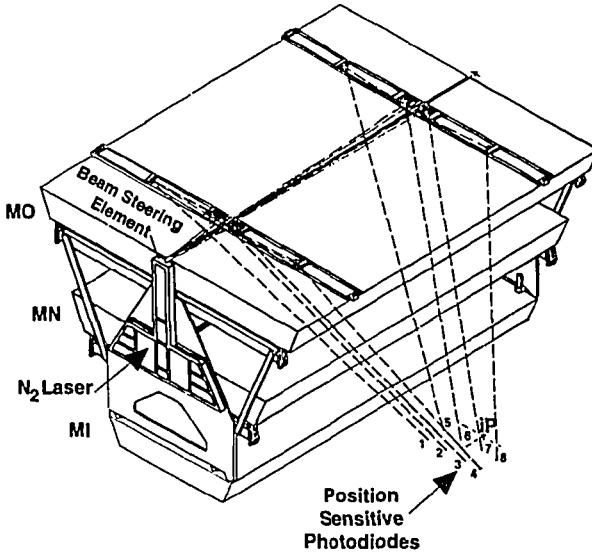


Figure 2.7: A muon chamber octant on its stand.

The muon detector consists of two “ferris” wheels, each weighing 86 tons and comprising eight independent units or octants. Each octant (Figure 2.7) consists of a special mechanical structure supporting five precision chambers. There are two chambers (MO) in the outer layer, two chambers (MM) in the middle layer and one inner (MI) chamber. These chambers measure the track coordinates in the bending plane. In addition, the top

and bottom covers of the MI and MO chambers are also drift chambers and measure the Z coordinate along the beam. There are a total of six Z chambers per octant.

The major sources of error in the sagitta measurement are the intrinsic resolution of the drift chambers, multiple scattering, and the accuracy of alignment of chambers belonging to different layers. The detector has been designed to minimize the contributions from each of these sources of errors. From a measurement with a test chamber, a single wire resolution of $200\text{ }\mu\text{m}$ was found. The contribution of the error due to the intrinsic resolution of the drift chambers is $57\text{ }\mu\text{m}$. The contribution due to multiple scattering is estimated to be about $31\text{ }\mu\text{m}$ at 45 GeV. Muons more energetic than 3 GeV are confined to one octant. Hence, the alignment of the chambers is critical between chambers in the same octant. This is accomplished with optical and mechanical measurements as well UV laser and cosmic ray verification [42]. An error contribution of $30\text{ }\mu\text{m}$ was found from this source.

2.9.1 The precision chambers

Each precision (P) chamber contains about 320 signal wires and a total of 3000 wires, including field shaping, cathode and guard wires. The signal and field shaping wires are positioned with a precision of about $10\text{ }\mu\text{m}$ in the bending direction and to better than $40\text{ }\mu\text{m}$ in the non-bending direction by precision pyrex glass and carbon fiber bridges. The chamber cells have been designed to have a very uniform field throughout the active region. An internal alignment system consisting of light emitting diodes, lenses and quadrant photodiodes is integrated with the structure of the bridges. These systems enable the positioning of the bridges and thereby the wire, to an accuracy of $10\text{ }\mu\text{m}$.

2.9.2 The Z-chambers

The Z-chambers consist of two layers of drift cells offset by one half cell with respect to each other to resolve left-right ambiguities. In total, there are 96 Z-chambers. If a muon passes through both MI and MO, its position in the $r - z$ plane is measured eight times. The measured resolution has been found to be $700\text{ }\mu\text{m}$.

2.10 The L3 Trigger

The goal of the L3 trigger system is to record detector signals from each beam crossing in which particles originate at the $Z \rightarrow e^+e^-$ vertex. This is achieved by a cascade of three digital trigger levels with intermediate buffering. Each of these three levels has redundant selection criteria which are logically OR'd to arrive at a decision. This ensures good efficiency for most physics channels. The settings and calibration of the accelerator, detector and trigger systems are monitored frequently and recorded to attain the highest precision in the event reconstruction. The functions of the three trigger levels are described in the following sections.

2.10.1 Level-1 trigger

The level-1 has five triggers based on the calorimeters, luminosity monitors, scintillation counters, muon chambers and the central tracking chamber, each gated with the beam crossing signal. A positive result from any of the five, commences the operation of the fine digitisation electronics, whereas on a negative result, all electronics is cleared and readied for the next beam crossing. The level-1 rate of positive decisions is less than 8 Hz, with less than 5% dead time incurred from the fine digitisations.

Calorimeter trigger

The level-1 calorimeter trigger is designed to select events which deposit energy in the electromagnetic or hadronic calorimeters. This includes e^+e^- , $\tau^+\tau^-$, hadronic and $\nu\bar{\nu}\gamma$ final states. The trigger requires at least 8 GeV in the BGO barrel or at least 15 GeV in the BGO and HCAL barrels or at 25 GeV in the entire calorimeter. The event is also accepted if a cluster in a $\theta - \phi$ block exceeds 6 GeV. If this cluster coincides with a track from the charged track trigger, the threshold is reduced to 2.5 GeV. Events with only a single isolated electromagnetic cluster of more than 1 GeV (single photon) are also accepted. The main source of background for this trigger is electronic noise and typical total rates are 1 to 2 Hz.

Scintillator trigger

Information from this trigger is used to select high multiplicity events and to reject cosmic rays. The mean time of a hit from any of the 30 scintillators is required to be within a loose gate of 30 ns for an event to be accepted. High multiplicity events are selected by requiring 5 hits spread by over 90° . The rate of this trigger is typically 0.1 Hz and it is practically background free.

Muon trigger

The muon trigger selects events with at least one particle which penetrates the muon chamber. To be selected, the event is required to have a track in the muon chambers with a transverse momentum larger than 1 GeV. The single muon trigger requires one track measured in at least two of the 3 P-chambers and 3 out of 4 Z-chambers in the same octant.

TEC trigger

The TEC trigger is used to select events with charged tracks. At least two tracks in the central tracking chamber with a transverse momentum larger than 150 MeV and separated by more than 120° in azimuth are required to accept an event. The trigger rate depends on the beam conditions, varying from 1 to 4 Hz.

Luminosity trigger

The luminosity trigger has the analog sums from the luminosity monitors as input. One of the following thresholds should be met to accept the event: two back-to-back (within ± 1 sector) depositions ≥ 15 GeV, total energy on one side greater than 25 GeV and greater than 5 GeV on the other, or a total energy on either side greater than 30 GeV. The trigger rate is 1.5 Hz typically; it depends primarily on the delivered luminosity, but it can also increase under bad background conditions.

2.10.2 Level-2 trigger

The function of the level-2 trigger is to reject background events selected by level-1. The inputs to the level-2 trigger are the coarse data used in level-1, the level-1 results and some more data available for analysis at this step. As compared to level-1, the level-2 trigger can spend more time per event without incurring additional deadtime and can also correlate subdetector signals improving the decisions made by level-1. Events that fulfill more than one level-1 trigger condition, are accepted by the level-2 trigger automatically. It mainly rejects calorimeter triggers generated by electronic noise and interactions with the rest gas in or the walls of the beam pipe. The rejection rate is typically 20-30% averaged over all level-1 triggers, such that the total rate after level-2 is typically less than 6 Hz.

2.10.3 Level-3 trigger

Level-3 applies criteria based on the complete digital data for the event, reducing the output rate to 2 to 3 Hz. Events which are selected by more than one trigger at level-1 are automatically accepted. Luminosity triggers are also passed through unhindered. Muon triggers are required to pass a more stringent scintillator coincidence in time (± 10 ns) and space ($\pm 60^\circ$). Tracks from TEC trigger events are correlated with at least 100 MeV of energy in the calorimeters; they are also examined for quality and a common vertex.

The output from the level-3 trigger is delivered into a memory buffer on the main online computer. From this buffer, all events are written to tape and selected events are dispatched to ten separate monitoring programs. Processes on a cluster of online computers control the data taking, monitoring, logging, detector adjustments and calibration of all the detector and trigger elements.

2.11 Event Reconstruction

To identify the physical content of the events recorded by the data acquisition system, the digitised output from the various subdetectors is reconstructed by the L3 reconstruction package REL3. The reconstruction process is accomplished in two steps. First the signals from each subdetector are analysed to create higher level objects which can be interpreted as signatures of particles which could have traversed the subdetector in question. This is done by software specific to each subdetector - TEL3, ECL3, HCL3, SCL3, MUL3, FLL3 and JTL3 for the TEC, ECAL, HCAL, scintillators, MUCH, luminosity monitors and the triggers. Next, information from the various subdetectors is combined to yield global information referring to particles in the event. This step is termed 'across L3' reconstruction and is performed by the package AXL3. For example, an electron or positron, like any charged particle, will leave a track in the TEC and then interact in the electromagnetic calorimeter. There will be no energy deposition in the hadronic calorimeter and no signal in the muon chambers. In the first stage of event reconstruction,

the track in the TEC and the electromagnetic bump in the BGO are reconstructed, independent of each other. In the second stage, a matching algorithm determines that the electromagnetic bump in the BGO was created by the same particle that left the track in the TEC and the two are grouped together as signatures of the same particle. The output from AXL3 aims to represent as close as possible particles and groups of particles. However, no physics assumptions are made by AXL3; these are left to the analysis groups.

The objects created by AXL3 relevant to this analysis are as follows:

- ASRC: smallest resolvable clusters made out of TEC tracks and calorimetric hits.
- AMU1: muons reconstructed across the L3 detector giving the best estimate of their momentum and direction at the vertex. The details of muon reconstruction have been described in [43].
- ASJT: jets using the ASRC's as fundamental building blocks. A geometrical algorithm is used to combine the ASRC's into jets [48]. These jets are used to determine the initial quark/gluon direction, invariant mass and momentum in the forthcoming analyses chapters.

2.12 Event Simulation

Simulating the detector response to the different types of physics interactions which are expected to be observed in a given detector is essential for various reasons. The simulated events aid the analysis by providing foresight into the characteristics of the events of the physics process being studied. The simulated events help in attaining a deeper understanding of the detector thereby reducing systematic errors. The geometrical and phase space acceptance of the process being studied is obtained from simulated events. Also, the reconstruction and analysis programs can be checked using the simulated events. This makes the both the precision tests and searches for rare new processes possible.

The Monte Carlo simulation is carried out in two steps:

Step 1: Event generation, where events are constructed according to a physics model.

The output of this step is the four momenta and the particle identification(ID) of the particles produced in the given event.

Step 2: Detector Simulation, where the generated particles are propagated through a detailed representation of the L3 detector. The tracking, shower simulation in the detector materials and the response of each active component of the detector is simulated. The output of this step is the digitised detector response, akin to the output from the data acquisition system, which is reconstructed using REL3 as well.

Various physics generators are used for event generation. In this analysis, the QCD generator Jetset [44] was primarily used. Table 2.1 lists the parameter settings affecting this analysis for the generated events.

<i>Parameter</i>	<i>Value</i>
m_Z	91.181 GeV
Γ_Z	2.501 GeV
$\sin^2\Theta_W$	0.2315
Λ_{QCD}	0.3 GeV
$\alpha_s(m_Z^2)$	0.125
ϵ_b	0.008
ϵ_c	0.07

Table 2.1: JETSET parameters.

The detector simulation is accomplished by the package, SIL3. It is based on the GEANT3 [45] package which enables the description of the detector geometry and a detailed simulation of all particle interactions including electromagnetic and hadronic showers. All processes, such as, decay, energy loss, multiple scattering, nuclear interaction, bremsstrahlung, pair production and photofission, are simulated when particles are tracked through the detector. SIL3 contains a complete representation of the L3 detector down to the required level of accuracy ($\sim 10 - 100\mu\text{m}$). Particles are tracked down to ~ 10 keV in the electromagnetic calorimeter and ~ 1 keV in the hadron calorimeter, which are the sensitivity limits of the two calorimeters. Hits in the TEC and HCAL are simulated using the time-to-distance relation measured in the test beam data.

Chapter 3

Event Selection and Acceptance Calculations

3.1 Introduction

In this analysis the J/ψ mesons were identified by their decay into a muon pair, $J/\psi \rightarrow \mu^+\mu^-$ (and alternatively ψ' mesons by $\psi' \rightarrow \mu^+\mu^-$). The inclusive muons used in this analysis were selected from a sample of 1.06 million $e^+e^- \rightarrow \text{hadrons}$ events, recorded in 1990, 1991 and 1992 with the L3 detector at $\sqrt{s} \approx m_Z$. The data sample corresponds to an integrated luminosity of 43.5 pb^{-1} . This chapter describes the selection criteria followed by a discussion of the efficiency and the sample purity.

3.2 Hadron selection

Hadronic events are characterised by an average energy deposition in the detector of approximately the center of mass energy, a low energy imbalance and a high particle multiplicity. These properties are used in triggering and selecting these events. A brief outline of hadron event selection follows; details have been described elsewhere [54].

3.2.1 Triggers

The primary triggers used in the hadronic event selection are the energy, scintillation counter and charged track triggers. Events with muons are also triggered by the single muon trigger. Since three independent triggers are utilised, the individual trigger efficiencies can be determined from a study of the trigger data of the selected hadronic events. This analysis shows that the calorimetric trigger is $(99.684 \pm 0.003)\%$ efficient, and the scintillation counter and charged track triggers are each $(93.73 \pm 0.02\%)$ and $(96.15 \pm 0.02\%)$ efficient, respectively [47]. The combined trigger efficiency for hadronic events fulfilling the selection criteria is $(99.988 \pm 0.001\%)$. Hence, the systematic error due to trigger inefficiencies is negligible.

3.2.2 Event Selection and Acceptance

The event selection for the process $e^+e^- \rightarrow \text{hadrons}$ is based on the energy depositions in the electromagnetic and hadronic calorimeters, and the momentum of muons measured in the muon chambers. A clustering algorithm is used to group energy depositions in the calorimeters [48]. Since the minimum energy needed to form a cluster in the endcaps is slightly larger than in the barrel region, the two regions are treated differently. On the average, the clustering algorithm reconstructs one cluster per particle and a typical hadronic event contains forty such clusters. The background processes for this channel are $Z \rightarrow \tau^+\tau^-(\gamma)$, two photon processes, beam gas interactions and cosmic rays.

The event selection criteria are as follows:

1. $0.5 < E_{vis}/\sqrt{s} < 1.5$, where E_{vis} is the total energy observed in the detector. Figure 3.1 shows the distribution of the total observed energy in the detector, E_{vis} , normalised to \sqrt{s} for the data compared to simulated events.
2. The longitudinal and transverse energy imbalances are obtained by constructing the vectorial sum of all the cluster momenta $E_i \hat{p}_i$ (neglecting the particle masses):

$$\vec{E} = \sum_i E_i \hat{p}_i \quad (3.1)$$

The imbalances are then defined as

$$E_{||} = |E_z|/E_{SRC}, \quad E_T = \sqrt{E_x^2 + E_y^2}/E_{SRC}, \quad (3.2)$$

where E_{SRC} is the simple energy sum of all calorimetric clusters. Then,

- a. $|E_{||}/E_{vis}| < 0.5$
- b. $|E_{\perp}/E_{vis}| < 0.5$

The distributions for the longitudinal and transverse energy imbalances for data compared to the Monte Carlo events are shown in Figures 3.2 and 3.3, respectively.

3. The number of clusters, $N_{cluster}$, reconstructed in the calorimeters is required to satisfy:
 - a. $N_{cluster} \geq 13$ for $|\cos \theta_t| < 0.74$ (Barrel) or
 - b. $N_{cluster} \geq 9$ for $|\cos \theta_t| > 0.74$ (End-cap) where θ_t is the polar angle of the event thrust axis¹ with respect to the beam line.

Figure 3.4 shows the distribution for the number of calorimetric clusters in the barrel region for data and five flavor Monte Carlo. The discrepancy between data and Monte Carlo at the high end of the distribution is partially understood to be due to an incorrect hadronic cross section used in the simulation of the interactions of charged pions with the detector material.

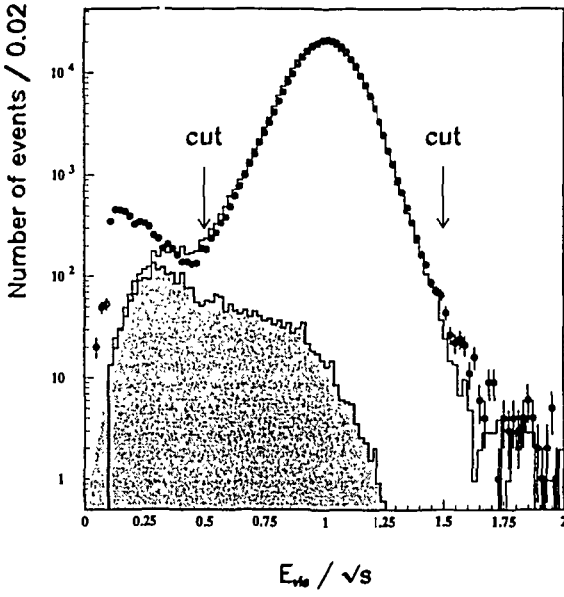


Figure 3.1: Scaled visible energy distribution for data compared with the Monte Carlo prediction. The shaded area represents the contribution expected from the background processes, $e^+e^- \rightarrow \tau^+\tau^-$ and $e^+e^- \rightarrow e^+e^-(\gamma)$.

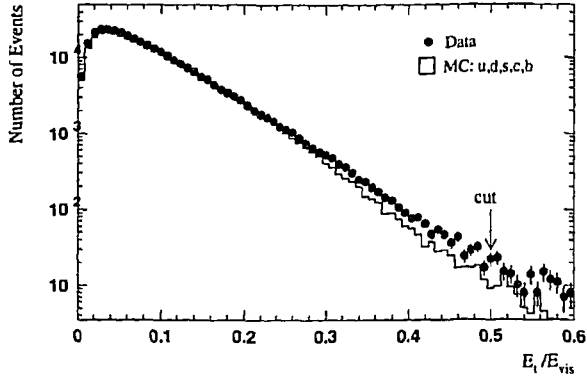


Figure 3.2: Longitudinal energy imbalance for data compared with the Monte Carlo prediction.

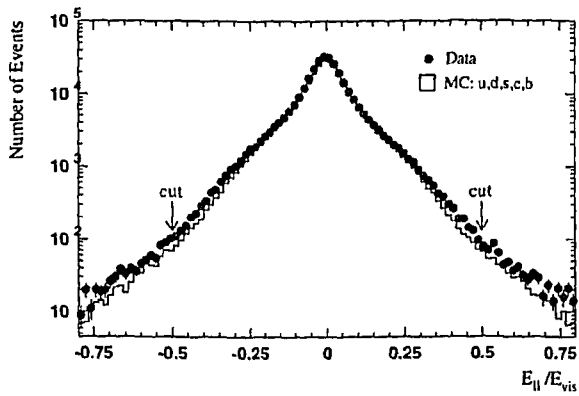


Figure 3.3: Transverse energy imbalance for data compared with the Monte Carlo prediction.

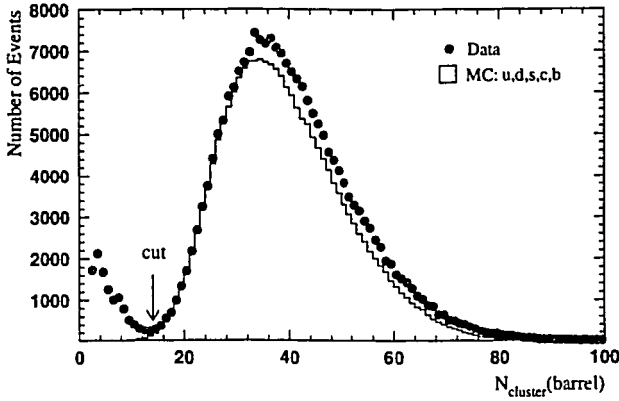


Figure 3.4: The number of calorimetric clusters in the barrel region for data compared to the Monte Carlo prediction.

Since the hadron calorimeter covers 99.5% of the full solid angle, the acceptance for $e^+e^- \rightarrow \text{hadrons}$ events is very high, $(99.15 \pm 0.03)\%$, including all detector inefficiencies. This number has been determined with the JETSET 7.3 [44] Monte Carlo program and cross checked with HERWIG 5.3 [49]. The results from the two models are consistent.

3.3 Event Preselection

Since the branching ratio for the process considered is small ($\sim 10^{-3}$), first the hadronic data and Monte Carlo was analysed with very loose cuts. The events that meet the selection criteria were written onto a tape. All events with at least two AMUI's (Section 2.11) coming from the interaction region and lying in the same hemisphere were selected. The invariant mass of the muon pair was further required to be at least 1.8 GeV. The preselection pass reduced the event sample from 1.06 million to approximately 600 events.

3.4 Muon selection

Muons are identified and measured in the muon chamber system, which covers the angular range $|\cos \theta_\mu| < 0.75$. Figure 3.5 shows the JETSET 7.3 Monte Carlo momentum

¹The thrust axis \mathbf{n} is defined in such a way that the longitudinal momenta p_{iL} with respect to this axis are maximal, $T = \max \sum_i \frac{|p_{iL}|}{|p_i|}$.

spectrum of the two J/ψ daughter muons - the faster of the two on the left and the slower on the right. The unshaded histogram in both plots is the generated momentum and the hatched histogram is the momentum spectrum of the reconstructed muons. It can be seen from the plot that in the laboratory frame, the J/ψ tends to decay asymmetrically - one of the daughter muons carries off most of the momentum. In order to reconstruct the J/ψ mesons, the cut on the muon momentum should be as low as possible. However, as is obvious from the plots, muons less energetic than 2 GeV do not get reconstructed. They range out in the calorimeters and are not seen in the muon chamber system. Hence, to maximize the efficiency, no cut was applied on the muon momentum.

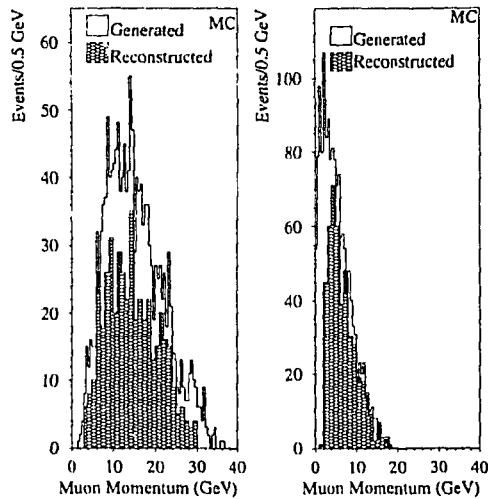


Figure 3.5: Muon momentum spectrum from JETSET 7.3. The momentum of the more energetic of the two J/ψ daughter muons is on the left and the lower muon momentum spectrum is on the right.

The background in the muon selection consists mainly of punchthrough hadrons, i.e., pions, protons and kaons, which do not interact in the calorimeter and muons which are not products of J/ψ decays. Thus, more stringent cuts were applied on the preselected sample to reject the background and to select well measured muons.

The cuts used to identify muons for this analysis and their motivation are as follows:

- **P segment cut:** The track has at least two (out of three) segments in the muon P chambers to guarantee a sufficiently good momentum resolution.
- **Z segment cut:** The track has at least one (out of two) segments in the muon Z chambers to ensure optimal angular resolution.
- **Vertex Cut:** The track was required to point to the interaction region to reject punchthrough hadrons and muons that do not originate at the interaction vertex:
 - In the transverse plane the distance from the interaction vertex was required to be less than 4 times the error on the track position.
 - In the longitudinal plane the interaction vertex was required to be less than 5 times the error on the track position away from the nominal collision point.

Figure 3.6 shows the distributions of the distance from the interaction vertex in the transverse and longitudinal planes divided by their respective errors for the preselected data and Monte Carlo samples.

3.5 J/ψ Selection

After a pair of muons is found, in which each muon satisfies the cuts outlined above, J/ψ candidates are selected by applying the following cuts:

1. The muons are required to be oppositely charged.
2. The opening angle between the muons is required to be less than 90° . This kinematic requirement reduces the background significantly at large invariant masses without reducing the J/ψ finding efficiency. Figure 3.7 shows the distribution of the opening angle between the two J/ψ daughter muons from the 'pure' JETSET Monte Carlo events. As can be seen from the figure, the opening angle between the two muons is never greater than 90° . This also holds for the gluon and charm fragmentation produced J/ψ 's.

Figure 3.8 shows one of the selected events recorded by the L3 detector.

3.6 Background Simulation and Acceptance Calculation

Muon pairs that pass the above cuts can also arise from one of the following background sources:

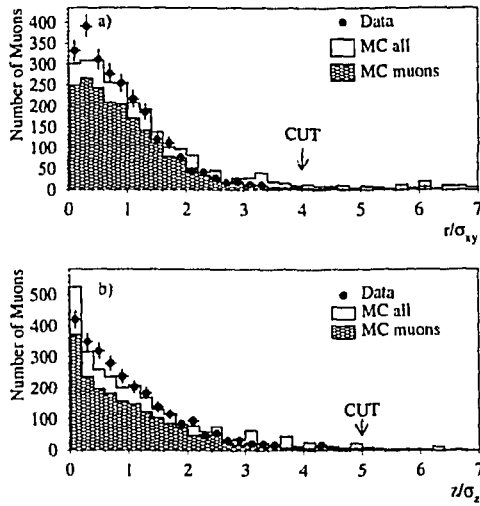


Figure 3.6: Distance from the interaction vertex for the preselected muons a) in the transverse plane and b) in the longitudinal plane divided by the errors on them respectively for the preselected data and the Monte Carlo samples.

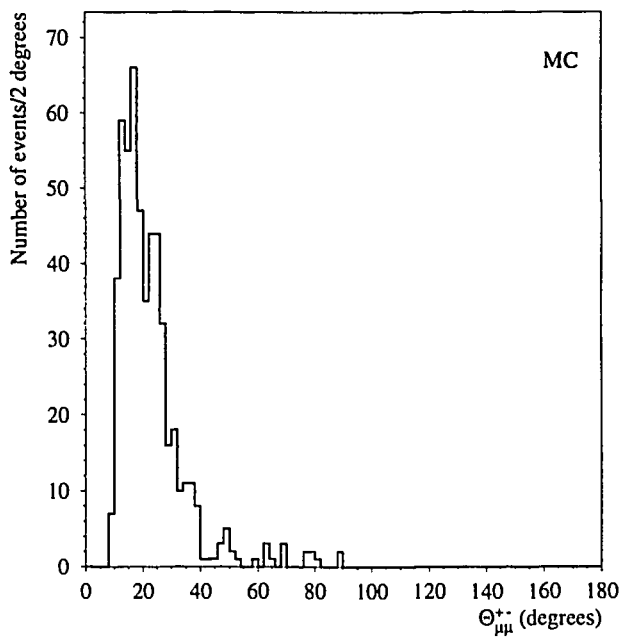


Figure 3.7: The Monte Carlo prediction for the opening angle between the two J/ψ daughter muons from JETSET 7.3.

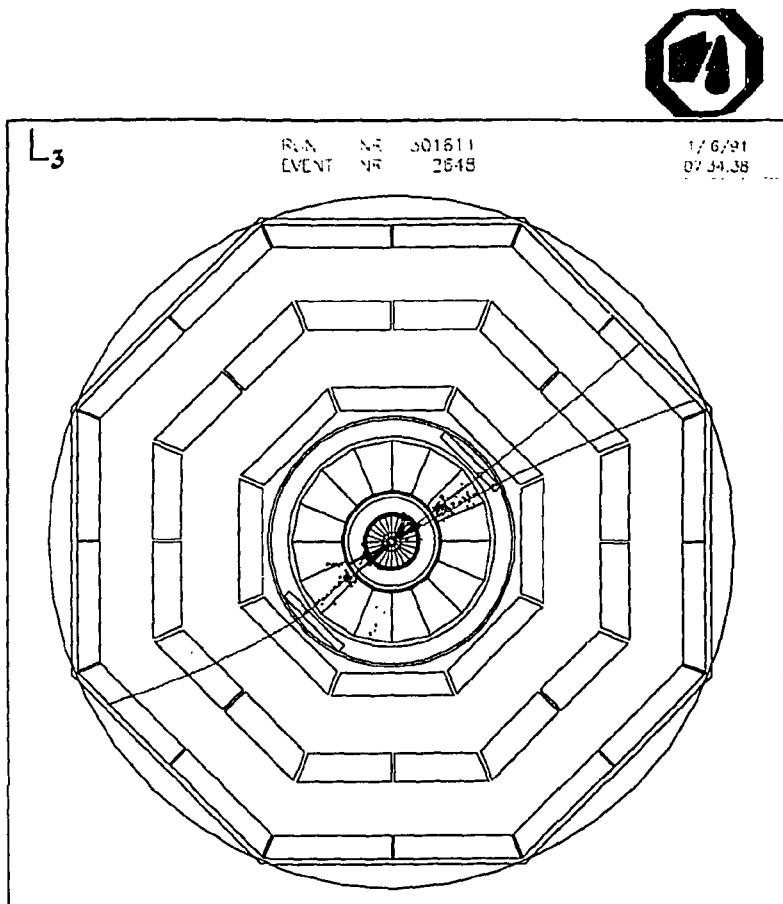


Figure 3.8: A $J/\psi \rightarrow \mu^+\mu^-$ candidate event recorded by the L3 detector.

1. The semileptonic decay of a b hadron to a c hadron ($b \rightarrow c\mu^-\bar{\nu}X$), followed by the semileptonic decay of the c hadron ($c \rightarrow s\mu^+\nu X$) (cascade decays) and the charge conjugate cascade decays.
2. A prompt muon from a b or c hadron decay, with a misidentified hadron or a muon from a K or π decay.
3. A misidentified hadron with a muon from a K or π decay.
4. Two misidentified hadrons.

To simulate the background processes, 2 million five flavor $Z \rightarrow q\bar{q}(g)$ Monte Carlo events produced with the JETSET model [44] were used. These events were subjected to the same preselection as the data, thus reducing the event sample. Table 3.1 shows the fraction of each source of muon pairs in the invariant mass region of 2.8 and 3.4 GeV. As can be seen from the table, the dominant background source is cascade decays.

Source	Fraction
$J/\psi \rightarrow \mu^+\mu^-$	60.59 %
Cascade	30.54 %
Muon + misidentified hadron	7.39 %
Hadron pair	1.48 %

Table 3.1: Monte Carlo estimates of the sample of event samples in the muon pair invariant mass region of 2.8 to 3.4 GeV.

Figure 3.9 shows the JETSET 7.3 five flavor Monte Carlo fitted muon pair invariant mass distribution between 2.0 and 4.0 GeV. A binned maximum likelihood fit was performed on the distribution. An exponential was found suitable to describe the shape of the background whereas the signal was fitted with a Gaussian. The mean and the width of the Gaussian and the background shape were left free in the fit. From the fit, the J/ψ mass and width were found to be 3.093 ± 0.014 GeV and 134 ± 16 MeV, respectively.

Since the process considered has a small branching ratio, a 'pure' Monte Carlo event sample, in which every b hadron decays into a J/ψ and every J/ψ decays into a muon pair, was used to compute the acceptance. Also, no single Monte Carlo model contains all J/ψ production mechanisms studied in this thesis. Hence, different models had to be employed to determine the acceptance for the various production mechanisms. In all cases, the J/ψ was forced to decay into a muon pair. The acceptance for J/ψ mesons produced via the decay of b hadrons was determined with JETSET 7.3. The events were b -flavour with the decay chain being forced to be $b \rightarrow J/\psi + X$; $J/\psi \rightarrow \mu^+\mu^-$ for one of the b -hadrons. For systematic studies, similar events were simulated with JETSET 7.3 interfaced with EURODEC for the decay of the b hadron. To study the gluonic production of J/ψ , events produced by CORFUJ [50] were used. To study the J/ψ mesons produced

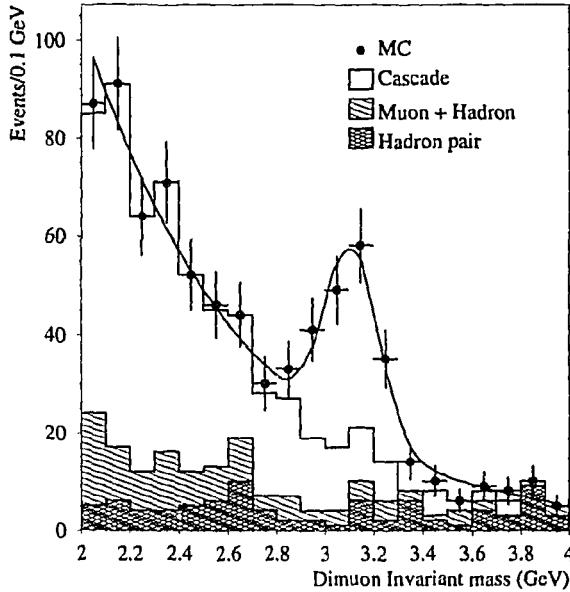


Figure 3.9: JETSET 7.3 five flavor Monte Carlo $\mu^+\mu^-$ invariant mass distribution. The curve is the result of the fit described in the text. The contributions from the various background sources are shown by the histogram.

via charm fragmentation, $Z \rightarrow c\bar{c}g(g)$ events with a J/ψ decaying into a muon pair were simulated [51]. Table 3.2 lists the different kinds of Monte Carlo events simulated for the acceptance calculation.

The acceptance for the $J/\psi \rightarrow \mu^+\mu^-$ is mainly determined by the angular coverage of the muon chambers ($\sim 75\%$) and the absorption of low momentum muons in the calorimeter. From the Monte Carlo it was determined that approximately 20% of the $b \rightarrow J/\psi$ events were lost because the momentum of either one or both the muons was less than 2.0 GeV. For gluonic production, the number of events lost is even higher because the muon momentum spectrum is softer; 40% of the $Z^0 \rightarrow q\bar{q}g^*$; $g^* \rightarrow J/\psi + X$; $J/\psi \rightarrow \mu^+\mu^-$ events have at least one muon with momentum less than 2 GeV.

Figure 3.10 shows the $\mu^+\mu^-$ invariant mass distribution for the ‘pure’ JETSET 7.3 sample. The distribution is fitted with a gaussian giving a mass of 3.111 ± 0.005 GeV and a

<i>Monte Carlo model</i>	<i>Number of events</i>
JETSET 7.3	1500
JETSET 7.3+EURODEC	3000
JETSET 7.3 (charm fragmentation)	1000
CORFUJ	1200

Table 3.2: The different Monte Carlo models and the number of each type of events simulated to determine the acceptance for various J/ψ production mechanisms studied in this thesis.

width of 139 ± 5 MeV. The number of events accepted is determined from this fit. Table 3.3 lists the efficiency computed for the four Monte Carlo sets. The efficiencies obtained from the JETSET 7.3 and JETSET 7.3 interfaced with EURODEC are consistent. The efficiency for gluonic production is lower for reasons explained above.

Since, the JETSET 7.3 as used in L3 agrees with the data better than EURODEC, it was utilised for further analyses.

<i>Monte Carlo model</i>	<i>Efficiency</i>
JETSET 7.3	$30.15 \pm 0.01\%$
JETSET 7.3+EURODEC	$30.45 \pm 0.01\%$
JETSET 7.3 (charm fragmentation)	$27.9 \pm 0.01\%$
CORFUJ	$24.33 \pm 0.01\%$

Table 3.3: Estimates for the J/ψ finding efficiency for the different Monte Carlo models and the statistical error.

3.6.1 Detector Inefficiency

The detector simulation takes into account detector inefficiencies which are constant over a running period. For example, noisy BGO crystals are killed during reconstruction, hits in a TEC sector which was not functional are ignored and track segments in dead cells in the MUCH are not considered. If a substantial part of the detector being used in a particular analysis is off or noisy during a certain run, the run is classified as a 'bad' run and rejected. However, if only a small segment of the detector was malfunctioning at a certain given time, it would be wasteful to reject the events. These non-constant inefficiencies are not taken into account in the simulation process. They do affect the analysis, though; Monte Carlo may predict not only better resolution but higher tagging efficiencies as well. These inefficiencies can be determined from data and corrected for.

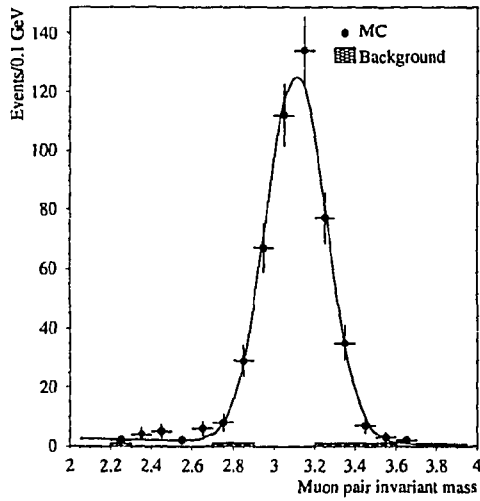


Figure 3.10: JETSET 7.3 'pure' Monte Carlo $\mu^+\mu^-$ invariant mass distribution. The curve is the result of the fit described in the text.

This analysis uses the muon chambers and hence, we are concerned with the discrepancy between the data and Monte Carlo for the muon chambers. Several methods were used to determine the muon chamber inefficiency for the different running periods. From the hadronic sample, a global inefficiency was inferred by comparing the number of muons with P segments (1 to 3) and Z segments (1 or 2) in data and Monte Carlo [43]. In another method, the muons from $\tau \rightarrow \mu X$ in a sample of $e^+e^- \rightarrow \tau^+\tau^-$ events were identified with the inner detectors, i.e., the tracking chamber and the electromagnetic and hadronic calorimeters. The fraction of these events in which a corresponding track was found in the muon chambers was determined, thereby giving the muon chamber efficiency [52] ϵ_μ .

However, in the present analysis each event has two muons, with an average azimuthal opening angle of 15° as can be inferred from Figure 3.11. If both muons go into the same dead cell, the efficiency to observe a muon pair, $\epsilon_{\mu^+\mu^-} = \epsilon_\mu$ as opposed to $\epsilon_{\mu^+\mu^-} = \epsilon_\mu^2$, if they go into different dead cells. Hence, in this analysis a different method which takes these correlations into account was used to determine the J/ψ finding efficiency. The method has been described in detail elsewhere [53] and here only a brief outline is presented.

This method exploits the clear signal provided by the $Z \rightarrow \mu^+\mu^-$ events and the characteristic of the channel that the two energetic muons are back to back on the average. In order to reject the background that can contaminate the sample, the $Z \rightarrow \mu^+\mu^-$ events are accepted only if:

- The number of reconstructed muons is 1 or 2.
- At least one muon has $40 \leq p_\mu \leq 45$ GeV, where p_μ is the muon momentum.
- If there are two muons with $\cos \Theta_{\mu\mu} < 0$, where $\Theta_{\mu\mu}$ is the opening angle between them.

Since, each TEC half sector covers 7.5° in ϕ , the entire (θ, ϕ) space is divided into cells of $7.5^\circ, 7.5^\circ$. An efficiency for each (θ, ϕ) cell is determined by counting the number of times that only a single muon is found in an event. If only one muon is found in the event, the cell where the other muon was expected to be found, i.e., $(\theta + \pi, \phi + \pi)$, is inefficient. Applying the same algorithm to simulated and real data, a cell by cell correction factor is evaluated for the Monte Carlo which is simply the ratio between the data efficiency and the Monte Carlo efficiency for the given cell. In the Monte Carlo, it is possible to compare the evaluated efficiency with the actual efficiency, i.e., number of reconstructed muons/number of generated muons. This comparison gives the systematic error on the method which was determined to be 10%.

The validity of the method for muons with lower momentum was checked using the $\tau \rightarrow \mu X$ sample. Within the statistical error, the efficiency so determined was found to be independent of the muon momentum.

The J/ψ finding efficiency was redetermined applying the weights cell by cell. Table 3.4 lists the results for the different running periods and the different Monte Carlo samples. The results from this method are consistent with those obtained from other methods [43, 52].

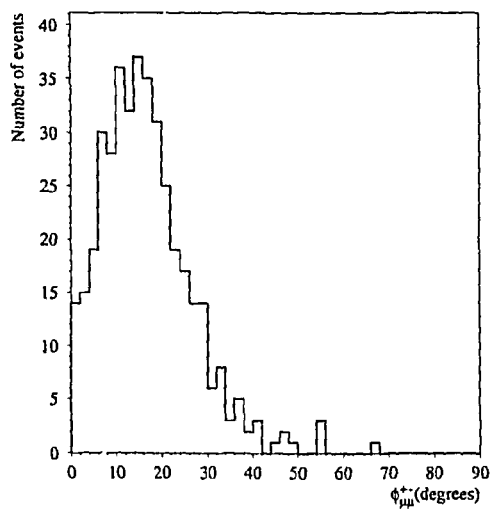


Figure 3.11: The Monte Carlo prediction for the azimuthal opening angle between the two J/ψ daughter muons from JETSET 7.3.

<i>Monte Carlo Model</i>	<i>Running Period</i>	Corrected $\epsilon_{J/\psi}$ (%)
JETSET 7.3	1991	26.9 ± 0.01
	1992	26.4 ± 0.01
JETSET 7.3+EURODEC	1991	27.2 ± 0.01
	1992	26.6 ± 0.01
JETSET 7.3 (charm fragmentation)	1991	24.6 ± 0.01
	1992	24.1 ± 0.01
CORFUJ	1991	21.0 ± 0.01
	1992	20.5 ± 0.01

Table 3.4: The muon chamber inefficiency corrected J/ψ efficiency and statistical error for various running periods and different Monte Carlo models.

Chapter 4

J/ψ and ψ' Production

4.1 Introduction

In this chapter the determination of the $Br(Z^0 \rightarrow J/\psi + X)$ and $Br(Z^0 \rightarrow \psi' + X)$ is described. As discussed in Chapter 1, the major process contributing to J/ψ production at LEP energies is expected to be the decay of b hadrons. In addition, a small fraction of J/ψ mesons is expected to be produced via charm and gluon fragmentation. From the invariant mass of the jet containing the J/ψ and from the J/ψ decay length, limits are set on the charm fragmentation and gluon production of J/ψ mesons. Furthermore, this limit is used to calculate the fraction of the J/ψ mesons from b hadron decays, $Br(b \rightarrow J/\psi + X)$.

4.2 Determination of J/ψ and ψ' Production

The measured invariant mass distribution of $\mu^+\mu^-$ pairs in the mass region $2.0 < m_{\mu^+\mu^-} < 5.0$ GeV is shown in Figure 4.1. It is fitted with a gaussian for the J/ψ and ψ' signals and an exponential for the background using an unbinned maximum likelihood fit. The probability density function used for the fit is given by

$$\mathcal{P}_i = f_{J/\psi} \times \mathcal{G}_1 + f_{\psi'} \times \mathcal{G}_2 + (1 - f_{J/\psi} - f_{\psi'}) \times E \quad (4.1)$$

where $f_{J/\psi}$ is the fraction of J/ψ events and $f_{\psi'}$ is the fraction of ψ' events. \mathcal{G}_1 and \mathcal{G}_2 are Gaussians which describe the signal; they are defined as follows

$$\mathcal{G}_1 = 1/\sqrt{2\pi}\sigma e^{-(m_i - m_{J/\psi})^2/2\sigma^2} \quad (4.2)$$

$$\mathcal{G}_2 = 1/\sqrt{2\pi}\sigma e^{-(m_i - m_{\psi'})^2/2\sigma^2}, \quad (4.3)$$

where m_i is the measured invariant mass for the i_{th} event, σ is the sigma of the two gaussians, $m_{J/\psi}$ is the J/ψ mass, $m_{\psi'}$ is the ψ' mass. The background shape is described by an exponential, E which is given by:

$$E = \frac{b}{e^{-5b} - e^{-2b}} e^{-bm_i}, \quad (4.4)$$

where b is the slope of the exponential. The fit is performed in the region from 2.5 GeV and the denominator in the above equation is the normalisation factor. The fit function to be maximized is

$$\mathcal{L} = \sum_i \ln P_i \quad (4.5)$$

Since the statistics is poor, the width of the two gaussians was fixed to the Monte Carlo value of 140 MeV; the same mass resolution is assumed for J/ψ and ψ' . The J/ψ mass was fixed to 3.097 GeV [3] and the ψ' mass was fixed to 3.686 GeV [3]. All other parameters were left free in the fit. From the fit, $f_{J/\psi}$ is found to be 0.246 ± 0.030 giving 98.5 ± 12.0 J/ψ 's. $f_{\psi'}$ is found to be 0.012 ± 0.013 giving 5 ± 5 ψ' 's. The number of background events in the invariant mass window of $2.8 < m_{\mu^+\mu^-} < 3.4$ GeV is 40 ± 5 .

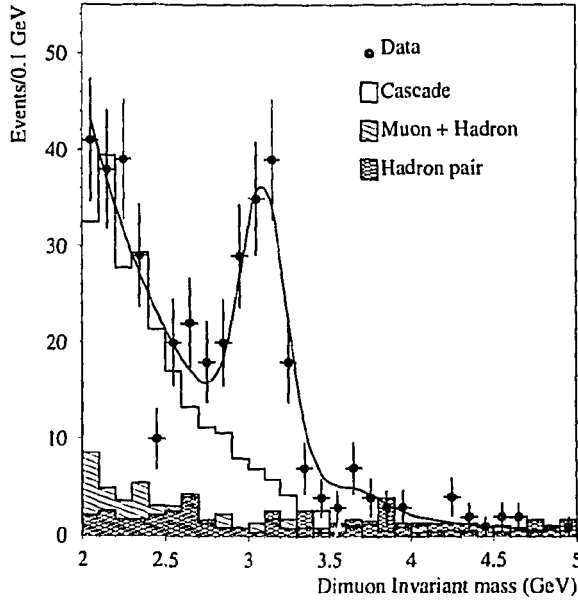


Figure 4.1: The $\mu^+\mu^-$ invariant mass distribution between 2.0 and 5.0 GeV. The solid line is the result of the fit described in the text. The contributions from the various background sources as estimated from Monte Carlo are shown by the histograms.

4.3 Determination of $Br(Z^0 \rightarrow J/\psi + X)$

The branching ratio $Br(Z^0 \rightarrow J/\psi + X)$ can be calculated as follows:

$$Br(Z^0 \rightarrow J/\psi + X) = \frac{N_{J/\psi}}{\varepsilon_{J/\psi}} \cdot \frac{\varepsilon_h}{N_h} \cdot \frac{\Gamma_h}{\Gamma_z} \cdot \frac{1}{Br(J/\psi \rightarrow \ell^+ \ell^-)} \quad (4.6)$$

where $N_{J/\psi}$ and N_h are the number of the J/ψ meson signal events and the total number of hadronic Z^0 decays, respectively, and ε_h is the selection efficiency for hadronic events [54]. $\varepsilon_{J/\psi}$ denotes the geometric and kinematic acceptance corrected for the detector inefficiencies as determined from Jetset 7.3 Monte Carlo and described in section 3.6.1, for the J/ψ mesons; Γ_h and Γ_z are taken from the L3 measurements [54]. Using the measurement of $Br(J/\psi \rightarrow \ell^+ \ell^-) = 0.0590 \pm 0.0015$ from the MARK-III experiment [56], we determine:

$$Br(Z^0 \rightarrow J/\psi + X) = (4.0 \pm 0.6 (stat.)) \times 10^{-3}$$

4.3.1 Systematic Error

The systematic error is computed by varying all known quantities that could contribute to it by their measured or estimated error. There are four major sources of systematic error in the measurement of the branching ratio $Br(Z^0 \rightarrow J/\psi + X)$.

- **Fitting Procedure.** Since the number of signal events is obtained from a fit, changes in the fitting procedure change $N_{J/\psi}$. To obtain the systematic error due to the fitting procedure, the signal and the background shapes were varied. The width of the gaussian was varied by the error on it from the fit to the ‘pure’ Monte Carlo, i.e., 15 MeV and the background shape was fitted by a three degree polynomial. Also, the fit was performed excluding the ψ' . The fit to the $\mu^+ \mu^-$ pair invariant mass distribution to extract the number of signal events contributes 0.2×10^{-3} .
- **J/ψ Selection.** The efficiency for finding J/ψ mesons is a function of the selection cuts. To find the contribution of the selection procedure to the systematic error, the analysis was redone with the following cuts:
 - $4.0 < p_\mu < 45$ GeV, where p_μ is the muon momentum.
 - In the transverse plane the interaction vertex was required to be less than 3 times the error on it and in the longitudinal plane it was required to be less than 4 times the error on it.

The systematic error arising from this source was estimated to be 0.2×10^{-3} .

- **Dimuon Detection Efficiency.** The dimuon detection efficiency determination, as described in Section 3.6.1, contributes an additional 0.1×10^{-3} to the systematic error.

- $Br(J/\psi \rightarrow \ell^+ \ell^-)$. This number used from MARK III contributes 0.2×10^{-3} to the systematic error.

Table 4.1 lists the various contributions to the systematic error on the measurement of the branching ratio $Br(Z^0 \rightarrow J/\psi + X)$. The total systematic error is obtained by adding the four contributions in quadrature, giving 0.4×10^{-3} .

Contribution	$\Delta Br(Z^0 \rightarrow J/\psi + X) \times 10^{-3}$
Fitting procedure	0.2
J/ψ selection	0.2
Dimuon detection efficiencies	0.1
$Br(J/\psi \rightarrow \ell^+ \ell^-)$	0.2

Table 4.1: Contributions to the systematic error on the $Br(Z^0 \rightarrow J/\psi + X)$ measurement, obtained by changing the method or varying the parameters by their errors, as described in the text.

4.3.2 Final Result

The final result is:

$$Br(Z^0 \rightarrow J/\psi + X) = (4.0 \pm 0.6(stat.) \pm 0.4(sys.)) \times 10^{-3}$$

This is in good agreement with previous measurements made by L3 [57] and other LEP experiments [58]. Table 4.2 summarizes the previous LEP measurements.

Experiment	$Br(Z^0 \rightarrow J/\psi + X)$
OPAL (90-91)	$(4.5 \pm 0.8 \pm 0.6) \times 10^{-3}$
ALEPH (90-91)	$(3.81 \pm 0.41 \pm 0.26) \times 10^{-3}$
L3 (90-91)	$(4.1 \pm 0.7 \pm 0.3) \times 10^{-3}$
This analysis (90-92)	$(4.0 \pm 0.6 \pm 0.4) \times 10^{-3}$

Table 4.2: The experimental results for inclusive J/ψ production in Z decays[56,57].

4.4 Determination of $Br(Z^0 \rightarrow \psi' + X)$

The branching ratio of $Br(Z^0 \rightarrow \psi' + X)$ can be calculated as follows:

$$\text{Br}(Z^0 \rightarrow \psi' + X) = \frac{N_{\psi'}}{\epsilon_{\psi'}} \cdot \frac{\epsilon_h}{N_h} \cdot \frac{\Gamma_h}{\Gamma_z} \cdot \frac{1}{\text{Br}(\psi' \rightarrow \ell^+ \ell^-)} \quad (4.7)$$

where $N_{\psi'}$ and N_h are the number of the J/ψ meson signal events and the total number of hadronic Z^0 decays, respectively, and ϵ_h is the selection efficiency for hadronic events [54]; $\epsilon_{\psi'}$ denotes the geometric and kinematic acceptance for the process corrected for the detector inefficiencies. Since, the mass difference between the J/ψ and ψ' is small (~ 0.589 GeV), the same efficiency as the one for the J/ψ as determined from Jetset 7.3 Monte Carlo and described in section 3.6.1 can be used in this computation. Γ_h and Γ_z are taken from the L3 measurements [54]. Using the measurement of $\text{Br}(\psi' \rightarrow \ell^+ \ell^-) = 0.0077 \pm 0.0017$ [3] we determine at 90% confidence level:

$$\text{Br}(Z^0 \rightarrow \psi' + X) < 2.0 \times 10^{-3}$$

This result is consistent with the theoretical prediction in Section 1.7.

4.5 Non-b J/ψ Production

In this analysis, an invariant mass window of $2.8 < m_{\mu^+ \mu^-} < 3.4$ is used to identify J/ψ mesons. In order to distinguish the J/ψ mesons produced via charm fragmentation and gluon jets from those coming from b hadron decays, the following distributions are used:

- **Jet Invariant Mass:** The invariant mass of the jet the J/ψ belongs to, separates the gluon produced J/ψ from the b produced ones. Here, the jet used is the ASJT as described in Section 2.11. For the J/ψ mesons coming from b hadron decays, the invariant mass of the jet containing the J/ψ is of the order of the b quark mass whereas when the parent of the J/ψ is an excited gluon, the invariant mass of the jet is lower. This distribution has no separating power between the charm fragmentation and the b decay cases because the b quark jet mass is very close to the c quark jet mass. The quark jet mass may not be equal to the quark mass mainly due to contamination from fragmentation products from the primary vertex. Figure 4.2 shows the jet mass distribution for the three cases. The b hadron and charm fragmentation distributions have been obtained using JETSET whereas CORFUJ has been used in the gluon case.
- **Decay Length:** This distribution is used to distinguish the J/ψ mesons which are products of b hadron decays from the charm fragmentation and gluon produced ones. The decay length measurement is described in detail in the following chapter. In the charm fragmentation and gluon bremsstrahlung cases, the J/ψ mesons are prompt and originate at the primary vertex. The measured decay length is then just the TEC resolution and the beam spot size. Figure 4.3 shows the decay length distributions in the three cases. The b hadron and charm fragmentation distributions have been obtained using JETSET whereas CORFUJ has been used in the gluon case.

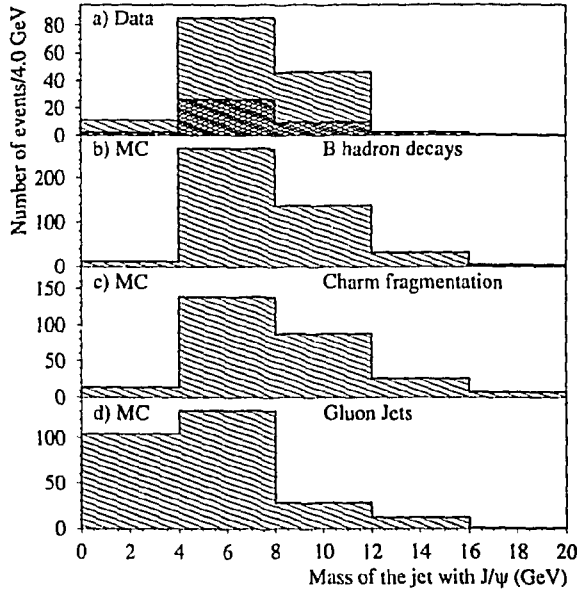


Figure 4.2: The invariant mass of the jet the J/ψ meson belongs to for the three production mechanisms a) data with where the shaded histogram is the estimated background contribution from five flavor Monte Carlo, b) b hadron decay, c) charm fragmentation, and d) gluon bremsstrahlung. Distributions b) and c) have been obtained from JETSET and d) from CORFUJ.

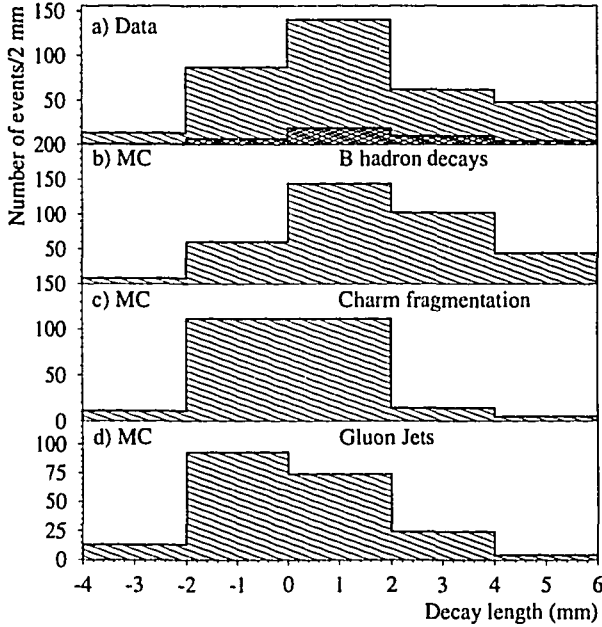


Figure 4.3: The decay length of the two daughter muons of the J/ψ meson for the three production mechanisms a) data with the shaded histogram showing the background contribution obtained using five flavor Monte Carlo, b) b hadron decay, c) charm fragmentation, and d) gluon bremsstrahlung. Distributions b) and c) have been obtained from JETSET and d) from CORFUJ.

A limit on the production rate of the charm fragmentation and gluon production of J/ψ mesons is set by performing a maximum likelihood fit to the two dimensional distribution of the decay length versus the jet invariant mass over their entire range. In the fit, the fractions of J/ψ produced through b hadron decay, charm fragmentation and gluon jets are varied. The background is obtained from the five-flavor Monte Carlo events generated using JETSET.

From the fit, the fraction of J/ψ mesons coming from gluon jets is estimated to be:

$$f_g = -0.07 \pm 0.10(stat.) \pm 0.01(sys.) \quad (4.8)$$

and, the fraction of J/ψ produced via charm fragmentation is:

$$f_c = -0.08 \pm 0.19(stat.) \pm 0.01(sys.). \quad (4.9)$$

The systematic errors come from the uncertainty in the background contribution which was varied by $\pm 5\%$.

Constraining $0 \leq f_g \leq 1$ and $0 \leq f_c \leq 1$ and using the acceptances for the charm and gluon production mechanisms corrected for detector inefficiencies as described in section 3.6.1, limits are set on the two branching ratios:

$$Br(Z \rightarrow q\bar{q}g^*; g^* \rightarrow J/\psi + X) < 0.6 \times 10^{-3},$$

$$Br(Z \rightarrow c\bar{c}g^*; c(\bar{c}) \rightarrow J/\psi + X) < 1.1 \times 10^{-3},$$

at 90% C.L. This result is consistent with [57] where the gluon jet production of J/ψ mesons was investigated.

4.6 Determination of $Br(b \rightarrow J/\psi + X)$

Since, the J/ψ production via charm fragmentation and gluons is consistent with zero, we can assume that all the J/ψ are products of b hadron decays and the branching ratio $Br(b \rightarrow J/\psi + X)$ can be deduced using the following relationship:

$$Br(b \rightarrow J/\psi + X) = \frac{\Gamma_z}{2 \cdot \Gamma_{bb}} \cdot Br(Z^0 \rightarrow J/\psi + X). \quad (4.10)$$

Using the value of Γ_z [54] and Γ_{bb} [59] from L3 measurements, we find

$$Br(b \rightarrow J/\psi + X) = (1.25 \pm 0.16(stat.) \pm 0.14(sys)) \times 10^{-2}.$$

4.7 Discussion and comparison with other experiments

Table 4.3 lists some branching ratio measurements of charmonium production via b hadron decays. The $Br(b \rightarrow J/\psi + X)$ presented here is in good agreement with other measurements by L3 [57] and other LEP experiments [58]. This branching ratio may also be compared with $(1.12 \pm 0.20) \times 10^{-2}$ obtained by experiments at CESR and DORIS [60, 61]. Taking into account the different values for $Br(J/\psi \rightarrow \ell^+ \ell^-)$ used in the calculations, the ratio of the two branching ratios is 1.1 ± 0.3 . In addition to the B_u and B_d mesons produced at $\Upsilon(4S)$, B_s and B_c mesons and b baryons are also produced at LEP. We therefore measure the average branching ratio of $Br(b \rightarrow J/\psi + X)$ weighted by a larger variety of b-hadrons than at CESR and DORIS.

Branching ratio	Experiment	Result
$Br(b \rightarrow J/\psi + X)$	CLEO	$(1.09 \pm 0.16 \pm 0.21)\%$
	ARGUS	$(1.07 \pm 0.16 \pm 0.22)\%$
	Crystal Ball	$(1.12 \pm 0.33 \pm 0.25)\%$
	ALEPH(90-91)	$(1.21 \pm 0.13 \pm 0.08)\%$
	L3(90-91)	$(1.3 \pm 0.2 \pm 0.2)\%$
	This analysis(90-92)	$(1.25 \pm 0.16 \pm 0.14)\%$
$Br(b \rightarrow \psi' X)$	ARGUS	$(0.46 \pm 0.17 \pm 0.11)\%$
$Br(b \rightarrow \chi_{c1} X)$	ARGUS	$(1.23 \pm 0.41 \pm 0.29)\%$
	L3	$(2.4 \pm 0.9 \pm 0.2)\%$

Table 4.3: Some measurements of charmonium production via b hadron decays[57,58,60,61,62,63].

As discussed in Section 1.8.1, J/ψ mesons can be produced via the decay of higher charmonium states. The $Br(b \rightarrow J/\psi + X)$ obtained here can be combined with the ARGUS measurement of $Br(b \rightarrow \psi' + X)$ [61] to estimate the fraction of J/ψ mesons which originate from $b \rightarrow \psi' + X$ decays. Using the $Br(\psi' \rightarrow J/\psi + X) = 57 \pm 4\%$ [3], we find this fraction to be $(20 \pm 10)\%$. This result is in agreement with the theoretical prediction as discussed in Section 1.8.1.

Further, from a weighted average of the ARGUS¹[62] and L3 measurements of $Br(b \rightarrow \chi_{c1} + X)$ [63] we can estimate the fraction of J/ψ mesons which originate from $b \rightarrow \chi_{c1} + X$ decays. Using the $Br(\chi_{c1} \rightarrow J/\psi \gamma) = 27.3 \pm 1.6\%$ [3], we find this fraction is $33 \pm 14\%$. This result indicates that a larger fraction of J/ψ mesons is produced via χ_{c1} than is expected. However, more statistics is needed for any firm conclusions.

¹The branching ratio has been recalculated using the MARK III [56] value for $Br(J/\psi \rightarrow \ell^+ \ell^-)$.

By subtracting the contributions from χ_{c1} and ψ' , one can estimate that the branching ratio from direct b decay to J/ψ is about half our experimental number: $Br(b \rightarrow J/\psi(\text{direct}) + X) = (0.58 \pm 0.21)\%$. Comparison of this branching ratio to theoretical predictions (Section 1.8.2) shows that color suppression indeed plays an important role in J/ψ production via b decay.

Chapter 5

B Physics with J/ψ tagged b hadrons

5.1 Introduction

As has been shown in Chapter 4, all of the reconstructed J/ψ mesons are products of b hadron decays. Thus, they can be used to tag b hadrons. The estimation of the parent b hadron four-vector is described in the first section. This is followed by a determination of the b quark fragmentation parameter ϵ_b . Next, the reconstruction of the J/ψ decay angular distribution is described.

In all measurements presented in this thesis, an invariant mass window of $2.8 < m_{\mu^+\mu^-} < 3.4$ GeV has been used to identify the J/ψ mesons.

5.2 Estimation of the b Hadron Four-Vector

All analyses that follow, require the knowledge of the parent b hadron four vector. The decay chain considered here is $B \rightarrow J/\psi + X$. The X here is not reconstructed and hence, an indirect mechanism has to be devised to evaluate the b hadron four vector. The following subsections describe the method used to reconstruct the b momentum and direction and the resolution obtained from the parametrisations.

5.2.1 b hadron momentum estimation

Three different methods have been tried to estimate the parent b hadron momentum:

- Monte Carlo momentum. A relationship can be found between the measured J/ψ momentum and the Monte Carlo b hadron momentum.
- Reconstruct a ‘b jet’. The algorithm creates a jet with the J/ψ . Charged and neutral particles which appear to be products of the b hadron decay are added to the jet, taking first the particle which adds the least to the invariant mass according to the relation $M_i^2 = 2E_{jet}E_i(1 - \cos \theta_{jet,i})$, where E_{jet} is the energy of the existing jet, E_i is the energy of the particle i , $\theta_{jet,i}$ is the angle between the jet and the

particle. After adding a particle, the jet parameters are recalculated by adding the four momenta and the next particle searched for. The process is stopped when no particle can be added without increasing the invariant mass of the jet to a value greater than $\sim b$ quark mass. The momentum of the jet is then the parent b hadron momentum.

- Use the ASJT jet as described in Section 2.11. The b momentum can be parametrized in terms of the ASJT jet momentum containing the J/ψ .

All methods listed above gave similar results. Method 1 was chosen because it suffers least from systematic biases; methods 2 and 3 depend on the accurate modelling of fragmentation in the Monte Carlo. Figure 5.1 shows the fitted distribution of the generator b momentum versus the measured J/ψ momentum. The distribution is fitted with a third degree polynomial. The values of the parameters obtained are:

$$a1 = 2.7546 \pm 0.0156; \quad a2 = -0.0760 \pm 0.005; \quad a3 = 0.0008 \pm 0.0001. \quad (5.1)$$

The ratio of the estimated and the true b hadron momentum is shown in Figure 5.2. As can be seen from the figure, a 19% b hadron momentum resolution is obtained by the parametrisation used.

5.2.2 b hadron direction estimation

The b hadron direction is approximated by the ASJT jet axis to which the J/ψ belongs. As can be seen from Figures 5.3 and 5.4, the jet axis approximates the b flight direction very well. The resolution obtained on the azimuthal angle is 27 mrad and on θ it is 33 mrad.

5.3 Measurement of the b quark fragmentation parameter, ϵ_b

Using the b momentum parametrisation described in Section 5.2.1, the parent b hadron energy spectrum in terms of the scaled energy variable $x_E = 2E_{hadron}/\sqrt{s}$ is obtained. This variable is chosen because it is directly measurable and its definition is independent of fragmentation models. The Peterson *et al.* [14] fragmentation function gives a reasonable parametrisation of the observed scaled energy distribution on L3 [64]. The Peterson *et al.* function was originally expressed in terms of the fractional “energy” of the primordial quark, $z = \frac{(E+p_{||})_{hadron}}{(E+p_{||})_{quark}}$:

$$f(z) = \frac{N}{z} \left(1 - \frac{1}{z} - \frac{c_q^z}{1-z} \right)^{-2}, \quad (5.2)$$

where N is the normalisation and c_q^z is a free parameter. However, it is difficult to determine the primordial quark energy experimentally as the quarks can radiate gluons

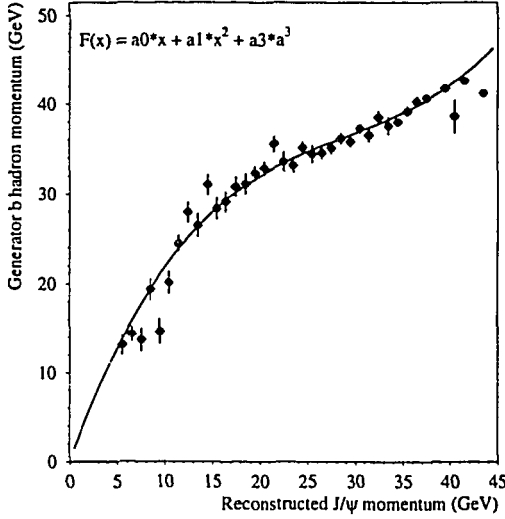


Figure 5.1: The fitted generator b hadron momentum versus the reconstructed J/ψ momentum. The distribution is fitted with a three degree polynomial giving results described in the text.

before hadronising. Therefore, the above equation is used in the same form but where z is replaced by x_E and c_q^z by ϵ_q .

Figure 5.5 shows the J/ψ acceptance in terms of the measured x_E of the b hadron. Since, the acceptance in the region $x_E < 0.4$ and $x_E > 0.9$, is small and not well defined, these regions are excluded from the fit. A binned χ^2 fit is performed on the acceptance corrected and background subtracted distribution where the fit function is given by Equation 5.2. The background estimation is obtained from Monte Carlo as shown in Table 3.1. Figure 5.6 shows the fitted distribution. From the fit, we obtain

$$\epsilon_b = 0.037 \pm 0.016, \quad (5.3)$$

which corresponds to

$$\langle x_E \rangle_b = 0.71 \pm 0.04, \quad (5.4)$$

where the errors are statistical.

5.3.1 Systematic errors

There are two sources of systematic errors in this measurement.

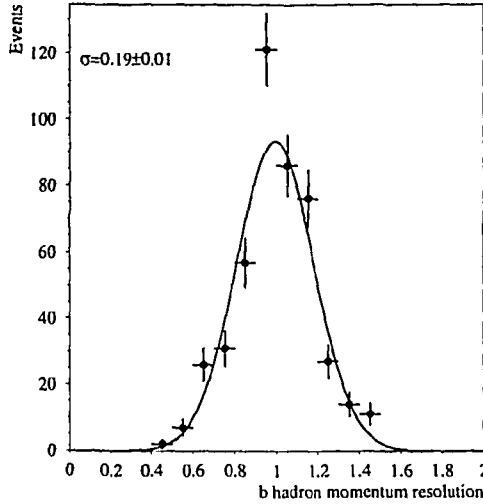


Figure 5.2: The b momentum resolution obtained by the parametrization described in the text from JETSET Monte Carlo. The plotted quantity is the ratio of the true b and the estimated b hadron momenta.

- **b momentum parametrisation** The b momentum parametrisation used was varied by $\pm\sigma$ on all the parameters changing the ϵ_b by 0.015.
- **Background fraction** The background fraction was varied by $\pm 5\%$ contributing a systematic error of 0.013 to ϵ_b .

5.3.2 Final result

Adding the systematic errors in quadrature, the final result is:

$$\epsilon_b = 0.038 \pm 0.016(\text{stat.}) \pm 0.020(\text{sys.}), \quad (5.5)$$

which corresponds to the average energy fraction of the b hadron:

$$\langle x_E \rangle_b = 0.71 \pm 0.04(\text{stat.}) \pm 0.04(\text{sys.}). \quad (5.6)$$

This measurement is in good agreement with previous measurements using the J/ψ [57] and from a study of the momentum and transverse momentum spectra of inclusive leptons from b hadron semileptonic decay [64].

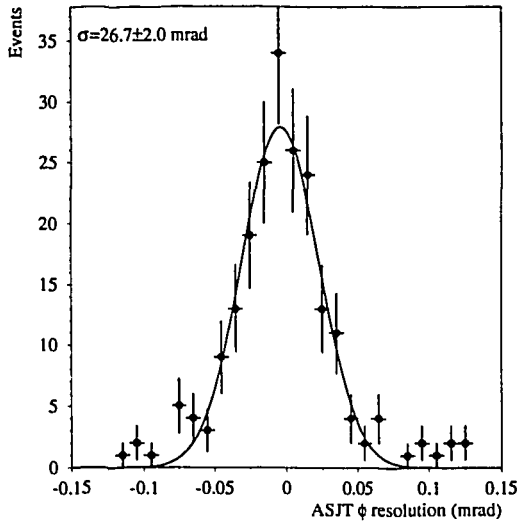


Figure 5.3: The resolution on the azimuthal angle of the b hadron flight direction from JETSET. The plotted quantity is the difference between the true and the estimated azimuthal angles.

5.4 J/ψ Decay Angular Distribution

In principle, with the momentum parametrization described in Section 5.1, one can boost back the J/ψ to the parent b hadron rest frame and obtain the decay angle, Θ^* , of the muon from the J/ψ decay in the cm-system of the J/ψ meson with respect to the direction of the J/ψ in the b hadron rest system. Since, the decay $J/\psi \rightarrow \mu^+\mu^-$ is purely electromagnetic and hence, not parity violating, any muon can be chosen. In principle, the $\cos \Theta^*$ distribution can then be fitted with the following function to determine the J/ψ alignment:

$$\frac{dn}{d\Omega} = N(1 + A \cos^2 \Theta^*), \quad (5.7)$$

where N is the normalisation and A is the alignment. However, given the resolution on the parent b hadron momentum and the statistics, this measurement is not feasible.

Figure 5.7 shows the J/ψ acceptance with respect to $\cos \Theta^*$, where Θ^* is the angle of the daughter muon in the J/ψ cm-system with respect to the J/ψ flight direction. Figure 5.8 shows the $\cos \Theta^*$ distribution from JETSET Monte Carlo. Figure 5.9 shows the same distribution after reconstruction and acceptance correction. Figure 5.10 shows the acceptance corrected and background subtracted $\cos \Theta^*$ distribution for data.

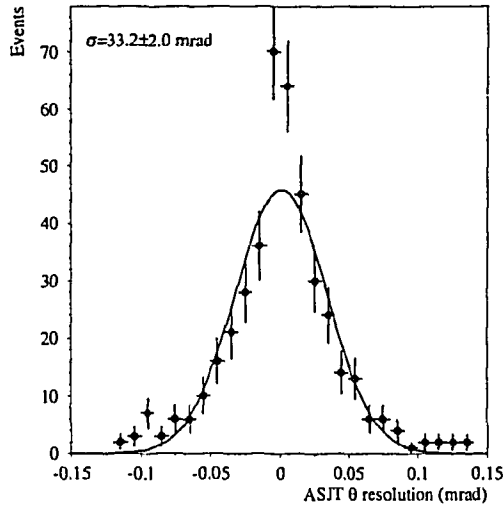


Figure 5.4: The resolution on the θ of the b hadron flight direction from JETSET. The plotted quantity is the difference between the true and the estimated b hadron θ 's.

Within the statistical error, this distribution is flat and in agreement with the Monte Carlo prediction.

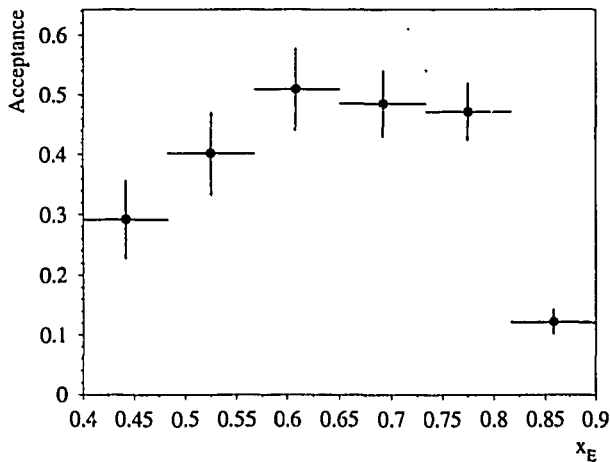


Figure 5.5: The acceptance as a function of x_{E_b} from JETSET.

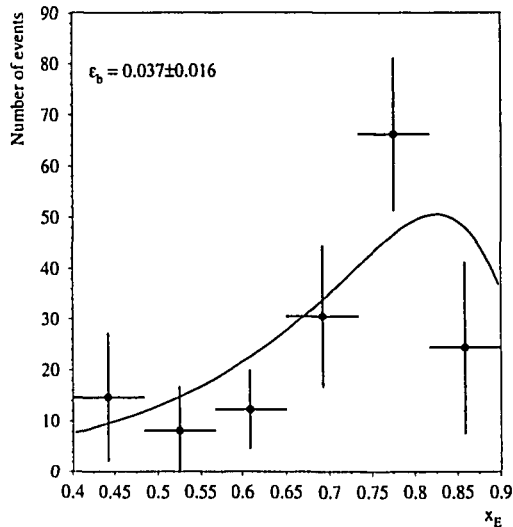


Figure 5.6: The fitted x_{E_b} distribution for data. The solid line is the result of the fit described in the text.

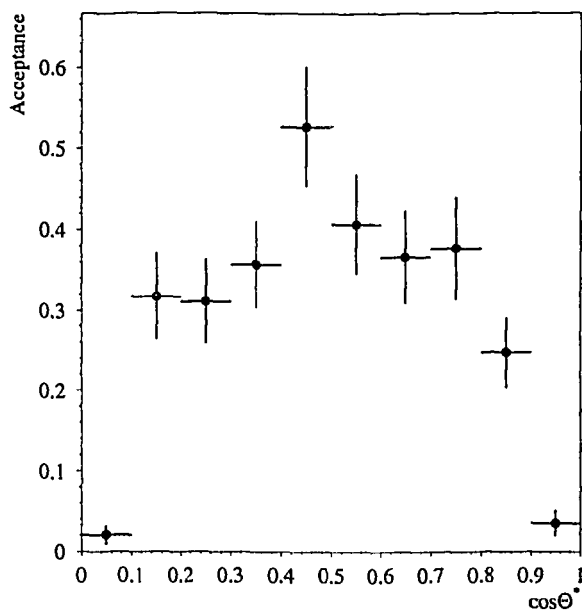


Figure 5.7: The J/ψ acceptance with respect to $\cos \Theta^*$ from JETSET Monte Carlo.

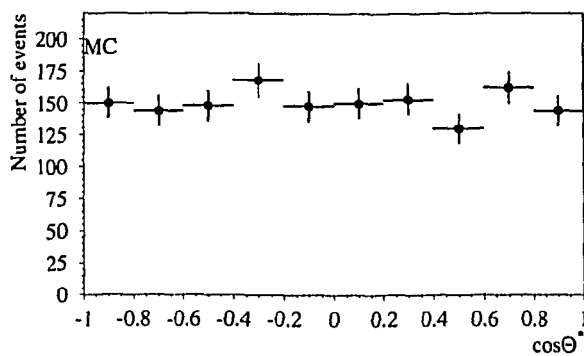


Figure 5.8: The $\cos \Theta^*$ distribution from JETSET Monte Carlo.

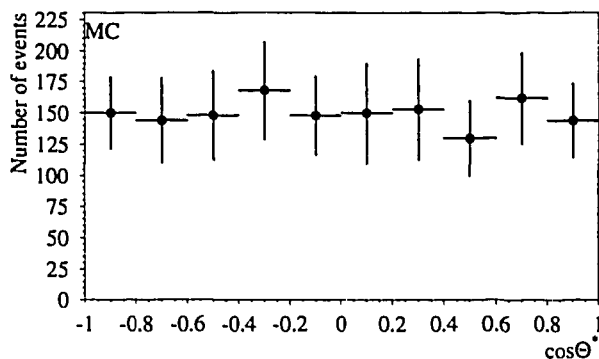


Figure 5.9: The $\cos \Theta^*$ distribution from JETSET Monte Carlo after reconstruction and acceptance correction.

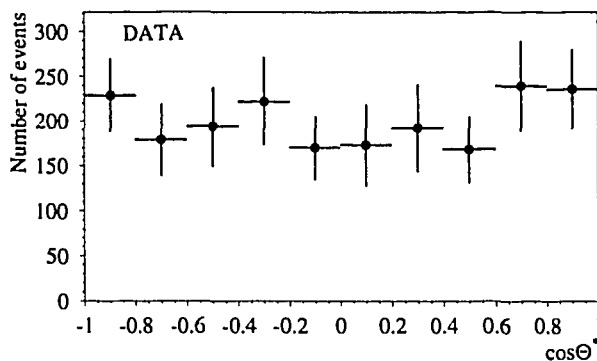


Figure 5.10: The acceptance corrected and background subtracted $\cos \Theta^*$ distribution for data.

Chapter 6

Measurement of the Average b Hadron Lifetime

6.1 Introduction

The proper decay time for a b -hadron, like that for any other unstable particle, depends on its decay length and boost; it is given by:

$$t = \frac{l}{\gamma\beta c}, \quad (6.1)$$

where l is the measured decay length. The proper decay time, t , depends on τ_b via the well known exponential probability distribution,

$$\mathcal{P}(t; \tau) dt = \frac{1}{\tau} e^{-t/\tau} dt, \quad t > 0. \quad (6.2)$$

However, what is actually measured by any detector is the proper decay time convoluted with the detector resolution. Figure 6.1 shows the generator level proper decay time from Jetset and the same plot after reconstruction. The probability distribution function then becomes:

$$\mathcal{P}_{exp}(t; \tau) dt = \frac{1}{\tau} e^{-t/\tau} dt \otimes \mathcal{R}, \quad t > 0, \quad (6.3)$$

where \mathcal{R} is the detector resolution function.

Hence, if the detector resolution is known, the proper decay time can be obtained from the measurement of the decay length and momentum; the average b hadron lifetime τ_b is then abstracted by a fit to the proper time distribution. The following sections describe the measurement of the decay length, the fitting procedure to obtain τ_b , the result and the systematic errors followed by a comparison with the τ_b obtained by other methods and experiments.

Furthermore, the τ_b obtained is used to determine the CKM matrix element $|V_{cb}|$.

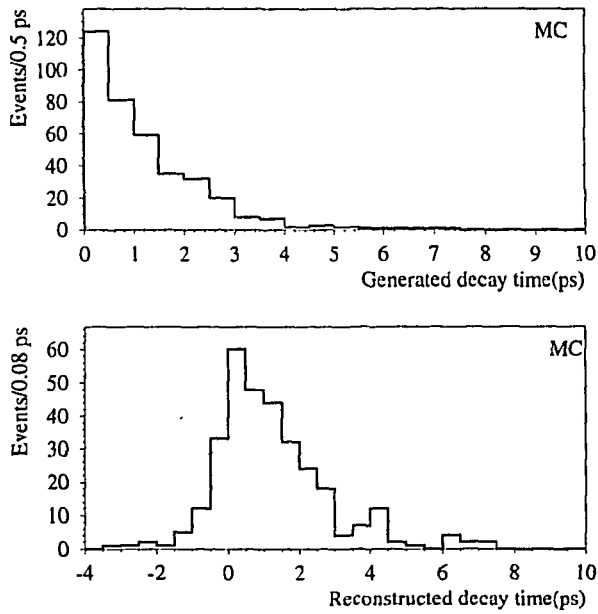


Figure 6.1: The J/ψ decay length distribution from Monte Carlo, before and after reconstruction.

6.2 Vertex Finding and Decay Distance Determination

The first step in this analysis is to find the J/ψ production and decay point which is the production point of the two daughter muons. This secondary vertex is found by minimizing the weighted sum of the distances of closest approach (DCA) of the two muon tracks where the weights are the errors on the DCA as obtained from the track fit. The systematic offsets in the DCA and the error on it due to the imperfections in the TEC calibration were corrected for as described in [65, 66]. The beamspot position in L3 is determined on a fill by fill basis by treating the entire fill (see Section 2.2) as an event. The fill vertex finding algorithm is described in detail in Appendix A. In addition, the fill vertex position for the second half of the 1992 data had to be corrected for; it is described in Appendix B. The decay point is reconstructed in the $R - \phi$ plane since the beam spot position and width are not well known in the direction parallel to the beam.

Given the vertex position, the error matrix on the vertex, and the beamspot and its error matrix, the most likely decay distance of the b-hadron in two dimensions, l_{2D} can be calculated. Figure 6.2 gives a definition of the variables used in the calculation. The point (x_1, y_1) is the most likely decay point and (x_2, y_2) is the most likely event vertex. This distance was assigned a positive sign if the decay vertex occurred after the event vertex measured along the flight direction of the b-hadron, which is approximated as the jet axis. It was signed negative if the decay vertex occurred before the event vertex. In a perfect detector, negative decay lengths would not occur. But, since what is measured is the decay length convoluted with the detector resolution, negative decay lengths are not unphysical. The values of (x_1, y_1) and (x_2, y_2) were found by minimizing the following χ^2 :

$$\chi^2 = \Delta_V^t \sigma_V^{-1} \Delta_V + \Delta_b^t \sigma_b^{-1} \Delta_b \quad (6.4)$$

where Δ_V and Δ_b are vectors in $r - \phi$ space, and

$$\begin{aligned} \Delta_V^t &= (x_V - x_1, y_V - y_1), \\ \Delta_b^t &= (x_b - x_1, y_b - y_1) \end{aligned}$$

Here, σ_V and σ_b are the error matrices for the secondary vertex and the beamspot, respectively. The determination of σ_b or the beam spot size, is described in detail in Appendix C. The b flight direction was kept fixed in the χ^2 minimization, thus putting a constraint on the allowed values of (x_1, y_1) and (x_2, y_2) . The result of the minimization was:

$$l_{2D} = \frac{x\sigma_{yy} \cos \phi_J + y\sigma_{xx} \sin \phi_J - \sigma_{xy}(x \sin \phi_J + y \cos \phi_J)}{\sigma_{yy} \cos^2 \phi_J - 2\sigma_{xy} \sin \phi_J \cos \phi_J + \sigma_{xx} \sin^2 \phi_J} \quad (6.5)$$

where

$$x = x_V - x_b$$

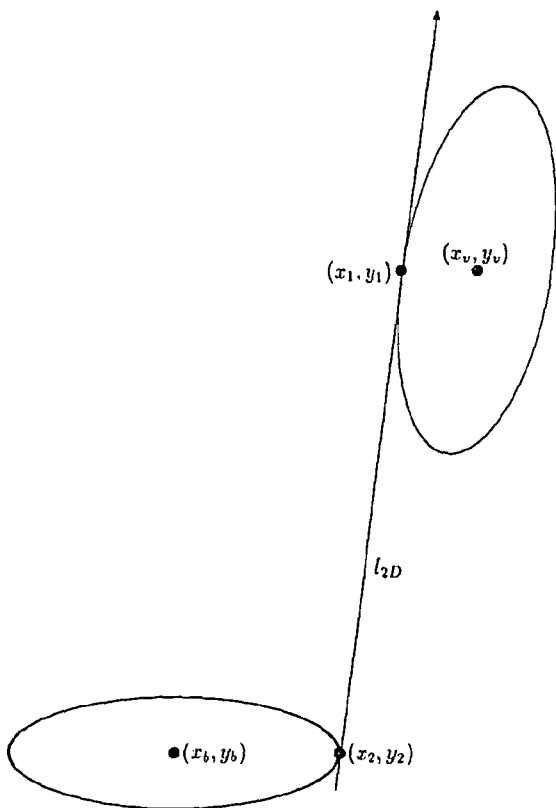


Figure 6.2: The definition of the variables used in the computation of the most likely decay distance, l_{2D} . The b hadron flight direction is approximated by the jet axis.

$$y = y_V - y_b$$

$$\sigma_{ij} = \sigma_{V,i} + \sigma_{b,j}$$

and ϕ_J is the azimuthal angle of the b hadron.

The error on the most likely distance can be computed as follows:

$$(\Delta l_{2D})^2 = \left(\frac{\partial l_{2D}}{\partial x} \right)^2 \sigma_{xx} + \left(\frac{\partial l_{2D}}{\partial y} \right)^2 \sigma_{yy} + 2 \left(\frac{\partial l_{2D}}{\partial x} \right) \left(\frac{\partial l_{2D}}{\partial y} \right) \sigma_{xy} \quad (6.6)$$

giving

$$\Delta l_{2D} = \left[\frac{\sigma_{xx}\sigma_{yy} - \sigma_{xy}^2}{\sigma_{yy} \cos^2 \phi_J - 2\sigma_{xy} \cos \phi_J \sin \phi_J + \sigma_{xx} \sin^2 \phi_J} \right]^{\frac{1}{2}} \quad (6.7)$$

The χ^2 for the most likely distance is given by:

$$\chi^2_l = \frac{(x \tan \phi_J - y)^2}{\sigma_{yy} - 2 \tan \phi_J \sigma_{xy} + \tan^2 \phi_J \sigma_{xx}} \quad (6.8)$$

The resulting decay length distribution for data is shown in Figure 6.3. An excess of events with positive decay distances, implying a non-zero lifetime of the sample, is apparent.

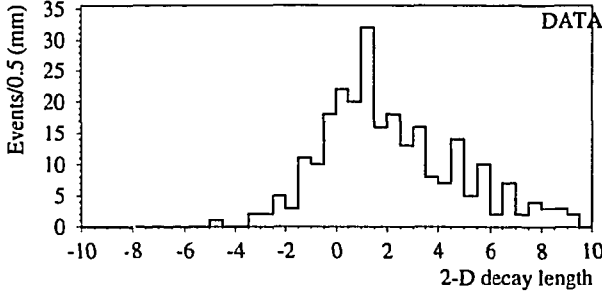


Figure 6.3: The most likely two dimensional decay length, l_{2D}

The three-dimensional decay length is given by:

$$l = \frac{l_{2D}}{\sin \theta_J}, \quad (6.9)$$

where, θ_J is the polar angle of the jet axis containing the J/ψ . The error on the decay length is then given by

$$(\Delta l)^2 = \left[\left(\frac{\Delta l_{2D}}{l_{2D}} \right)^2 + \left(\frac{\Delta \theta}{\tan \theta} \right)^2 \right] l^2 \quad (6.10)$$

$\Delta \theta$ is 0.037 rad as described in Section 5.2.2.

6.3 Event Selection

In addition to the cuts described in Sections 3.4 and 3.5 the following cuts were applied to select decays with good resolution:

- At least one inner TEC hit on each track.
- A minimum azimuthal opening angle of 50 mrad for each track pair. Figure 3.11 shows the distribution of the opening angle between the two muon tracks.
- $\chi^2_l < 10$. Figure 6.4 shows the distribution of χ^2_l for data.

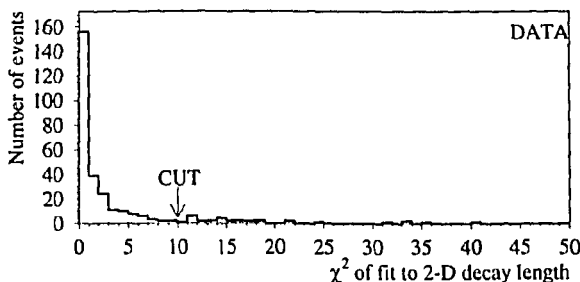


Figure 6.4: The χ^2 of the fit for the most likely decay two dimensional decay length,, l_{2D}

Since, the jet axis is used to approximate the b hadron flight direction, both muons were also required to belong to the same jet. This criterion led to the loss of 5 events.

6.4 Determination of the proper time

The measured decay length is converted to proper decay time using Equation 6.1. The b momentum is obtained via the parametrization described in Section 5.2.1. An average b hadron mass of 5279 MeV [3] is used to obtain the b boost. The error on the proper time (σ_i) for each event i , is then given by the quadratic sum of the error on the decay length, ∂l , and the 19% error on the b momentum as described in Section 5.2.1. The dominant error contribution here is from the error on the two-dimensional decay length.

6.5 The fitting procedure

An unbinned maximum likelihood fit is performed to extract τ_b from the measured proper time. As shown in Table 3.1 there is approximately 40% background in the invariant mass region of $2.8 < m_{\mu^+\mu^-} < 3.4$ GeV the majority of which comes from the cascade decays of b hadrons. The lifetime for the cascade decays will be some convolution of τ_b and the c hadron lifetimes and hence, these events also contain information of τ_b . The events are split into three categories:

- Signal: The ‘true’ J/ ψ fraction, f_s with a lifetime τ_b .
- Cascade: The cascade decay fraction, f_{bc} with a lifetime τ_{bc} where

$$\tau_{bc} = S \times \tau_b, \text{ and } S \text{ is a scale factor.}$$

- Background: The event fraction f_{bkd} with no dependence on τ_b and a pseudo lifetime, τ_{bkd} .

The probability density function is then given by

$$\mathcal{P}_i(\tau_b, \tau_{bkd}, l_i, \sigma_i) = f_s \mathcal{P}_i(\tau_b; l_i, \sigma_i) \otimes \mathcal{R} \quad (6.11)$$

$$+ f_{bc} \mathcal{P}_i(\tau_{bc}; l_i, \sigma_i) \otimes \mathcal{R} \quad (6.12)$$

$$+ f_{bkg} \mathcal{P}_i(\tau_{bkg}, l_i, \sigma_i) \otimes \mathcal{R} \quad (6.13)$$

Since, the sum of n Gaussians is also Gaussian, the error on the proper decay time can be assumed to be Gaussian. It can be shown that if \mathcal{R} is a Gaussian, the probability function in Equation 6.3 is given by:

$$P(l_i/\tau; \sigma_i) = \frac{1}{\tau} e^{(\sigma_i^2/2\tau^2)} e^{(-l_i/\tau)} \text{erfc} \left[\frac{1}{\sqrt{2}} \left(\frac{\sigma_i}{\tau} - \frac{l_i}{\sigma_i} \right) \right], \quad (6.14)$$

where σ_i is the error on l_i and

$$\text{erfc}(x) = 1 - 2\pi^{-1/2} \int_0^x e^{-t^2} dt. \quad (6.15)$$

The Likelihood function to be maximized is then given by

$$\mathcal{L}(\tau_b) = \Pi_i \mathcal{P}(\tau_b, \tau_{bkd}, l_i, \sigma_i) \quad (6.16)$$

6.5.1 Determination of the scale factor for τ_{bc}

The scale factor that relates τ_{bc} to τ_b is determined from the five flavor Monte Carlo events. In order to avoid any kinematic biases, cascade decays in the invariant mass window of $2.8 < m_{\mu^+\mu^-} < 3.4$ GeV are chosen. The proper time distribution is fitted with the function given in Equation 5.2. Figure 6.5 shows the fitted proper time distribution for these events. From the fit we find:

$$\tau_{bc} = 1.41 \pm 0.06 \text{ ps} \quad (6.17)$$

The input average b hadron lifetime in the Monte Carlo is 1.31 ps and hence,

$$\tau_{bc} = (1.08 \pm 0.08) \times \tau_b \quad (6.18)$$

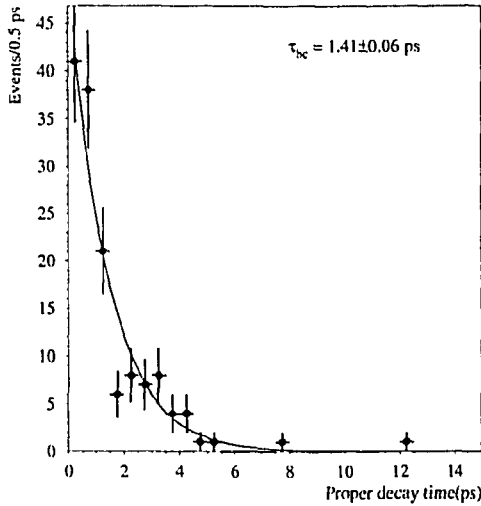


Figure 6.5: The fitted proper time distribution for cascade decays from Monte Carlo.

These cascade decays have an effective lifetime longer than the b lifetime which is as expected. The second lepton comes from the D decay after an extra flight length since the D lifetime is larger than the B lifetime.

6.5.2 Determination of τ_{bkd}

The determination of τ_{bkd} is done in a similar way as τ_{bc} , this time by fitting the rest of the background in the invariant mass window $2.8 < m_{\mu^+\mu^-} < 3.4$ GeV from Monte Carlo.

The result of the fit is

$$\tau_{bkd} = 0.57 \pm 0.43 \text{ ps}, \quad (6.19)$$

where the error is statistical. Figure 6.6 shows the distribution and the fit.

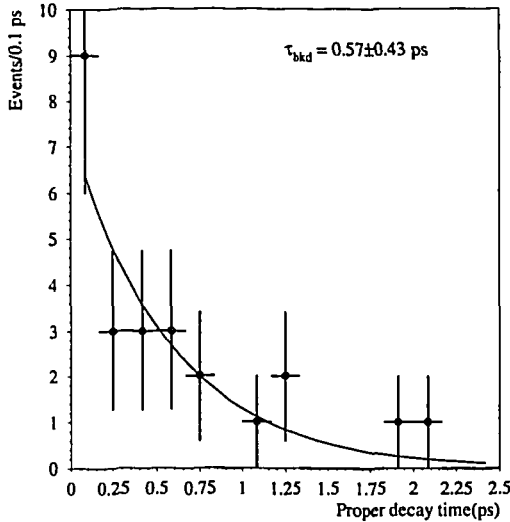


Figure 6.6: The fitted proper time distribution for background decays from Monte Carlo.

6.5.3 The Result

Figure 6.7 shows the proper time distribution for data and the result of the fit. The final result from the fit is:

$$\tau_b = 1.28 \pm 0.19 \text{ ps}, \quad (6.20)$$

where the error is statistical.

6.5.4 Systematic Errors

The systematic errors which contribute to this measurement can be grouped into two classes. The first class is associated with the physics assumptions and approximations used in the analysis; in other words, the Monte Carlo model used. The following sources are considered:

1. The b hadron momentum parametrization.

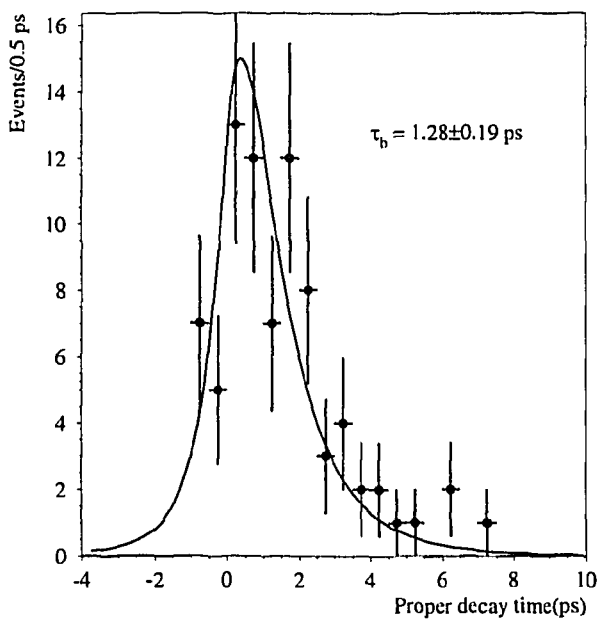


Figure 6.7: The fitted proper time distribution for data. The fit is described in the text.

2. The event fractions.
3. The prompt contribution fraction from gluon and charm fragmentation.
4. The cascade and background lifetimes.

The second class deals with the detector and reconstruction related errors inherent in the measurement; it includes:

1. The uncertainty in the jet axis modelling the b hadron flight direction in θ and ϕ .
2. The beam centroid position.
3. The TEC calibration.
4. The fitting procedure.

b hadron momentum parametrisation

To evaluate the first, the proper decay time was recalculated varying the parameters in Equation 5.1 by $\pm\sigma$. This changed the lifetime by 0.03 ps.

The event fractions

The event fractions were varied by $\pm 5\%$ in each case changing the lifetime by 0.02 ps.

The prompt contribution

Using the theoretical predictions for the gluon and charm fragmentation production of J/ψ mesons as described in Section 1.8, 5% of the J/ψ were attributed to these two processes. This changed the lifetime by 0.01 ps.

b hadron direction estimation

The θ and ϕ of the jet axis were changed by $\pm\sigma$ where the errors are described in Section 5.2.2. The change in θ changes the lifetime by 0.01 ps and the change in ϕ changes it by 0.03 ps.

The fitting procedure

The lifetime assumed in the Monte Carlo generator is reproduced by the maximum likelihood method used in the measurement; it therefore does not contribute to the systematic error.

Beam centroid position

The beam centroid position was varied by $\pm 30\mu\text{m}$ in x and y within the beam spot; this changed the lifetime by 0.04 ps.

TEC calibration

The decay length was recomputed without correcting for the ϕ dependent systematic deviations as described in Reference [65] and with the calibration constants determined by a different method. The lifetime changed by 0.05 ps by this variation.

Table 6.1 gives a summary of the various systematic errors. These are added in quadrature to yield a total systematic error of 0.08 ps.

Source	Variation	$\delta\tau_b(\text{ps})$
b momentum	$\pm 1\sigma$	± 0.03
Event fractions	$\pm 5\%$	± 0.02
Prompt contribution	5%	± 0.01
b hadron θ	$\pm 1\sigma$	± 0.01
b hadron ϕ	$\pm 1\sigma$	± 0.03
Beam centroid position	$\pm 30\mu m$	± 0.04
TEC calibration		± 0.05
Total		± 0.08

Table 6.1: Systematic Errors for the lifetime measurement.

6.5.5 Final Result

The final result of this analysis is:

$$\tau_b = 1.28 \pm 0.19(\text{stat}) \pm 0.08(\text{sys})$$

6.5.6 Comparison with other Experiments

Figure 6.8 gives a list of the τ_b measurements to date. The figure is split into three parts - measurements by non-LEP experiments, the LEP measurements using the DCA method and measurements using the J/ψ . The world average is computed by the technique described in [3] without taking any correlations into account. The result from this analysis is consistent with current world average. This measurement is statistics limited and improvements can be expected with the accumulation of more statistics.

6.6 Determination of $|V_{cb}|$

As described in Section 1.4, a measurement of τ_b can be used to determine the CKM matrix element $|V_{cb}|$ through the following relation:

$$|V_{cb}|^2 = \frac{BR(b \rightarrow \mu\nu X)}{\tau_b} \times \left[\left(\frac{G_F^2 m_b^5}{192\pi^3} \right) \left(f_c + f_u \frac{|V_{ub}|^2}{|V_{cb}|^2} \right) \right]^{-1}. \quad (6.21)$$

Here, f_q is the product of the phase space and QCD corrections:

$$f_q \equiv f_q^{\text{PS}} f_q^{\text{QCD}} \quad (6.22)$$

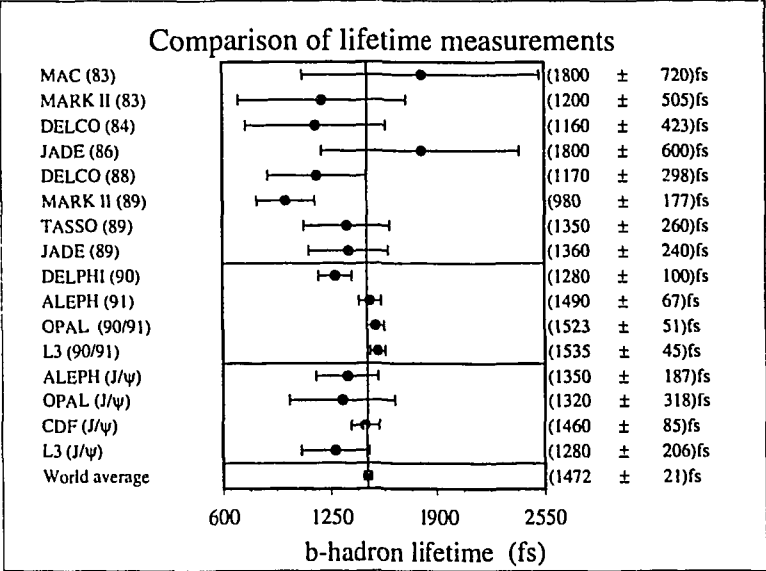


Figure 6.8: Average b hadron lifetime measurements to date.

Defining $\epsilon_q \equiv \frac{m_q}{m_b}$, the corrections can be approximated by [67]:

$$f_q^{PS}(\epsilon_q) = 1 - 8\epsilon_q^2 + 8\epsilon_q^6 - \epsilon_q^8 - 24\epsilon_q^4 \ln \epsilon_q, \quad (6.23)$$

and

$$f_q^{QCD} = 1 - \left[\frac{2\alpha_s(m_b^2)}{3\pi} \right] \left[\left(\pi^2 - \frac{31}{4} \right) (1 - \epsilon)^2 + \frac{3}{2} \right] \quad (6.24)$$

To calculate f_c and f_u , the u quark mass is chosen to be $m_u = 0.2 \pm 0.2$ GeV [3]. Effective heavy quark masses are used from measurements by the ARGUS collaboration within the framework of the ACCMM model [68] from a fit to the lepton momentum spectrum in semileptonic b meson decays [69]. The values obtained are $m_b = 4.95 \pm 0.07$ GeV and $m_b - m_c = 3.30 \pm 0.02$ GeV [70]. The value of m_b is model dependent and to take the uncertainties in the model into account, a larger error of 0.3 GeV is assigned to m_b . The value used for $m_b - m_c$ comes from the ARGUS measurement since a change in m_b will be compensated by an equivalent change in m_c . The strong coupling constant, α_s at $Q^2 = m_b^2$, is obtained by extrapolating the value measured by L3 at the Z resonance [71]. The corrections then amount to:

$$f_q^{PS} = \begin{cases} 0.447 & (c \text{ quark}) \\ 0.987 & (u \text{ quark}) \end{cases}$$

$$f_q^{QCD} = \begin{cases} 0.876 & (c \text{ quark}) \\ 0.824 & (u \text{ quark}) \end{cases}$$

The ratio $|V_{ub}|/|V_{cb}|$ is the weighted mean of the measurements by CLEO ($|V_{ub}|/|V_{cb}| = 0.076 \pm 0.008$) [72] and ARGUS ($|V_{ub}|/|V_{cb}| = 0.110 \pm 0.012$) [73], both obtained within the context of the ACCMM model. The average b hadron lifetime is taken from the present analysis and the semileptonic b branching ratio from an L3 measurement [74].

The values entering in this measurement are listed in Table 6.2. The value of V_{cb} obtained is:

$|V_{cb}| = 0.048 \pm 0.004 \pm 0.003$

The first error is due to the L3 experimental errors on the b hadron semileptonic branching ratio while the second error is due to the uncertainties on the quark masses, α_s and the ratio $|V_{ub}|/|V_{cb}|$. The dominant sources of uncertainty in this measurement are the b quark mass, the semileptonic b branching ratio and τ_b . This result is in agreement with the earlier measurement made by L3 where τ_b was obtained by the DCA method [75].

Parameter	Value	Error	Source
τ_b	1.28 ps	0.19 ps	This analysis
$\text{Br}(b \rightarrow \mu\nu X)$	11.9 %	0.67 %	L3 1990 analysis [74]
b quark mass m_b	4.95 GeV	0.3 GeV	ARGUS [70]
$m_b - m_c$	3.30 GeV	0.02 GeV	ARGUS data & ACCMM-model [70]
u quark mass m_u	0.2 GeV	0.2 GeV	PDG [3]
$\alpha_s(m_u)$	0.24	0.02	L3 extrap. from $\alpha_s(m_Z)$ [71]
V_{ub}/V_{cb}	0.086	$\pm 0.008 \pm 0.023$	CLEO/ARGUS [72, 73]

Table 6.2: Parameters used for the determination of $|V_{cb}|$

A

Fill Vertex Reconstruction in L3

A.1 Introduction

Since, the position of the luminous region in LEP has been found to be fairly stable during a fill, it is computed on a fill by fill basis in L3. The whole fill is treated as a single event and several thousand tracks enter into the computation; in most cases the fill vertex approximates the interaction point of an individual event better than the event vertex, when it can be reconstructed. In the case of Z^0 decaying into a e^+e^- or $\mu^+\mu^-$ pair, i.e. into two parallel primary tracks, it is not even possible to reconstruct an event vertex and the interaction point has to be derived from events with higher charged multiplicity recorded nearby in time. In hadronic events also, the number of primary tracks can be small and the primary vertex reconstruction is possible only for a fraction of them.

A.2 Computation of the Vertex

The fill vertex is computed through the same formalism as any other vertex, i.e., by minimizing the weighted sum of the distances of closest approach (DCA) of the tracks in the x-y plane and the intercepts of the tracks in the s-z plane, where s is the arc length of the track in the x-y plane.

From Figure A.1, we can see that the quantity to be minimized is :

$$\chi^2(\Delta\vec{r}) = \sum_i ((\omega_{dd_i} d_i'^2(\Delta\vec{r}) + (\omega_{zs_i} z_0'^2(\Delta\vec{r})) \quad (\text{A.1})$$

where ω_{dd_i} are the weights assigned to the distance of closest approach in the x, y plane and ω_{zs_i} are the weights assigned to the intercepts in the s, z plane.

It can be shown that [76]

$$d' = 1/\rho + \Delta r_z \sin\phi - \Delta r_y \cos\phi, \quad (\text{A.2})$$

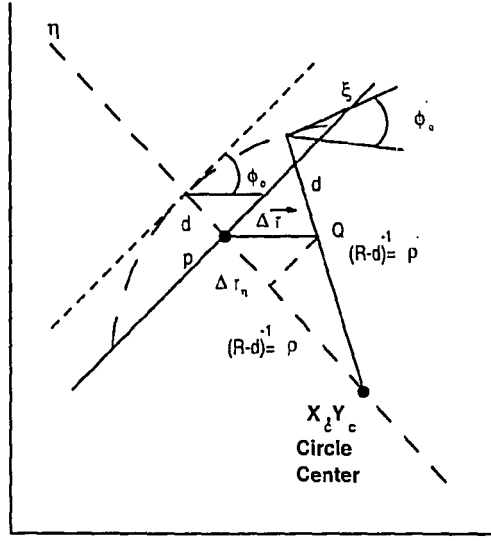


Figure A.1: The definition of the variables used in the fill vertex computation.

and

$$z'_{0i} = z_{0i} - \Delta r_z + z'_i(\Delta r_x \cos \phi + \Delta r_y \sin \phi). \quad (\text{A.3})$$

By requiring

$$\frac{\delta \chi^2}{\delta \Delta r_x} = 0 \quad \frac{\delta \chi^2}{\delta \Delta r_y} = 0 \quad \frac{\delta \chi^2}{\delta \Delta r_z} = 0 \quad (\text{A.4})$$

we obtain a system of three linear equations of the form :

$$C \Delta \vec{r} = \vec{b} \quad (\text{A.5})$$

It can be further shown that the elements of the symmetric matrix C are given as:

$$\begin{aligned} C_{11} &= \Sigma_i (\omega_{dd,i} \sin^2 \phi_i + \omega_{zz,i} z_i'^2 \cos^2 \phi_i) \\ C_{12} &= \Sigma_i \sin \phi_i \cos \phi_i (-\omega_{dd,i} + \omega_{zz,i} z_i'^2) \\ C_{22} &= \Sigma_i (\omega_{dd,i} \cos^2 \phi_i + \omega_{zz,i} z_i'^2 \sin^2 \phi_i) \\ C_{13} &= -\Sigma_i \omega_{zz,i} z_i' \cos \phi_i \\ C_{23} &= -\Sigma_i \omega_{zz,i} z_i' \sin \phi_i \\ C_{33} &= \Sigma_i \omega_{zz,i} \end{aligned} \quad (\text{A.6})$$

and, the \vec{b} is given by:

$$\begin{aligned} b_1 &= -\Sigma_i(\omega_{dd}d_i\sin\phi_i + \omega_{zz}z_{0i}z_i'^2\cos\phi_i) \\ b_2 &= \Sigma_i(\omega_{dd}d_i\cos\phi_i - \omega_{zz}z_{0i}z_i'^2\sin\phi_i) \\ b_3 &= \Sigma_i\omega_{zz}z_{0i} \end{aligned} \quad (\text{A.7})$$

Solving these equations, we obtain

$$\Delta\vec{r} = C^{-1}\vec{b} = E\vec{b} \quad (\text{A.8})$$

where E is the error matrix for the fill vertex.

The vector pointing to the fill vertex is then given by

$$\vec{r}_{fillvertex} = \vec{r}_{nom.vertex} + \Delta\vec{r} \quad (\text{A.9})$$

where $\vec{r}_{nom.vertex}$ is the “nominal vertex” which was used as the reference point for the track reconstruction.

B

Fill Vertex Correction for 1992b

Since, TEC is symmetric around the z-axis, no systematic offsets should be observed if the DCA is plotted with respect to ϕ . However, this was not true for the second half of the 1992 data. Figure B.1 shows the average DCA per outer TEC half sector for Bhabha and dimuon events. The sinusoidal structure seen in this plot is typically what happens if the fill vertex assumed for the tracks is offset. The offset in the x and y positions of the fill vertex can be obtained by fitting this plot by the following function:

$$\text{DCA} = A \times \sin(\phi - \phi'), \quad (\text{B.1})$$

where, A is the amplitude of the sine wave and ϕ' is the phase. The results from the fit are:

$$A = 0.19420; \quad \phi' = -1.1664. \quad (\text{B.2})$$

The offsets in the fill vertex position Δx and Δy in the x and y coordinates of the fill vertex can then be obtained by using the following relations:

$$\Delta x = A \cos(\phi'); \quad \Delta y = A \sin(\phi'). \quad (\text{B.3})$$

The corrections obtained were

$$\Delta x = 0.076 \text{ mm}; \quad \Delta y = -0.178 \text{ mm}. \quad (\text{B.4})$$

The corrected fill vertex was given by:

$$x_{\text{corrected}} = x + \Delta x; \quad y_{\text{corrected}} = y + \Delta y, \quad (\text{B.5})$$

where x and y were the computed fill vertex coordinates. Figure B.2 shows the average DCA per half sector plotted versus ϕ after correcting the fill vertex position. The sinusoidal structure in ϕ has been eliminated.

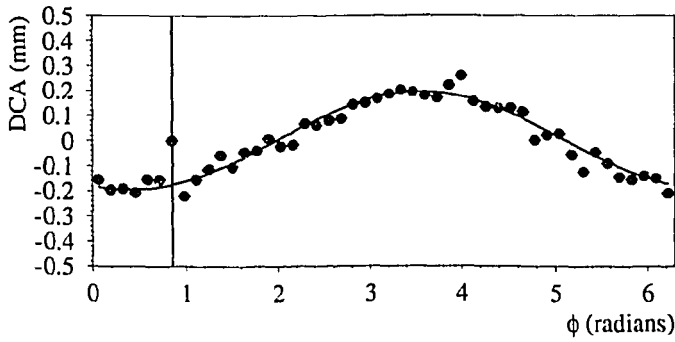


Figure B.1: The average DCA per half TEC sector versus ϕ before applying the fill vertex correction for the second half of the 1992 data for Bhabha and dimuon events. The solid line is the result of the fit described in the text.

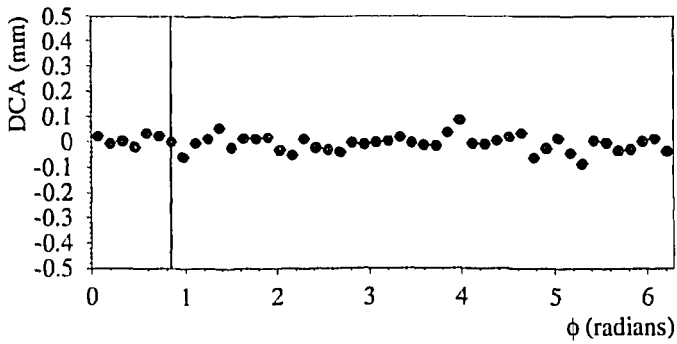


Figure B.2: The average DCA per half TEC sector versus ϕ for the second half of the 1992 data for Bhabha and dimuon events, after applying the fill vertex correction described in the text.

C

Determination of LEP Beam Spot Size

The size of the beam spot is determined from event samples with two collinear tracks, Bhabhas and dimuons [65]. The Gaussian width of the distribution of closest approach(DCA) of each of the two tracks to the fill vertex shows a variation in the azimuthal angle ϕ that allows a determination of the horizontal and vertical components of the beam spot. The TEC resolution can be taken into account by measuring the distribution of the miss distance between the two tracks. Neglecting the multiple scattering contribution and folding all tracks into the region $0 < \phi_1 < \pi$, the DCA resolution is then given by:

$$\sigma_{DCA}^2(\phi_1, \phi_2) = 0.5(\sigma_{TEC}^2(\phi_1) + \sigma_H^2 \sin^2 \phi_1 + \sigma_V^2 \cos^2 \phi_1 + \sigma_{TEC}^2(\phi_2) + \sigma_H^2 \sin^2 \phi_2 + \sigma_V^2 \cos^2 \phi_2),$$

where,

$$\begin{aligned} \sigma_{TEC}(\phi_1, \phi_2) &= \text{Intrinsic TEC DCA resolutions} \\ \sigma_H &= \text{Horizontal size of beam spot} \\ \sigma_V &= \text{Vertical size of beam spot} \end{aligned}$$

The miss distance analysis directly measures $\sigma_d^2(\phi_1) = \sigma_{TEC}^2(\phi_1) + \sigma_{TEC}^2(\phi_2)$ and the beamspot dimensions are obtained by fitting the distribution of

$$\sigma^2(\phi_1) = \sigma_{DCA}^2 - \sigma_d^2(\phi_1) = \sigma_H^2 \sin^2 \phi_1 + \sigma_V^2 \cos^2 \phi_2. \quad (C.1)$$

Figure C.1 shows the fitted distribution for the 1992a period. Table C.1 lists the values of the beam spot size for each running period.

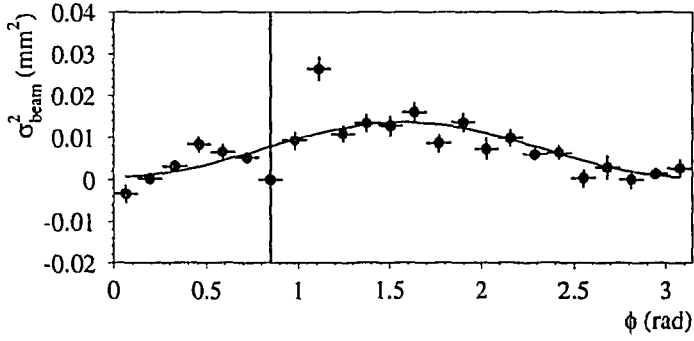


Figure C.1: Fit for the LEP beam spot size for the 1992a period.

<i>Running Period</i>	σ_H	σ_V
1990	$196 \pm 3 \mu m$	$24 \pm 11 \mu m$
1991	$157 \pm 3 \mu m$	$23 \pm 10 \mu m$
1992a	$115 \pm 3 \mu m$	$47 \pm 6 \mu m$
1992b	$116 \pm 3 \mu m$	$24 \pm 10 \mu m$

Table C.1: The LEP beam spot size for different running periods.

Bibliography

- [1] S.L.Glashow, "Partial symmetries, massless particles and gauge fields", Nucl.Phys. **22** (1961) 579;
S. Weinberg, "A model of leptons", Phys.Rev. Lett. **19** (1967) 1264;
A.Salam, "Relativistic groups and analyticity", In N.Svartholm, editor, Elementary Particle Theory, Almqvist and Wiksell, Stockholm, (1968) 369.
- [2] P.W. Higgs, Phys. Lett. **12** (1964) 132; Phys. Rev. Lett. **13** (1964) 508; Phys. Rev. **145** (1966) 1156;
F. Englert and R. Brout, Phys. Rev. Lett. **13** (1964) 321.
- [3] J.J. Hernández *et al.*, Review of Particle Properties 1992, Phys. Rev. **D 45** (1992), 2.
- [4] L3 Collab., B. Adeva *et al.*, Phys. Lett. **B 231** (1989) 509; **B 237** (1990) 136; **B 249** (1990) 341;
L3 Collab., B. Adeva *et al.*, Z. Phys. **C 51** (1991) 179;
ALEPH Collab., D. Decamp *et al.*, Phys. Lett. **B 231** (1989) 519; **B 235** (1990) 399; Z. Phys. **C 48** (1990) 365;
DELPHI Collab., P. Aarnio *et al.*, Phys. Lett. **B 231** (1989) 539;
DELPHI Collab., P. Abreu *et al.*, Phys. Lett. **B 241** (1990) 435;
OPAL Collab., M.Z. Akrawy *et al.*, Phys. Lett. **B 231** (1989) 530; **B 240** (1990) 497; Z. Phys. **50** (1991) 373;
MARK II Collab., G.S. Abrams *et al.*, Phys. Rev. Lett. **63** (1989) 2173.
- [5] R.P. Feynman, Rev. Mod. Phys. **20** (1948) 367; Phys. Rev. **74** (1948) 939, 1430; **76** (1949) 749, 769; **80** (1950) 440;
S. Tomonaga, Prog. Theor. Phys. **1** (1946) 27;
F.J. Dyson, Phys. Rev. **75** (1949) 468, 1736.
- [6] M. Kobayashi, T. Maskawa, Prog. Theor. Phys. **49** (1979) 652.
- [7] C.N. Yang and R.L. Mills, Phys. Rev. **96** (1954) 191;
M. Gell-Mann, Acta Physica Austriaca, Suppl. **IX** (1072) 733;
H. Fritzsch and M. Gell-Mann, XVI International Conference on High Energy Physics, Batavia, Vol. II p.135 (1972);
H. Fritzsch, M. Gell-Mann and H. Leutwyler, Phys. Lett. **B 47** (1973) 365.
- [8] E691 Collab. J.R. Raab, *et al.*, Phys. Rev. **D 37** (1988) 2391;
CLEO Collab. S.C. Csorna, *et al.*, Phys. Lett. **B 191** (1987) 318;

- ARGUS Collab. H. Albrecht, *et al.*, Phys. Lett. **B 210** (1988) 267;
 Mark III Collab. R.M. Baltrusaitis, *et al.*, Phys. Rev. Lett. **54** (1985) 1976.
- [9] M. Suzuki, Phys. Lett. **B 71** (1977) 139;
 J.D. Bjorken, Phys. Rev. **D 17** (1978) 171;
 V.A. Khoze, Ya.I. Azimov and L.L. Frankfurt, Proceedings, Conference on High Energy Physics, Tbilisi 1976.
- [10] See for example, the reviews:
 S. Bethke, Z. Phys. **C 29** (1985) 175;
 J. Chrin, Z. Phys. **C 36** (1987) 163.
- [11] R.D. Field and R.P. Feynman, Nucl. Phys. **B 136** (1978) 1.
- [12] B. Andersson, *et al.*, Phys. Rep. **97** (1983) 31.
- [13] G. Marchesini and B.R. Webber, Nucl. Phys. **B 310** (1988) 461.
- [14] C. Peterson, *et al.*, Phys. Rev. **D 27** (1983) 105.
- [15] T. Sjöstrand, *et al.*, "Z Physics at LEP 1", edited by G. Altarelli *et al.*, CERN 89-08, Vol. 3, (1989) 143.
- [16] S. L. Glashow, J. Illiopoulos, L. Maiani, Phys. Rev **D 2**, 1285 (1970).
- [17] J. L. Aubert *et al.* Phys. Rev. Lett. **33**, 1404 (1974).
- [18] J. L. Augustin *et al.* Phys. Rev. Lett. **33**, 1406 (1974).
- [19] E. Fichten *et al.* Phys. Rev **D 21**, 203 (1980)
 C. Quigg *et al.* Phys. Reports **56**, No. 4 (1979) 167.
- [20] H. Fritzsch, Phys. Lett. **B 86** (1979) 164.
- [21] M.B.Wise, Phys. Lett. **B 89** (1980) 229.
- [22] G. Schuler, CERN-TH **7170** (1994).
- [23] J.H.Kühn, S.Nussinov and R.Rückl, Z. Physik **C 5** (1980) 117.
- [24] J.H.Kühn and R. Rückl, Phys. Lett. **B 135** (1984) 477.
- [25] G. C. Branco *et al.*, Phys. Lett. **B 85** (1979) 269.
- [26] K. Hagiwara *et al.*, Phys. Lett. **B 267** (1991) 527.
- [27] E. Braaten *et al.*, Phys. Rev. Lett. **71** (1993) 1673.
- [28] V. Barger *et al.*, Phys. Rev. **D 41** (1990) 1541.
- [29] E. Braaten *et al.*, Phys. Rev **D 48** (1993) 4230.
- [30] H. Fritzsch and J. H. Kühn, Phys. Lett. **B 90** (1980) 164.
- [31] J. H. Kühn and H. Schneider, Z. Phys. **C 11** (1981) 263;
 W. Keung, Phys. Rev. **D 23** (1981) 2072.
- [32] B. Guberina *et al.*, Nucl. Phys. **B 174** (1980) 317.

- [33] ALEPH Collab., D. Decamp et al., "ALEPH : a detector for electron-positron annihilations at LEP", Nucl. Inst. Meth. A **294** (1990) 121.
- [34] DELPHI Collab., P. Aarnio et al., "The Delphi detector at LEP", Nucl. Inst. Meth. A **303** (1991) 233.
- [35] L3 Collab., B. Adeva et al., "The construction of the L3 detector at LEP", Nucl. Inst. Meth. A **289** (1990) 35.
- [36] OPAL Collab., K. Ahmet et. al., "The OPAL detector at LEP", Nucl. Inst. Meth. A **305** (1991) 275.
- [37] LEP design report, "The LEP injector chain", CERN-LEP/TH/83-29 vol. I (1983)
LEP design report, "The LEP main ring", CERN-LEP/TII/84-01 vol. II (1984).
- [38] A. H. Walenta, IEEE Nucl. Sci. NS-26, Nr. 1(1979) 73.
- [39] H. Akbari et al., "The L3 vertex detector: design and performance", Nucl. Inst. Meth. A **315** (1992) 161
F. Beissel et al., "Construction and performance of the L3 central tracking detector", Nucl. Inst. Meth. A **332** (1993) 33.
- [40] O. Adriani et al., "Hadron calorimetry in the L3 detector", Nucl. Inst. Meth. A **302** (1991) 53.
- [41] B. Adeva et al., "Muon detection at the L3 experiment at LEP", Nucl. Inst. Meth. A **277** (1989) 187.
- [42] X. Leijtens, "Production of tau pairs at the Z resonance", Ph.D. thesis, University of Amsterdam, unpublished.
- [43] T. Foreman, "Bottom Quark Production at the Z Resonance", PhD Thesis Univ. of Amsterdam (1993), unpublished.
- [44] T. Sjöstrand and M. Bengtsson, Comput. Phys. Commun. **43** (1987) 367;
T. Sjöstrand in "Z Physics at LEP", CERN Report CERN-89-08, Vol. III, p. 143.
For the 1990 data we used JETSET 7.2 and for the 1991 and 1992 data we used JETSET 7.3.
- [45] The L3 detector simulation is based on GEANT Version 3.14.
See R. Brun *et al.*, "GEANT 3", CERN DD/EE/84-1 (Revised), September 1987. Hadronic interactions are simulated using the GHEISIA program; see H. Fesefeldt, RWTH Aachen Report PYTHIA 85/02 (1985).
- [46] L3 Collaboration, B. Adeva *et al.*, Z. Phys. C **51** (1991) 179.
F. Filthaut, "Hadronic Cross Section Measurements on the Z Resonance with the L3 Detector", PhD Thesis Univ. of Nijmegen(1993), unpublished.
- [47] H. Kuyten, private communication.

- [48] O. Adriani *et al.*, "Hadron calorimetry in the L3 detector", Nucl. Inst. Meth. A **302** (1991) 53.
- [49] G. Marchesini and B. Webber, Nucl. Phys. B **310** (1988) 461.
- [50] W. J. Stirling, CORFUJ Monte Carlo program, private communication.
- [51] T. Sjöstrand, private communication.
- [52] M. Hebert and G. Wang, "Efficiencies Affecting the Inclusive Lepton Analysis", L3 note 1178(1992).
- [53] C. Zaccardelli, "J/ ψ Production at the Z Resonance", to be published as PhD thesis at Swiss Federal Institute of Technology, Zurich.
- [54] L3 Collaboration, B. Adeva *et al.*, Z. Phys. C **51** (1991) 179.
- [55] L3 Collaboration, B. Adeva *et al.*, Phys. Lett. B **261** (1991) 177.
- [56] MARK-III Collaboration, D. Coffman *et al.*, Phys. Rev. Lett. **68** (1992) 282.
- [57] L3 collaboration, B. Adeva *et al.*, Phys. Lett. B **259** (1991) 199.
- [58] OPAL collaboration, G. Alexander *et al.*, Phys. Lett. B **266** (1991) 485; ALEPH collaboration, D. Busculic *et al.*, Phys. Lett. B **295** (1992) 396.
- [59] L3 Collaboration, B. Adeva *et al.*, Phys. Lett. B **261** (1991) 177.
- [60] CLEO Collaboration, M.S. Alam *et al.*, Phys. Rev. D **34** (1986) 3279; CRYSTAL BALL Collaboration, W. Maschmann *et al.*, Z. Phys. C **46** (1990) 552.
- [61] ARGUS Collaboration, H. Albrecht *et al.*, Phys. Lett. B **199** (1987) 451.
- [62] ARGUS Collaboration, H. Albrecht *et al.* Phys. Lett. B **277** (1992) 209.
- [63] L3 Collaboration, O. Adriani *et al.*, Phys. Lett. B **317** (1993) 467; M. Wadhwa, "Etude de la production de J/ ψ et de χ_c dans les désintégrations du Z avec le détecteur L3 à LEP", PhD thesis, LAP-T-93/04.
- [64] L3 Collaboration, O. Adriani *et al.*, Phys. Rep. **236** (1993) 1.
- [65] L. Taylor, "Measurements of the statistical and systematic errors of the TEC impact parameter and the size and position of the LEP beam spot", L3 note 1480(1992).
- [66] D. McNally, "Measurement of the average b hadron lifetime with the L3 detector at LEP", PhD. thesis submitted to Swiss Federal Institute of Technology, Zurich, Diss. ETH No. **10446** (1993).
- [67] C.S. Kim and A. D. Martin, Phys. Lett. B **225** (1989) 186.
- [68] G. Altarelli *et al.* Nucl. Phys. B **208** (1982) 365.
- [69] S. Stone, *Semileptonic B Decays - Experimental*, from *B Decays*, edited by S. Stone, World Scientific (1992).
- [70] H. Albrecht *et al.*, ARGUS Collab., Phys. Lett. B **249** (1990) 360.

- [71] O. Adriani *et al.*, L3 Collab., Phys. Rep. **B 288** (1993)
- [72] J. Bartelt *et al.*, CLEO Collab., CLNS Preprint **1240** (1993).
- [73] H. Albrecht *et al.*, ARGUS Collab., Phys. Lett. **B 255** (1991) 297.
- [74] B. Adeva *et al.*, L3 Collab., Phys. Lett. **B 261** (1991) 177.
- [75] O. Adriani *et al.*, L3 Collab., Phys. Lett. **B317** (1993) 474.
- [76] J. C. Sens and P. Vikas, "Reconstruction of the L3 Fill Vertices", L3 internal note 1027(1991).

Summary

In the Large Electron Positron collider (LEP) bunches of electrons and positrons are brought in collision. At a collision energy of 91.2 GeV the Z resonance is excited. The Z boson, the uncharged mediator of the weak force, decays into a particle and an antiparticle almost instantaneously. The probability that in this process heavy quarks charm-anticharm($c\bar{c}$) and bottom-antibottom($b\bar{b}$) are formed is $\sim 12\%$ and $\sim 15\%$ respectively. Thus, LEP provides an ideal environment to make precision measurements in the heavy quark sector.

The data for this thesis was collected with the L3 detector from 1990-1992. L3 is one of the four experiments at LEP. The integrated luminosity collected by L3 in this period is 43.5 pb^{-1} . The L3 detector was designed to measure e^+e^- collisions up to 200 GeV with special emphasis on high resolution measurements of photons, electrons and muons. The detector is installed within a magnet providing 0.5 T field. It consists of subdetectors to detect and measure the direction and momentum/energy of charged particles, electromagnetic particles, hadrons and muons.

In this thesis the production of the $1^3 S_1$ (the J/ψ meson) and the $2^3 S_1$ (the ψ' meson) of the $c\bar{c}$ bound states are investigated. The leptonic decays of the two mesons ($J/\psi, \psi' \rightarrow l^+l^-, l = e, \mu$) provide the cleanest signals of heavy quarks. In this thesis, the ψ' and J/ψ mesons have been tagged via their decay into a muon pair. From the invariant mass distribution of the $\mu^+\mu^-$ pairs the branching ratio for J/ψ production at the Z, $Br(Z^0 \rightarrow J/\psi + X)$, was determined to be $4.0 \pm 0.6(\text{stat.}) \pm 0.4(\text{sys.}) \times 10^{-3}$ while the branching ratio for ψ' production at the Z is smaller than $< 2 \times 10^{-3}$.

(*orig. text*)
The primary source for the production of J/ψ mesons at the Z is the decay of b hadrons. In addition, a small fraction of J/ψ mesons is expected to be produced via charm fragmentation and gluon bremsstrahlung. From the 2-dimensional distribution of the invariant mass of the jet containing the J/ψ meson and the decay length of the two muons, upper limits have been set on the non-b production of J/ψ mesons. The invariant mass of the jet containing the J/ψ discriminates the J/ψ produced from gluon jets from those produced from b hadron decays and charm fragmentation. The decay length separates the non-b produced J/ψ from the b hadron produced ones. The fraction of J/ψ produced from gluon jets was determined to be $-0.07 \pm 0.10 \pm 0.01$ which translates into $Br(Z \rightarrow q\bar{q}g^*; g^* \rightarrow$

$J/\psi + X) < 0.6 \times 10^{-3}$. The fraction of J/ψ produced via charm fragmentation was determined to be $-0.08 \pm 0.19 \pm 0.01$ which leads to the $Br(Z \rightarrow c\bar{c}g^*; c(\bar{c}) \rightarrow J/\psi + X) < 1.1 \times 10^{-3}$. Since, the non-b production of J/ψ mesons is consistent with zero, it can be assumed that all the J/ψ are products of b hadron decays. The branching ratio of b hadrons into J/ψ mesons can then be determined to be $Br(b \rightarrow J/\psi + X) = (1.25 \pm 0.16(stat.) \pm 0.14(sys)) \times 10^{-2}$.

The J/ψ meson provides a tag for b hadrons and the events containing J/ψ mesons can be used study the properties of b hadrons. In order to do this, one needs the knowledge of the parent b hadron four-vector. Monte Carlo methods were used to parametrize the parent b hadron momentum in terms of the measured J/ψ momentum; this leads to a resolution of 19%. The axis of the jet containing the J/ψ was used to define the direction of flight of the b hadron with an accuracy of 30 mrad on ϕ and 37 mrad on θ . Through the momentum parametrisation, the scaled energy of the parent b hadron $x_E = 2E_{hadron}/\sqrt{s}$ was obtained. From a fit to the x_E distribution with the Peterson fragmentation function the b quark fragmentation parameter, ϵ_b was determined to be $0.038 \pm 0.016(stat.) \pm 0.020(sys.)$. This corresponds to an average fractional energy of the hadron, $\langle x_E \rangle_b = 0.71 \pm 0.04(stat.) \pm 0.04(sys.)$. This confirms the hard fragmentation of b hadrons. Further, the decay angle Θ^* of the muon from J/ψ decay in the cm-system of the J/ψ meson with respect to the flight direction of the J/ψ was obtained. Within the statistical error, the distribution is flat in $\cos \Theta^*$.

Finally, the b hadron four vector parametrisation was used to determine the decay length and then the proper decay time of the b hadrons. From the proper time distribution the average b hadron lifetime, τ_b , as determined to be $\tau_b = 1.28 \pm 0.19(stat) \pm 0.08(sys)$. Further, this measurement was combined with the measurement of the b semileptonic branching ratio from L3 to derive a value of the CKM matrix element, $|V_{cb}|$: $|V_{cb}| = 0.048 \pm 0.004 \pm 0.003$.

The results in this thesis are in agreement with those from other experiments at LEP and at Υ_{4S} and no deviation is found from expectations based on the Standard Model.

Samenvatting

In de "Large Electron Positron" versneller (LEP) worden pakketjes van electronen en positronen met elkaar in botsing gebracht. Bij een botsingsenergie van 91.2 GeV wordt de Z resonantie aangeslagen. Het Z boson, de ongeladen mediator van de zwakke kracht, vervalt bijna onmiddellijk naar een deeltje en een antideeltje. De kans dat hierbij zware quarks worden gevormd, charm-anticharm($c\bar{c}$) en bottom-antibottom($b\bar{b}$) is respectievelijk $\sim 12\%$ en $\sim 15\%$. Daarmee vormt LEP een ideale omgeving om precisiemetingen te doen in de zware quark sector.

De meetgegevens voor dit proefschrift zijn in de jaren 1990-1992 verzameld met de L3 detector. L3 is één van de vier experimenten van LEP. De L3 detector is ontworpen om e^+e^- botsingen te meten tot aan 200 GeV met speciale nadruk op metingen met hoog oplossend vermogen van fotonen, electronen en muonen. De detector is geïnstalleerd in een magneetveld van 0.5 T. Hij bestaat uit subdetectoren om de richting en impuls/energie van geladen deeltjes, electromagnetische deeltjes, hadronen en muonen te meten.

In dit proefschrift wordt de productie van de $1^3 S_1$ (het J/ψ meson) en de $2^3 S_1$ (het ψ' meson) $c\bar{c}$ gebonden toestanden onderzocht. De leptonische vervalswijzen van deze twee mesonen ($J/\psi, \psi' \rightarrow l^+l^-, l = e, \mu$) leveren het zuiverste signaal op van zware quarks. In dit proefschrift worden de ψ' en J/ψ mesonen herkenbaar gemaakt via hun verval naar een muonpaar. Uit de invariante massaverdeling van het $\mu^+\mu^-$ paar is de vertakkingsverhouding voor J/ψ productie op de Z resonantie bepaald: $Br(Z^0 \rightarrow J/\psi + X) = 4.0 \pm 0.6(\text{stat.}) \pm 0.4(\text{sys.}) \times 10^{-3}$, terwijl de vertakkingsverhouding voor ψ' productie op de Z resonantie kleiner is dan 2×10^{-3} .

De voornaamste bron van de productie van J/ψ mesonen op de Z resonantie is het verval van b hadronen. Men verwacht dat een kleine fractie van J/ψ mesonen geproduceerd wordt via charmfragmentatie en gluonbremsstrahlung. Uit de 2-dimensionale verdeling van de invariante massa van de bundel hadronen die het J/ψ meson bevat en de vervalsslengte van de twee muonen zijn bovengrenzen bepaald op de productie van J/ψ mesonen die niet van b quarks afkomstig zijn. De fractie van J/ψ geproduceerd uit gluonjets is bepaald op $-0.07 \pm 0.10 \pm 0.01$ hetgeen overeenkomt met $Br(Z \rightarrow q\bar{q}g^*; g^* \rightarrow J/\psi + X) < 0.6 \times 10^{-3}$. De fractie van J/ψ geproduceerd uit charmfragmentatie is bepaald op $-0.08 \pm 0.19 \pm 0.01$ hetgeen overeenkomt met $Br(Z \rightarrow c\bar{c}g^*; c(\bar{c}) \rightarrow J/\psi + X) < 1.1 \times 10^{-3}$. Omdat de frac-

tie niet van b quarks afkomstige J/ψ mesonen consistent is met nul, kan worden verondersteld dat alle J/ψ 's producten zijn van b hadron verval. De vertakkingsverhouding voor het verval van een b hadron naar een J/ψ meson is dan te bepalen: $Br(b \rightarrow J/\psi + X) = (1.25 \pm 0.16(stat.) \pm 0.14(sys)) \times 10^{-2}$.

Het J/ψ meson biedt de mogelijkheid b hadronen herkenbaar te maken en de gebeurtenissen die een J/ψ meson bevatten kunnen gebruikt worden om de eigenschappen van b hadronen te bestuderen. Hiervoor heeft men de kennis nodig van de vier-vector van het b hadron. Monte Carlo methoden zijn gebruikt om de impuls van het b hadron te parametriseren als functie van de gemeten J/ψ impuls; dit resulteert in nauwkeurigheid van 19%. De as van de hadronbundel die de J/ψ bevat is gebruikt om de richting van het b hadron te bepalen, met een nauwkeurigheid van 30 mrad in ϕ en 37 mrad in θ . Uit de impuls wordt de geschaalde energie van het b hadron, $x_E = 2E_{hadron}/\sqrt{s}$ verkregen. Uit een aanpassing aan de x_E verdeling met de Peterson fragmentatiefunctie is de b quark fragmentatieparameter c_b bepaald: $c_b = 0.038 \pm 0.016(stat.) \pm 0.020(sys.)$. Die komt overeen met een gemiddelde fractionele energie van het hadron $\langle x_E \rangle_b = 0.71 \pm 0.04(stat.) \pm 0.04(sys.)$. De relatief hoge waarde van $\langle x_E \rangle$ bevestigt de harde fragmentatie van b hadronen. De verdeling van de vervalshoek Θ^* van het muon van het J/ψ verval met betrekking tot de vluchtrichting van de J/ψ in het J/ψ rustsysteem bleek binnen de statistische fout isotroop te zijn.

Tenslotte is de parametrisatie van de b hadron vier-vector gebruikt om de vervalslengte en de vervalstijd van de b hadronen te bepalen. Uit de eigentijdverdeling is de gemiddelde levensduur van het b hadron τ_b bepaald: $\tau_b = 1.28 \pm 0.19(stat) \pm 0.08(sys)$. Deze meting is gecombineerd met de meting van de semileptonische vertakkingsverhouding van het b hadron om het CKM matrixelement $|V_{cb}|$ vast te stellen: $|V_{cb}| = 0.048 \pm 0.004 \pm 0.003$.

De resultaten in dit proefschrift zijn in overeenstemming met die van de andere LEP experimenten en de Υ_{4S} experimenten en er is geen afwijking geconstateerd van de verwachtingen gebaseerd op het Standaard Model.

Acknowledgments

Given that every L3 paper is authored by ~ 450 people, it is almost audacious to present a thesis with a sole author. The least one can do is acknowledge the people without whose efforts this booklet would not have existed. But then again, mentioning all the names is no mean task - the danger of forgetting someone is immense. I would like to start by collectively thanking all the members of the L3 collaboration who have wittingly or unwittingly contributed to this thesis.

I would like to thank my advisor Frits Ern  for accepting me as his student, for his guidance and all his helpful suggestions. I am myself quite surprised by the difference in quality between the first and final versions which would not have been possible without his efforts. My co-advisor Bob Clare I would like to thank for his invaluable help with the analysis presented herein and for making sure that I finished when I did.

I would like to express my deepest gratitude to Prof. A. Zichichi for his encouragement and for ensuring that my material needs were met during all the years that I spent as a graduate student. I would like to thank Prof. S. C. C. Ting for his constant encouragement.

I would like to thank Carla Zaccardelli with whom I first started looking for that peak around 3.1 GeV. Working with her was always a pleasure and a lot of fun. I would like to thank Prof. H. Schopper for leading the L3 J/ψ analysis effort. His gentleness and enthusiasm have been the source of a lot of inspiration for me.

I would like to express my gratitude to Lucas Taylor for sharing his expertise with all that goes into lifetime measurements and various tools which were required to make this thesis more aesthetically appealing. I would like to thank John Swain for all the useful discussions I had with him and for ensuring that the Apollos and the network behaved themselves. Many thanks to Drs. D. McNally, M. Merk, A. A. Syed and M. Wadhwa who got there before me and hence, I could gain from their experiences of thesis writing.

I would like to thank Richard Mount for all his sound advice and his confidence in my abilities. Many thanks to Sunanda Banerjee and Francis Bruyant who taught me the rudiments of various bits of L3 software. I benefitted greatly from discussions with Ian Brock, Tiesheng Dai, Martin Pohl, Alex Nippe and S. Sridhar for which I thank them. Thanks to Prof. H. Newman for getting me started with 'real physics'. Thanks to "Dir drs." P. A. Marchesini and E. Thomas for teaching me all I needed to know about the VM and for helping me settle down at CERN.

I would like to thank my NIKHEF colleagues B. Bouwens, A. Buytenhuijs, F. Filthaut, D. Hauschildt, E. Koffeman, H. Kuijten, Z. Dehong, G. Raven, R. Rosmalen, W. van

Rossum and B. van der Zwaan for providing a congenial environment in the office and for putting up with the cloud of smoke that invariably gathers around me. Thanks to the NIKHEF seniors Dr. G. J. Bobbink, Prof. P. Duinker, Prof. F. Linde and Prof. R. T. van de Walle for their support. Many thanks to Prof. J. C. Sens for his interest in the early stages of this thesis.

A big thank you to my friends S. Christen, J. Gerald, M. McDermott, T. Paul, C. Schcel and H. Stone for all the pleasant times I shared with them.

Special thanks to Rizwan for being with me through it all, for his love, support and patience.

Lastly, I would like to thank my parents, Ujjwal and Jyoti for their love, support, encouragement, and understanding without which I wouldn't be where I am. I would especially like to thank my parents for giving me roots and wings.

Curriculum Vitae

The author of this thesis was born on 30th April 1965 in Allahabad, India. She received the Indian Certificate for Secondary Education in 1980 as a student of Notre Dame Academy, Patna, India. She was selected for the National Talent scholarship the same year by the National Council for Educational Research and Training on the basis of a nationwide examination. She attended the Girls' High School, Allahabad, India for the Indian School Certificate examination which she passed in 1982. She then moved to Miranda House, Delhi to pursue her B.Sc.(Honors) in Physics. After completing the bachelor's degree in 1985, she studied Computer Science at the University of Delhi. She received the Master of Computer Applications degree in 1988. Since, then she has been working at CERN, Geneva. She came to CERN on a World Laboratory fellowship to work on the L3 experiment. She started her Ph.D. work with the University of Utrecht in May 1990. Currently, she is employed by the University of Montreal to work on the OPAL experiment at CERN.